Aus dem Institut für Diagnostische und Interventionelle Radiologie
der Heinrich-Heine-Universität Düsseldorf
Direktor: Univ.-Prof. Dr. med. Gerald Antoch

Contrast-Free Functional MRI for Classifying Renal Involvement in Rheumatologic Diseases: Implementation and Evaluation

Dissertation

zur Erlangung des Grades eines Doktors der Medizin der Medizinischen Fakultät der Heinrich-Heine-Universität Düsseldorf

vorgelegt von
Sara Bokonjic
2026

Als Inauguraldissertation gedruckt mit Genehmigung der

Medizinischen Fakultät der Heinrich-Heine-Universität Düsseldorf

gez.:

Dekan: Prof. Dr. med. Nikolaj Klöcker

Erstgutachter/in: PD Dr. Alexandra Ljimani

Zweitgutachter/in: PD Dr. rer. nat. Doreen M. Floß

For Prof. Dr. med. Dr. hc Hans Günther Sonntag—thank you for everything you have done for me. Forever in peace.

For Dad, Mom and Andrej

"All we have to decide is what to do with the time that is given us." – J.R.R. Tolkien

Abstract

Renal involvement in rheumatic diseases, particularly in systemic lupus erythematosus (SLE) and vasculitides, is a serious and not uncommon complication that threatens organ function and therefore demands rapid diagnosis and treatment. Although biopsy remains the diagnostic gold standard, recent advances in renal functional multiparametric MRI (mpMRI) have opened non-invasive ways to quantify perfusion, diffusion, oxygenation, and tissue microstructure using contrast-free techniques such as DWI/DTI (ADC, FA), arterial spin labeling (ASL), BOLD/T_2*, and T_1/T_2 mapping.

The aim of this dissertation is to evaluate a contrast-free mpMRI protocol for classifying renal involvement in rheumatic diseases and to explore its potential as an early biomarker to possibly complement biopsy. 10 healthy volunteers and 36 patients were examined prospectively spanning SLE and vasculitis with and without renal involvement. Imaging data acquired on a clinical 3T system was quality-controlled, post-processed, correlated with routine clinical metrics and statistically analyzed.

Several mpMRI parameters demonstrated significant differences between healthy and diseased kidneys, providing convergent evidence that mpMRI can capture disease-related alterations. Effect sizes, however, varied by metric: differences were moderate for some metrics (e.g., ADC) and larger for others (e.g., T_2*). Further, ASL perfusion showed a negative correlation with age, whereas most other parameters exhibited little or inconsistent age dependence. Of particular importance, renal T_2* values were consistently reduced across all LN groups compared to healthy participants, underscoring disease-associated impairment in renal oxygenation. This supports T_2* as a potential non-invasive biomarker of renal hypoxia.

Overall, this dissertation contributes to further development of renal mpMRI by demonstrating clinically relevant and statistically significant group differences between healthy and diseased kidneys while clarifying the circumstances under which sensitivity varies across parameters. Future work should focus on standardized, stage-based protocols, blinded multi-rater and automated ROI strategies and larger, multicenter cohorts to enable weighted multiparametric indices and improve reproducibility, generalizability, and clinical impact.

Zusammenfassung

Die Nierenbeteiligung bei rheumatologischen Erkrankungen, insbesondere bei systemischem Lupus erythematodes (SLE) und Vaskulitiden, ist eine ernste Komplikation, die den Organerhalt gefährdet und eine rasche Diagnostik und Therapie erfordert. Während die Diagnose überwiegend auf der invasiven Biopsie beruht, hat die funktionelle multiparametrische Nieren-MRT (mpMRT) in den letzten Jahren deutliche Fortschritte gemacht: kontrastmittelfreie Verfahren wie DWI/DTI (ADC, FA), ASL, BOLD/T_2* sowie T_1/T_2-Mapping ermöglichen die nicht-invasive Quantifizierung von Perfusion, Diffusion, Oxygenierung und Mikrostruktur. Ziel dieser Arbeit war die Evaluation eines kontrastmittelfreien mpMRT-Protokolls zur Klassifikation der Nierenbeteiligung bei rheumatologischen Erkrankungen sowie dessen Potenzial als früher Biomarker und Ergänzung zur Biopsie. Prospektiv wurden 10 gesunde Proband*innen und 36 Patient*innen mit und ohne Nierenbeteiligung im Rahmen von SLE und Vaskulitiden untersucht. Die 3T-mpMRT (Siemens) Daten wurden standardisiert akquiriert, ausgewertet und mit Klinikdaten korreliert; die Statistik erfolgte nach etablierten Verfahren.

Mehrere mpMRT-Parameter unterschieden signifikant zwischen gesunden und erkrankten Nieren und belegen damit krankheitsbedingte Veränderungen. Die Effektstärken variierten jedoch je nach Messgröße: für einige Parameter (z. B. ADC) waren die Unterschiede moderat, für andere (z. B. T_2*) deutlich ausgeprägter. Es zeigte sich ein Alterseffekt nur für die ASL-Perfusion (Abnahme), während die übrigen Parameter überwiegend geringe bzw. inkonsistente Zusammenhänge aufwiesen. Von besonderer Bedeutung ist, dass die renalen T_2*-Werte in allen LN-Gruppen im Vergleich zu gesunden Probanden konsistent signifikant reduziert waren, was auf eine krankheitsassoziierte Beeinträchtigung der renalen Oxygenierung hinweist und T_2* als potenziellen nicht-invasiven Biomarker der renalen Hypoxie unterstützt.

Insgesamt trägt diese Dissertation zur Weiterentwicklung der renalen mpMRT bei, indem sie klinisch relevante Gruppenunterschiede belegt und Bedingungen parameterabhängiger Sensitivität aufzeigt. Zukünftig sind standardisierte, stadiumsensible Protokolle, (teil-) automatisierte und verblindete ROI-Auswertung, höhere Messpunktdichte sowie größere multizentrische Kollektive nötig, um gewichtete multiparametrische Indizes und eine bessere Reproduzierbarkeit, Generalisierbarkeit und klinische Nutzbarkeit zu erreichen.

Abbreviations

A. / Aa.	Artery / arteries
ACR	American College of Rheumatology
ADC	Apparent diffusion coefficient
ADH	Antidiuretic hormone
AKI	Acute kidney injury
ANA	Anti-nuclear antibodies
ANCA	Antineutrophil cytoplasmic antibody
ANOVA	Analysis of variance
Anti-dsDNA	Anti-double stranded DNA
anti-ENA	Anti extractable nuclear antigen antibodies
ANTs	Advanced normalization tools
ARPKD	Autosomal recessive polycystic kidney disease
ASL	Arterial spin labeling
BOLD	Blood oxygenation level dependent
CCD	Cortical collecting duct
CHCC	Chapel Hill Consensus Conference
CKD	Chronic kidney disease
CNT	Connecting tubule
CT	Computed tomography
DCE	Dynamic contrast enhanced
DCT	Distal convoluted tubule
DKD	Diabetic kidney disease
DNA	Deoxyribonucleic acid
DSI	Digital Image Solutions
DTI	Diffusion tensor imaging
DWI	Diffusion-weighed MRI
eGFR	Estimated glomerular filtration rate
EPI	Echo planar imaging
EULAR	European League Against Rheumatism
FA	Fractional anisotropy
FAIR	Flow sensitive alternating inversion recovery
FLASH-2D	Two-dimensional fast low angle shot
FOV	Field of view
FSE	Fast spin echo
GN	Glomerulonephritis
GRE	Gradient echo

HASTE	Half-Fourier acquisition single-shot turbo spin-echo	**RF**	Rheumatoid factor
HSD	Honestly significant difference	**ROI**	Region of interest
HSP	Henoch-Schönlein purpura	**SASHA**	Saturation recovery single-shot acquisition
IgA	Immunglobulin A	**SD**	Standard deviation
KS-test	Kolmogorov-Smirnov test	**shMOLLI**	Shortened modified look-locker technique
LN	Lupus nephritis	**SLE**	Systemic lupus erythematosus
MCD	Medullary collecting duct	**SOV**	Single-organ vasculitis
MOLLI	Modified look-locker pulse sequence	**SW**	Susceptibility-weighted
mpMRI	Functional multiparametric MRI	**TE**	Echo times
MRI	Magnetic resonance imaging	**TE**	Time to echo
MRR	Magnetic resonance relaxometry	**TLCO**	Twelve-layer concentric objects
NPar	Nonparametric	**TR**	Relaxation time
PACS	Picture Archiving and Communication System	**TR**	Repetition time
PCT	Proximal convoluted tubule	**True-FISP**	True fast imaging with steady precession
PST	Proximal straight tubule	**TSE**	Turbo spin echo
R. / Rr.	Ramus / rami	**US**	Ultrasound
RBC	Red blood cell	**V. / Vv.**	Vein / veins
RBF	Renal blood flow	**VIBE**	Volumetric Interpolated Breath-hold Examination
RF	Radiofrequency		

Table of Contents

1. Introduction

Renal involvement is a major driver of morbidity in rheumatic diseases, most notably in systemic lupus erythematosus (SLE) and systemic vasculitides, where lupus nephritis (LN) is a frequent and prognostically critical complication [1]. At present, renal biopsy remains the diagnostic reference standard for diagnosis, classification, activity assessment, and prognosis [2, 3]. However, biopsy carries non-trivial risks, particularly bleeding, given the prevalence of coagulation abnormalities, thrombocytopenia, hypertension, and anticoagulant use in these patients [4-7]. Therefore, it is not well suited for repeated monitoring. These considerations emphasize the importance of implementing non-invasive alternatives capable of capturing renal pathophysiology with sufficient sensitivity and reproducibility.

In this context, contrast-free functional magnetic resonance imaging (MRI) comprises a set of complementary techniques that quantify different aspects of kidney physiology and microstructure [8, 9]. Because this approach can be performed without gadolinium-based contrasting agents, it is particularly attractive in patients with reduced renal function, as is often the case in lupus nephritis, and it also avoids concerns about nephrogenic systemic fibrosis and gadolinium deposition in the brain [10, 11]. Beyond improving primary diagnosis, functional renal MRI also offers the prospect of non-invasive, repeatable assessments for disease staging and therapy monitoring [12].

Given that more than 850 million people worldwide live with kidney disease (≈10% of the population), non-invasive tools for early detection and monitoring are a public-health priority [12-15]. The kidney´s distinctive cortico-medullary architecture and fluid-regulatory role make it especially amenable to contrast-free functional MRI, which quantifies perfusion, diffusion, oxygenation and microstructure, thus underscoring the need to understand renal anatomy and physiology to interpret these biomarkers [12, 15-17].

1.1 Kidney

The kidneys are bean-shaped, reddish-brown, bilateral, parenchymal organs in the retroperitoneum, located in the upper abdomen near the adrenal glands, liver, and spleen. They

move with respiration due to their proximity to the diaphragm and are part of the urinary system, along with ureters, bladder and urethra [18].

1.1.1 Kidney Anatomy

Each kidney is about 10-12 cm long, 4-6 cm wide, 4 cm thick and ~150 g in weight. The hilum (*Hilum renale*) is located at the center of the minor concavity (*Margo medialis*) and is the point of entry of the renal artery and exit of the renal vein and ureter (Figure 1). The right kidney lies slightly lower due to the liver [18, 19].

The renal parenchyma consists of the outer *Cortex renalis* and the inner *Medulla renalis*, the latter arranged into triangular subunits—the renal pyramids (*Pyramides renales*)—separated by a section of cortex called *Columnae renales*. A pyramid plus its surrounding cortex forms a lobe. With their apex (*Papillae renales*), the renal pyramids open toward the minor and major calyx (*Calices renales minores* and *majores*), which unite to form the renal pelvis (*Pelvis renalis*). The renal sinus (*Sinus renalis*) contains pelvis, vessels and the fatty tissue [18, 19].

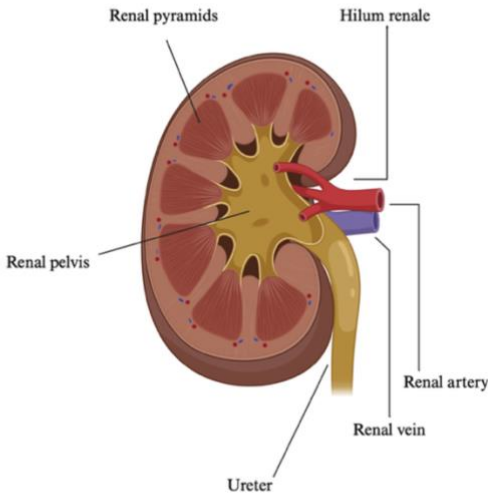

Figure 1: Kidney anatomy [20]. Cross-section of the kidney, encompassing the renal pelvis.

1.1.2 Renal Circulation

The two main renal arteries, the left *Arteria* (*A.*) *renalis sinistra* and the right *A. renalis dextra*, branch directly from the aorta, posterior to the renal veins, and divide into anterior and posterior branches, *Ramus* (*R.*) *anterior* and *R. posterior* respectively, then into interlobar (*Aa. interlobares*), arcuate (*Aa. arcuatae*), and interlobular arteries (*Aa. interlobulares* = *Aa. corticales radiatae*). They supply the cortex and then branch into more delicate arterial vessels, which are connected to the capillaries in the nephrons (described in 1.1.3). Venous drainage mirrors the arterial tree, converging into the renal veins, the left *Vena* (*V.*) *renalis sinistra* and the right *V. renalis dextra*, and inferior vena cava (*V. cava inferior*) [18, 19]. Schematic portrayal of the kidney circulation can be seen in Figure 2.

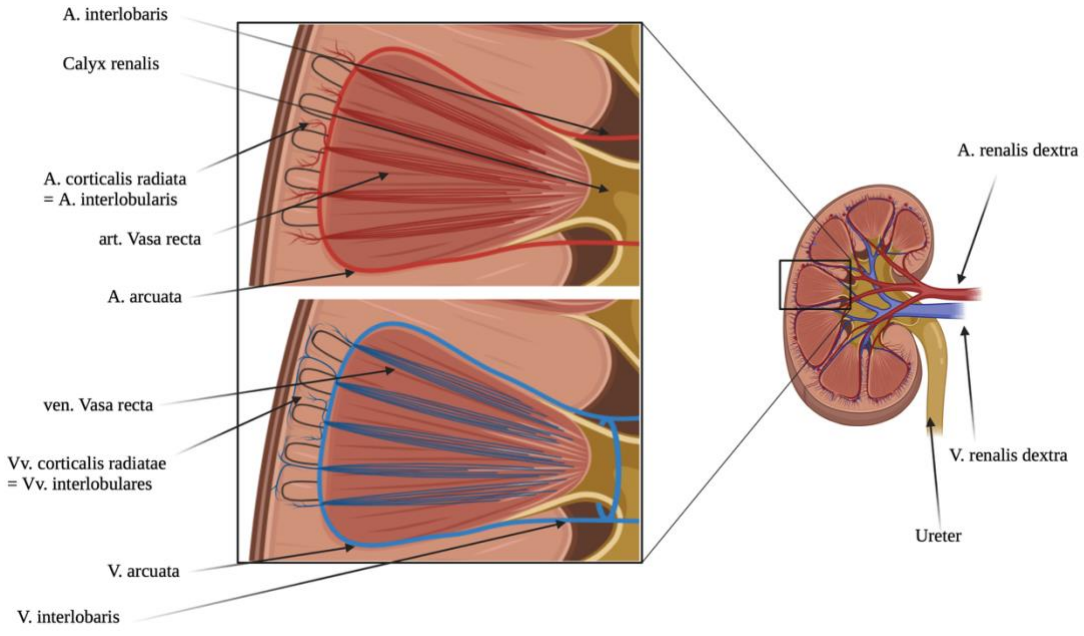

Figure 2: Renal circulation [21]. The left panel shows a magnified inset of the cortical and medullary vessels. The right panel depicts an overview of the renal cross-section.

A distinctive feature of renal circulation is the separation of cortical and medullary blood flow. Only 10% of renal blood flow (RBF) perfuses the medulla via the vasa recta, making it generally more vulnerable to hypoxia [22].

1.1.3 Kidney Histology

Microscopically, the kidney's functional units are the nephrons (~ 1 million per kidney), each consisting of a renal corpuscle (*Corpusculum renale*) or Malpighian corpuscle (*Marcello Malpighi, 1666*) and a tubular system. The corpuscle is formed by the glomerulus and its capsule, the Bowman's capsule (*William Bowman, 1842*). Tubules include proximal and distal convoluted/straight segments and the loop of Henle. Nephrons drain into collecting ducts, which pass through the pyramids of medulla and open into the renal pelvis [19]. Figures 3 and 4 show the histology of multiple regions of the kidney.

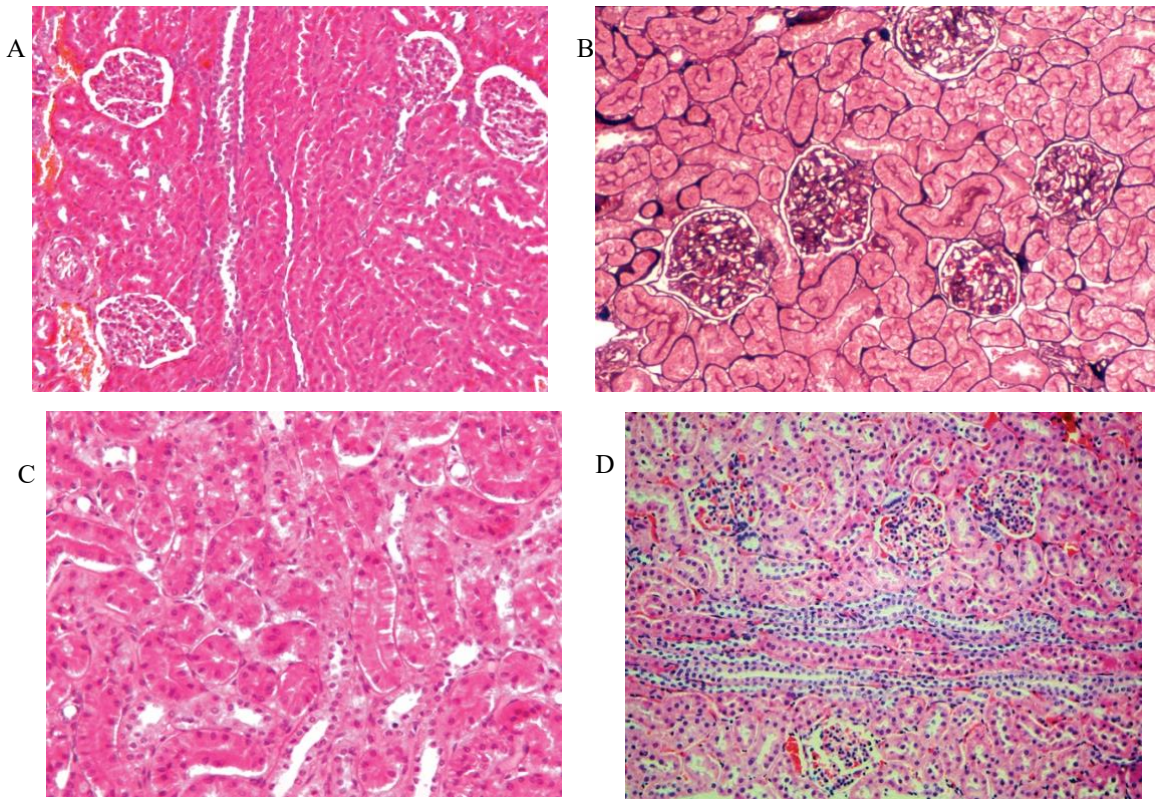

Figure 3: Histology of the kidney. Renal cortex. Corpuscles and convoluted tubules run through the cortex, while loops and collecting ducts are in the medulla. Acquired from [23]. Licensed by the publishing house Data Status from Belgrade, Serbia and by the author Prof. Dr. Ivan Nikolic.

A: Renal corpuscles and one medullary ray.

B: 5 renal corpuscles with proximal convoluted tubules.

C: Proximal and distal convoluted tubules.

D: Part of the renal cortex with medullary ray, consisting of straight sections of proximal and distal tubules and cortical part of the collecting duct.

A

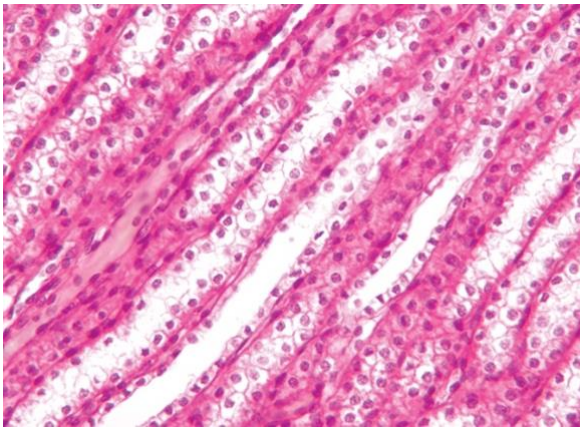

B

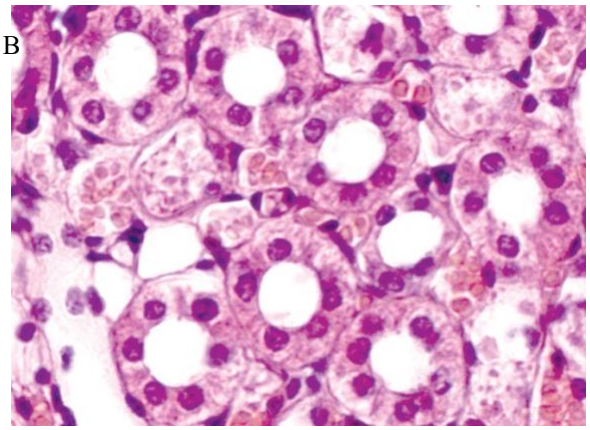

Figure 4: Histology of the kidney. Medulla renalis. Corpuscles and convoluted tubules run through the cortex, while loops and collecting ducts are in the medulla. Acquired from [23]. Licensed by the publishing house Data Status from Belgrade, Serbia and by the author Prof. Dr. Ivan Nikolic.

A: Longitudinal section of the medulla with collecting ducts.

B: Cross-section of the medulla with a few collecting ducts, one straight distal duct, few loops of Henle and a few of the capillaries (vasa recta).

1.1.4 Renal Function

The reference for this following section can be found in [24].

Kidneys filter blood, regulate fluid/electrolyte balance and produce urine. First, ultrafiltration of blood plasma occurs in the glomeruli: afferent arterioles bring blood, and the filtration barrier (consisting of the fenestrated endothelium, basal lamina, podocytes and filtration slits) allows the passage of water and small solutes (e.g., potassium [K^+] and sodium [Na^+]) but not larger proteins or cells [24]. The glomerular filtration rate (GFR) depends on the structural and functional integrity of the glomerular filtration barrier. Many pathologies of the kidney express themselves in a reduced GFR, such as chronic kidney disease (CKD), glomerulonephritis (GN), lupus nephritis and vasculitis nephritis.

The tubular system then modifies the filtrate by the process of tubular reabsorption and secretion:

- Proximal tubule (PCT, proximal convoluted tubule, and PST, proximal straight tubule): reabsorbs most solutes and water.

- Loop of Henle: generates medullary osmotic gradient and performs urine concentration. It consists of thin descending and ascending limbs, which show osmotic water-permeability, and a water-impermeable thick ascending limb for ion transport.
- Distal nephron, consisting of the distal convoluted tubule (DCT), the connecting tubule (CNT), the cortical collecting duct (CCD), and the medullary collecting duct (MCD): fine regulation of Na^+, K^+, and water under aldosterone and antidiuretic hormone (ADH) control [24].

In conclusion, the previously described tubular segments differ in their morphology and thus their function, and are responsible for homeostasis of electrolytes and water, as well as for concentrating and diluting the urine.

1.2 Systemic Lupus Erythematosus

Systemic lupus erythematosus is a rheumatic autoimmune disease with a multifactorial etiology and many different clinical and laboratory manifestations, so it shows a very complex phenotype. Autoantibodies are produced and can cause immune complex deposition, inflammation and, ultimately, permanent organ damage. The great majority of the patients produce anti-nuclear antibodies (ANA), that can be detected at some time during the course of the disease; anti-double stranded deoxyribonucleic acid (anti-dsDNA) antibodies can be found in many patients as well. Other autoantibodies, such as anti-extractable nuclear antigen (ENA) antibodies, and rheumatoid factor (RF), are less common. SLE is more frequent in women, especially women of childbearing age, with a female:male ratio of roughly 10:1. SLE can affect any organ system, but the most common manifestations include arthritis, skin lesions, renal involvement, Reynaud's phenomenon, fever, neurologic involvement etc. In Europe, roughly half a million people suffer from SLE [25-27].

As previously mentioned, renal manifestation is very common in SLE patients. Many patients eventually develop lupus nephritis. LN is an immune complex glomerulonephritis, with immune-complex-related renal inflammation and immunopathology. Eventually, the podocytes in the glomerular membrane get damaged, which causes the nephrotic syndrome. Damage to renal parenchymal cells triggers healing responses and causes the development of global glomerulosclerosis [28]. In patients with SLE, existing LN or renal disease such as

glomerulonephritis are among the most important causes of morbidity and mortality, which often determines the prognosis of SLE [27, 29, 30].

To diagnose LN, the following parameters, defined by the American College of Rheumatology (ACR) and European League Against Rheumatism (EULAR) classification criteria for SLE, need to be present: proteinuria with 0.5 g per 24 hours, renal biopsy class II or V lupus nephritis and renal biopsy class III or IV lupus nephritis (Table I). In addition, the criteria include the presence of urinary casts on a microscopic analysis, an increased serum creatinine level, decreased GFR and albumin, hematuria and pyuria in the absence of infection and menses. However, to reliably diagnose LN and to determine the degree of renal involvement, percutaneous renal biopsy is still the gold standard, despite being a very invasive procedure with many potential side effects. In particular, lupus patients with low-level proteinuria and normal renal function may require biopsy to quickly detect renal involvement and improve long-term outcomes [26, 29, 31, 32]. Furthermore, clinicians usually must perform repeated punctures in order to validate the examination results because there are many pathological pattern changes in LN. This cannot be accomplished in a short time, and it additionally increases the risk of side effects such as bleeding, which is already a great risk in SLE patients due to coagulant function abnormality. These issues underscore the fact that renal biopsy is not ideal for follow-up of treatment effects and/or regular check-ups for progression [27, 30].

Table I: World Health Organization (WHO) classification of lupus nephritis, modified after [26] and originally adapted from [33].

Class	Histology	Clinical presentation	Outcome
Normal (I)	Normal	No abnormalities	Excellent
Mesangial (II)	- Mesangial hypertrophy - Mesangial immune complex deposits	- No abnormalities in 25% - Minimal proteinuria	Good
Focal proliferative (III)	- Mesangial and endothelial proliferation - Immune deposition along capillaries - < 50% glomeruli involved	- Mild proteinuria (500-3500 mg/24h) - Nephrotic syndrome in 20% - Mild hematuria	Moderate
Diffuse proliferative (IV)	- Subendothelial immune deposits	- Moderate to heavy proteinuria - Hematuria with red blood cell	Poor

	- Cell proliferation - Crescents - Hematoxylin bodies - > 50% glomeruli involved	(RBC) casts - Mild to severe renal insufficiency - Hypertension present	
Membranous (V)	- Subepithelial granular immune deposits	- Nephrotic range proteinuria - Microscopic hematuria - Hypertension	Moderate
Sclerosing (VI)	- Focal segmental and global glomerular sclerosis - Fibrous crescents - Vascular sclerosis	- Severe renal insufficiency - End stage renal disease	Poor

1.3 Vasculitis

Vasculitis is the inflammation of blood vessel walls, with or without additional characteristic tissue injury [34]. Vasculitides comprise various complex illnesses that can affect every organ system, so it is therefore often very challenging to diagnose and manage the disease. There are many different symptoms that can occur and they can often overlap, making it even more difficult to diagnose vasculitis properly [35]. With the aim of better understanding vasculitis etiopathology, a nomenclature has been developed by the Chapel Hill Consensus Conference (CHCC) in 1994 (CHCC1994) and revised in 2012 (CHCC2012). In this nomenclature, there are three types of vessels defined that are affected by vasculitis (Figure 5). The first group consists of large vessels, such as the aorta and its major branches, as well as the analogous veins. The second group includes medium vessels, e.g. the main visceral arteries and veins and their proximal branches. The third group contains small vessels, such as intraparenchymal arteries, arterioles, capillaries, venules, and veins [34]. The intraparenchymal vessels of the kidney represent the common example of small vessels, as described in 1.1.2. Anti-neutrophil cytoplasmic antibody (ANCA)-associated vasculitides are classified as a separate group, as well as immune complex small vessel vasculitis [36].

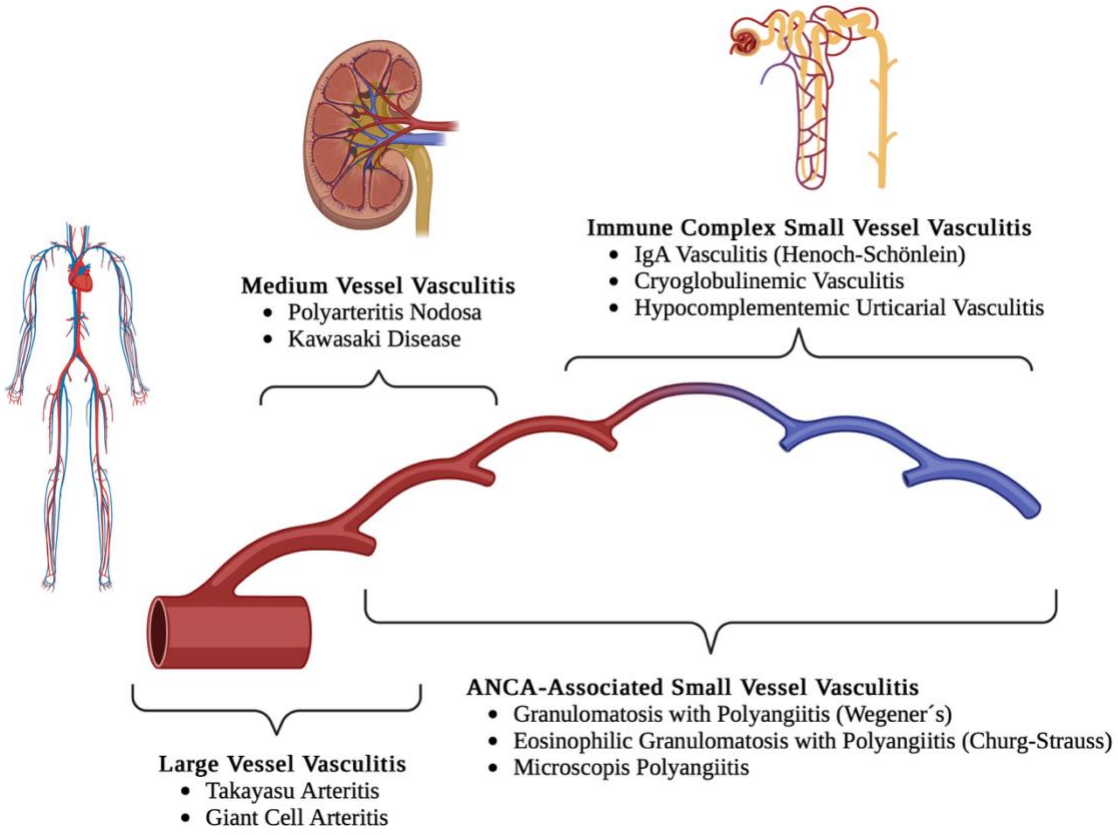

Figure 5: Classification of vasculitides by vessel size [37]. From left to right: aorta, large artery, medium artery, arteriole, capillary, venule, vein. Three main types of vessel involvement are shown, with predominantly affected vessels. There is an overlap, since all three major categories of vasculitis can affect arteries of any size. Variable vessel vasculitis can affect any type of vessel. IgA = Immunoglobulin A. Created with BioRender.com, modified after *Jennette et al.*, 2013 [34].

Vasculitis can also affect single organs such as the kidney, which is called single-organ vasculitis (SOV). SOV is characterized by inflammation of any blood vessel in one affected organ [38]. Renal manifestation is frequent in patients with systemic vasculitides due to the numerous vessels within the renal parenchyma. Small vessel vasculitides are most often in vasculitis nephritis, such as microscopic polyangiitis, granulomatosis with polyangiitis (also known as Wegener's granulomatosis), IgA vasculitis or Henoch-Schönlein purpura (HSP), and cryoglobulinemic vasculitis. They cause renal impairment through glomerular inflammation with subsequent nephritis and, potentially, renal failure. Medium- and large-sized vessels only rarely cause renal disease [39]. Renal involvement is the most serious complication and the main cause of long-term morbidity and mortality in HSP patients. Renal affection is generally accompanied with hematuria, with or without proteinuria and renal insufficiency [40]. Red

blood cell casts are strongly suggestive for vasculitis, as well as rapidly declining renal function. The gold standard to definitely confirm a diagnosis of vasculitis nephritis still remains an invasive renal biopsy [41].

1.4 The Role of Radiological Imaging In Rheumatology Patients

Among rheumatology patients, such as those with SLE and LN, the current assessment of renal lesions still predominantly relies on renal biopsy [27]. There are different conventional radiological examinations that are alternatively in use, for instance: ultrasound (US), scintigraphy, computed tomography (CT) and magnetic resonance imaging (MRI). These methods are noninvasive but still rather limited due to the complexity of the rheumatologic diseases. Ultrasonography, although simple and broadly available, is very dependent on the skill of the examinator and on the body fat percentage in patients. Scintigraphy requires special equipment and uses radioactive tracers, even though it is suitable for evaluation of GFR. The use of frequently contraindicated CT and MRI contrast agents (iodine- and gadolinium- based respectively) is also disadvantageous for this patient cohort because of the frequent renal impairment that comes with the rheumatologic diseases [27, 42]. This is why the gold standard for observing progression of e.g. renal impairment is still renal biopsy, a highly invasive procedure with many possible side effects. While biopsies provide the definitive diagnosis of a change within a certain tissue, they sample only smaller portions, which can in turn lead to false negative results and is why multiple biopsies are usually needed [42]. This is more thoroughly explained in subchapter 1.2.

Thus, it is necessary to find an alternative, noninvasive method for the effective evaluation of renal function and pathological changes within the kidney in LN patients to make a diagnosis and observe the prognosis and treatment efficacy [27, 30]. There are non-contrast, functional multiparametric MRI (mpMRI) protocols currently being developed to evaluate perfusion, interstitial diffusion, tissue oxygenation, *inter alia*, for the aim of providing alternative methods to biopsies and improving the use of radiological imaging [42]. The more detailed assessment of this topic can be found in subchapter 3.4. Since kidneys are richly supplied with blood and

have a high water percentage in tissues, they are ideal for functional MRI techniques such as diffusion tensor imaging (DTI), diffusion-weighted imaging (DWI), and blood oxygen level-dependent (BOLD) imaging [27], as well as T_1 (and T_2) mapping, which enables noninvasive characterization of the tissue. This has been tested and is regularly used for the myocardium, substituting cardiac biopsy [43].

2. Aims

The aim of this dissertation is to implement and evaluate a contrast-free functional MRI protocol to classify renal involvement in rheumatic diseases, with a primary focus on lupus nephritis. Our main goal is to explore and identify potential imaging biomarkers that capture disease-related alterations that can complement and ultimately reduce reliance on biopsy. By offering greater safety and patient comfort, this approach may advance diagnostic, prognostic, and therapeutic assessment in rheumatic diseases.

To operationalize these aims, the following questions are central:

- Can a contrast-free functional MRI protocol classify, and perhaps enable earlier detection of, renal involvement in rheumatic disease?
- Do the measured functional renal MRI parameters correlate with the clinical parameters?
- How reproducible are the measurements and is further optimization of the methods (e.g. ROI strategy, acquisition and processing choices) needed?

3. Material and Methods

3.1 Patients

The informed consent discussion was conducted with all the patients, who then signed a written agreement.

The following inclusion criteria were determined for this study:

- Male or female subjects age >18 years
- Valid informed consent, signed written agreement (appendix)
- Voluntary participation
- Patients with systemic lupus erythematosus or vasculitis

The standard MRI exclusion criteria were also defined for this study, such as:

- Subjects age <18 years, no signed consent
- Claustrophobia
- Artificial heart valve
- Artificial cardiac pacemaker
- Metal implants (Cochlear implants, hip endoprosthesis etc.)

This study included 36 patients in total. Among the 36 patients, there were 25 women and 11 men, from both outpatient and inpatient care (Table II). The MRIs were acquired during a 3-year period.

The patients included in this study were aged between 23 and 71 years. The average age of the patients was 47.3 ± 13.4 years. The median of age was 44.5 years. The more detailed portrayal of the patients can be found in the appendix.

Table II: Main characteristics of the patients.

Number	Age (in years)	Number of women	Number of men
N=36	47.3 ± 13.4	N=25	N=11

The patients were divided in three groups: patients with acute impairment of the kidney—acute kidney injury (AKI)—due to a rheumatic disease (“acute”), patients with chronic impairment of

the kidney—chronic kidney disease (CKD)—("chronic"), and SLE patients without kidney changes—without LN—("control").

Furthermore, 10 healthy age-matched test subjects were included in this study, 4 men and 6 women (building the fourth group, "healthy"). The healthy subjects were aged between 53 and 76 years. The average age amounted to 63.2 ± 6.9 years, while the median of age amounted to 64 years. Those subjects had no renal or cardiovascular diseases.

The following Table III shows the parameters describing the healthy subjects who participated in this study. The more detailed portrayal of the healthy subjects can be found in the appendix.

Table III: Main characteristics of the healthy subjects.

Number	Age (in years)	Number of women	Number of men
N=10	63.20 ± 6.9	N=6	N=4

Graphical representation of the group distribution in this study can be seen in subchapter 4.1, Figure 22.

3.2 Ethics Vote

This study was approved by the Ethics Committee at the Faculty of Medicine at Heinrich-Heine-University Düsseldorf.

Reference number: 5891R

Registration ID: 2017024144

Amendment from 06.06.2018

Date of approval: 28.08.2018

Name of applicant: PD Dr. Alexandra Ljimani, „Institut für Diagnostische und Interventionelle Radiologie Düsseldorf".

3.3 Basics of MRI

MRI is a valuable diagnostic and evaluation tool for various diseases. Due to its increased availability and reduction in cost nowadays, it is becoming more relevant and more frequently used. It is a noninvasive imaging technique used to create cross-sectional images in any

anatomical plane, with the aim of examining the morphology and function of the tissue. This subchapter is intended to provide a theoretical description of the basic MRI principles. Functional MRI will be explained in subchapter 3.4. The references used for this section can be found in [44-48].

Currently, MRI imaging is based on hydrogen atoms. Hydrogen atoms have the highest gyromagnetic ratio (γ) in the human body. Since the human body consists largely of tissues rich in hydrogen atoms, these tissues are able to produce a strong natural MR signal when placed in an external magnetic field. Because a hydrogen nucleus only consists of one proton and no neutrons, this nucleus is often referred to simply as a "proton". Atomic nuclei with spin are constantly rotating about an axis which induces a certain magnetic moment that is parallel to the rotation axis when placed in an external magnetic field [45] (Figure 7). Each spinning nucleus precesses at a specific characteristic frequency, calculated with the Larmor equation [44] (Figure 6). This rotation axis can change in the presence of powerful magnetic impulses (gradients).

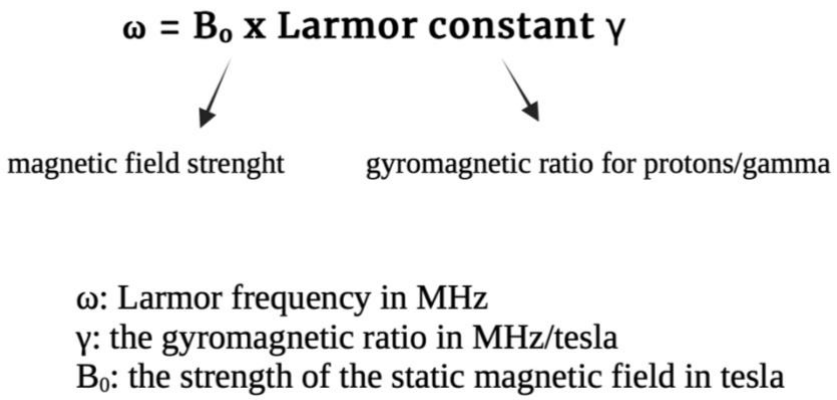

Figure 6: The Larmor equation [49].

The Larmor frequency ω is in direct proportion with the magnetic field B_0. The Larmor constant (gyromagnetic ratio [46], γ) is defined by the specific precession frequency of the spinning nucleus in relation to a determined magnetic field strength. For hydrogen protons, the Larmor constant amounts to 42.57 MHz per Tesla. The Larmor frequency of hydrogen changes in dependence of the magnetic field strength. At 3-Tesla systems, which were employed in this study, the ω of hydrogen would be 126 MHz [44].

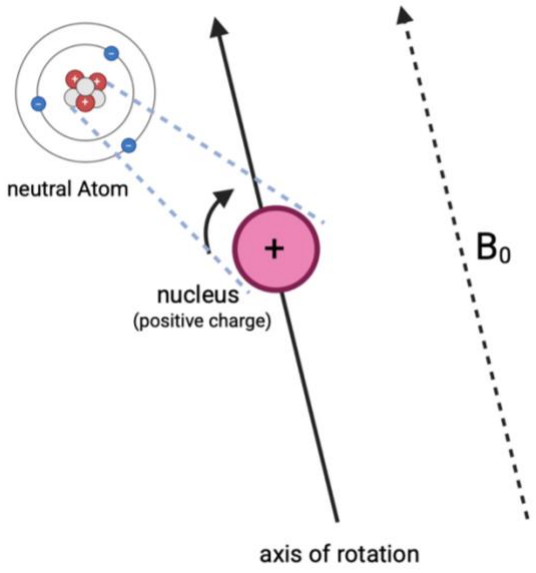

Figure 7: Nuclear spin [50]. This figure shows a rotating nucleus, with spin perpendicular to the rotating axis. B_0: external magnetic field. Created with BioRender.com, modified after *Dale et al.*, 2015 [45].

Building on the concept of Larmor precession, the spatial orientation and motion of the proton can be described using a rotating coordinate system containing three axes (*x, y, z*) (Figure 8). The stationary axis *z* is parallel to B_0 while the varying axes *x* and *y* rotate at the Larmor frequency [45]. Because of the same direction of the axis *z* and the magnetic field B_0, the magnetization that can be measured here is called the longitudinal magnetization (M_z). The state where only the M_z is present is called the stable state. Application of radiofrequency (RF) pulse at the Larmor frequency can change the proton alignment due to inducing a change in the vector direction of the M_z. Protons absorb the energy from the RF pulse and when the transmitter of RF is turned off, protons release this gained energy. The process mentioned is called relaxation [45]. The protons always begin to realign themselves immediately after transmitter is off, and they return to their stable state, an equilibrium. As previously explained, the protons release the previously added energy during this process and emit an echo signal while they relax. This is time-dependent and is characterized by the relaxation time (TR).

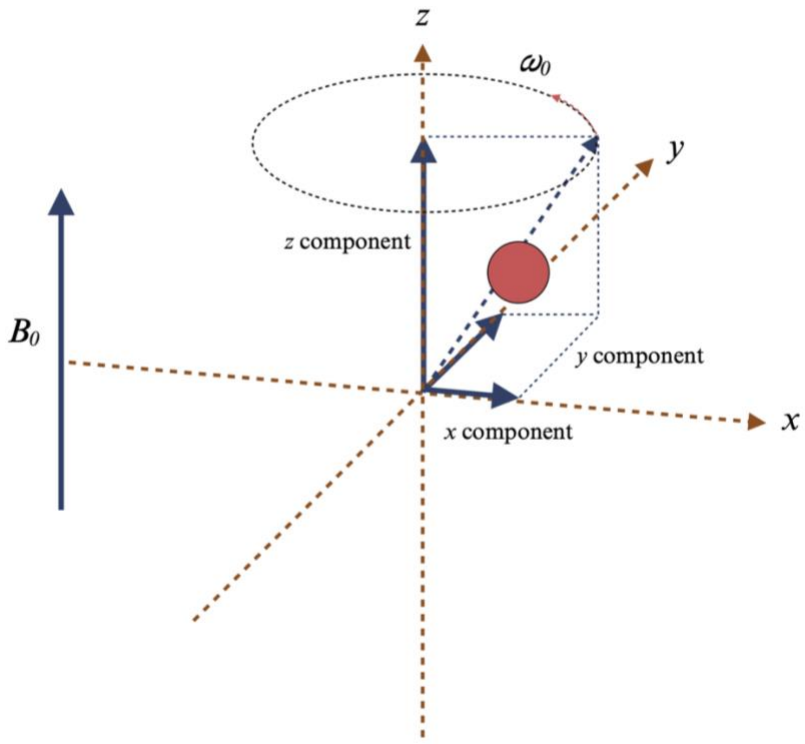

Figure 8: Coordinate system [51]. This figure shows a magnetic field with a proton which precesses about it. The precessional axis is the stationary axis *z* and it is parallel to the main magnetic field (B_0). The component *z* does not change as the proton precesses. The varying axes *x* and *y* rotate at the Larmor frequency (ω_0), which is proportional to B_0, as shown in the equation in Figure 6. Created with BioRender.com, modified after *Dale et al.*, 2015 [45].

3.3.1 Relaxation Times

There are two types of relaxation times that can be measured: longitudinal and transverse relaxation, also known as T_1 and T_2. Both relaxation types differ in separate tissues, which can be used to distinguish those tissues in MRI [44, 45].

The relaxation time T_1 is also known as longitudinal relaxation time or spin-lattice relaxation time [44, 46]. It describes the time required for the *z* to return to its original state after the RF pulse was applied. As previously explained, the M_z is parallel to B_0 while in steady state. When a RF pulse gets applied, the M_z rotates into the transverse plane. After the transmitter is turned off, the protons gradually return to the original orientation. The term T_1 relaxation explains this process of returning to longitudinal magnetization (M_z) [45].

A 90° RF pulse causes a rotation of *xy*-plane by 90°, which is called the transverse magnetization M_{xy}. After the pulse is gone and the relaxation process starts, the transverse magnetization is gradually decaying. This is explained by the T_2 relaxation, also known as transverse relaxation time or spin-spin relaxation time [44, 45]. Both relaxation times are demonstrated in Figure 9.

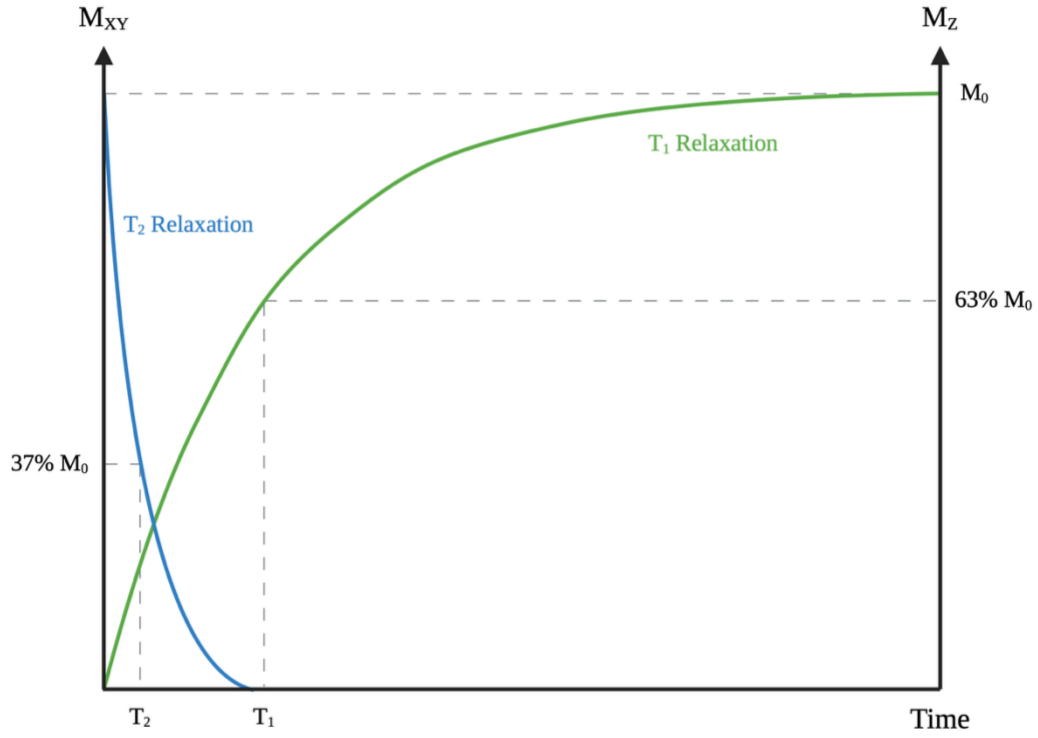

Figure 9: T_1 and T_2 relaxation [52]. Exponential T_1 recovery and T_2 decay, created with BioRender.com and modified after *McRobbie et al.*, 2017 [53].

As shown in Figure 9, T_1 relaxation time is the time required for M_z to again reach 63% of its maximum value (M_0). T_2 relaxation time is the time required for the transverse component of M_0 to decay to 37% of its initial value [45].

In summary, immediately after a 90° RF pulse was applied, there is no longitudinal magnetization, only transverse magnetization. While the protons are releasing their pulse-gained energy and returning to their original state, the longitudinal relaxation increases, until the initial state M_z is eventually restored completely. This is a slower process in relation to the transverse relaxation, as shown in Figure 9. During the relaxation of protons and the increasing of the

longitudinal relaxation, the transverse relaxation decreases until there is only longitudinal and no transverse relaxation [46].

3.3.2 Spatial Localization

In an effort to be able to use the MR signal for diagnostic purpose, the exact source of the signal must be spatially located, which requires the use of gradients, explained further below [47]. For this, the volume elements (voxels) need to be defined. Every digital image consists of a pixel matrix. Each square of the matrix represents one pixel. Every pixel gets assigned a number, which indicates an intensity of a certain signal. Since MRI creates cross-sectional images, each pixel contains information about a volume unit (voxel) [48]. Per estimation, one voxel contains 10^{18} water molecules. This once again shows the high abundance of hydrogen nuclei in organic tissue [44]. For spatial localization, different MR gradients are needed. Since the external magnetic field B_0 is static, smaller and more dynamic magnetic fields that have the means to change electrical fields need to be added. These additional magnetic fields are called gradients. The MR gradients are used to localize protons within the tissue in all three axes (*x, y, z*) [47] and they therefore enable frequency-encoding and phase-encoding. Now, different tissues can be spatially separated by frequency. This is called slice-selection. In summary, by measuring the frequency and amplitude, it is possible to differentiate MR signals and to set apart their individual positions in space, which enables image reconstruction in three dimensions [47].

3.4 Functional Multiparametric MRI (mpMRI)

Functional MRI techniques, such as diffusion-weighted (DWI) MRI, blood oxygenation level dependent (BOLD) MRI, arterial spin labeling (ASL), and magnetic resonance relaxometry (MRR), are promising, non-invasive methods for assessing renal functional aspects, which can't be assessed using other methods available at the moment [16]. In this following section, the basic principles of mpMRI and parameters used for renal function assessment of the patient cohort as well as healthy subjects participating in this study will be explained.

mpMRI consists of multiple imaging methods previously developed for assessing regional and time-varying changes in brain metabolism, but it can also be used in other organs such as the kidney. mpMRI is non-invasive and shows good spatial resolution. Therefore, it could be a potentially good biomarker for disease and therapy monitoring [54].

Diffusion and perfusion are processes that can be measured with mpMRI. Atoms and molecules continually move because of interactions with their surroundings. This continuous movement also happens on a molecular level, which is known as Brownian motion (*Robert Brown, 1827*) and represents random displacement of the molecules in space. Diffusion is based on this principle and refers to the constant random motion of particles, which results in a net movement from regions of higher to lower concentration when a concentration gradient is present (e.g., between intra- and extracellular spaces) [45].

$$\mathbf{D = A/t}$$

D: diffusion coefficient (cm^2*s^{-1})

A: Surface (cm^2)

t: time (s)

The displacement of the water molecules in tissue due to Brownian motion can be assessed by diffusion-weighted magnetic resonance imaging (DWI). DWI uses magnetic field gradients of different strengths called *b*-values that can vary during acquisition. In free molecular water motion, DWI signal exponentially decays with the strength of the magnetic gradient which was applied (*b*-value). A study by *Caroli et al.* [55] showed this method can be used to detect changes in renal interstitium due to renal fibrosis.

3.4.1 ADC

For measurements of the water molecule motion that is not free but in tissues *in vivo*, the apparent diffusion coefficient (ADC) is calculated [45]. This is one of the simplest parameters that can be used to assess tissue microstructure [16]. In renal tissue, molecular water motion is not free but rather obstructed by heterogeneity of the tissue and hindrances such as cell membranes and interstitial matrix. In the kidney, those particular hindrances are radial tubules and straight collecting ducts. This is why an adjusted diffusion coefficient is needed.

$$\mathbf{ADC = \ln (Sb_{low}/Sb_{high}) / (b_{high} - b_{low})} \text{ [56]}$$

In this formula, b_{low} and b_{high} are two *b*-values and Sb_{low} and Sb_{high} are corresponding signal intensities [56]. The DWI signal decay in the tissue is described by a monoexponential equation [55]. In this study, the ADC measurements were quantified inline (Figure 10). After regions of

interest (ROI) based analysis, a mean value was calculated, as shown in Figure 10. For detailed image analysis used for all metrics, see 3.7.

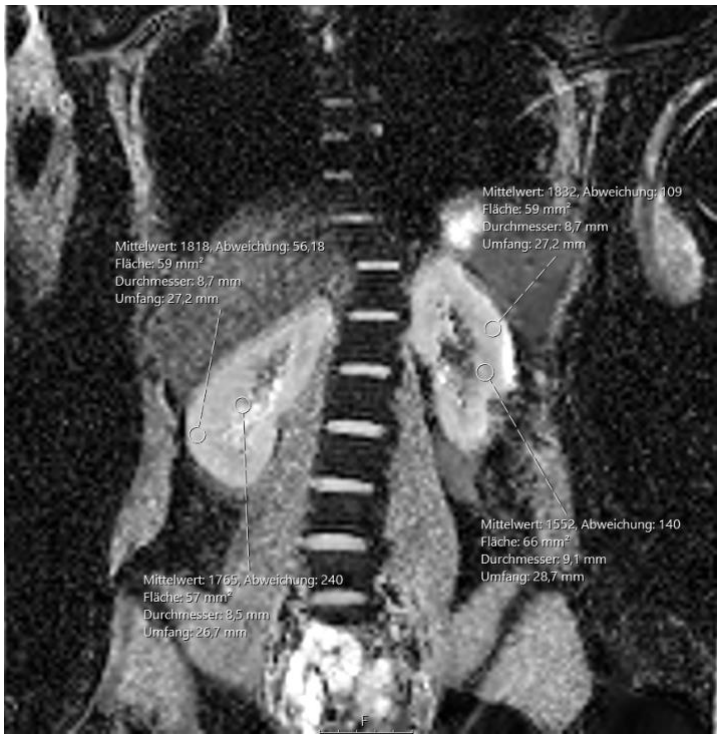

Figure 10: An example of ADC measurement, acquired in PACS. ROI drawings in cortex and medulla of both kidneys, with automated calculation of mean values.

3.4.2 FA

To characterize the tissue microarchitecture by quantifying the degree of tissue anisotropy and by exploring the spatial dependence of diffusion, the diffusion signal needs to be encoded in a bigger number of directions. The method used for this process is called diffusion tensor imaging (DTI) and requires multiple measurements of a minimum of six different directions of signal encoding. DTI allows assessment of the fractional anisotropy (FA), the vector of the diffusion, which reflects the degree of tissue anisotropy.

$$\mathbf{FA} = \sqrt{\frac{(\lambda_1-\lambda_2)^2 + (\lambda_2-\lambda_3)^2 + (\lambda_1-\lambda_3)^2}{2(\lambda_1^2 + \lambda_2^2 + \lambda_3^2)}} \quad [57]$$

λ_x are eigenvalues of diffusion coefficients.

FA, which is, together with ADC, also one of the diffusion-based biomarkers, shows the diffusion asymmetry within a voxel. The value of FA varies between 0 and 1. For example, 0% FA would mean complete (absolute) isotropy ($\lambda_1 = \lambda_2 = \lambda_3$), 100% FA complete (maximal) anisotropy [55]. The values of the FA parameter were produced similarly to ADC directly inline and analyzed with ROIs (Figure 11).

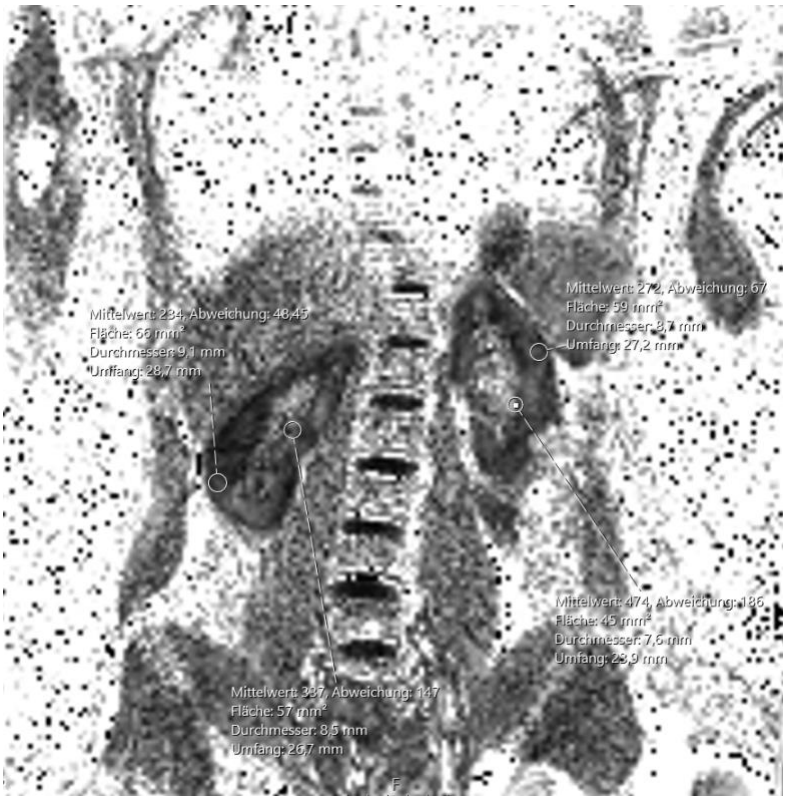

Figure 11: An example of FA measurement, acquired in PACS. ROI drawings in cortex and medulla of both kidneys, with automated calculation of mean values.

3.4.3 ASL

Approximately 25% of the cardiac output circulates through the kidneys. Renal perfusion is essential for delivering oxygen and nutrients and provides the driving pressure for glomerular filtration. Renal ischemia is an important characteristic of AKI and can hasten the progression of CKD. It is therefore of great importance to assess renal perfusion and detect and quantify changes early on to predict, slow down, or prevent further deterioration. Arterial spin labeling is a non-invasive MRI technique which uses magnetically labeled protons of water in arterial blood as an endogenous tracer to examine perfusion of a tissue without the need for exogenous

contrasting agents. ASL quantifies renal perfusion in a following unit: mL/100g/min. It has short acquisition time of 5-10 min., which makes combination with other mpMRI techniques possible, but it is still restricted to research settings [22]. ASL was originally developed for perfusion assessment in cerebral tissue [58, 59], but it has also been validated for renal use by several studies [60-64]. Most often, the FAIR (flow sensitive alternating inversion recovery) sequence is used for perfusion preparation and the True-FISP (true fast imaging with steady precession) sequence for data acquisition [16, 65, 66]. ASL reduces with subject's age and renal excretory function [22]. Many studies report reproducibility of renal perfusion by ASL and lower ASL values in chronic kidney disease patients compared with healthy subjects, which correlates with eGFR (estimated glomerular filtration rate). This reproducibility seems to be lower in the medulla than the cortex [22]. The systematic review by *Odudu et al.* [22] evaluated ASL data in 53 studies and established a following ASL range: from 139 to 427 mL/100g/min in renal cortex of healthy subjects and from 83 to 412 mL/100g/min in various patient groups. ASL values over 600 mL/100g/min are a probable indicator for unintentional positioning of the labeling ROI inside a vessel.

For the ASL calculation, two image types are needed: the label (tag) image and the control image. For the label, a RF pulse is applied. This alters the longitudinal magnetization of protons in arteries before they enter the imaging plane. An image of the label is therefore created after a latency time. The control image is taken at the same latency time, with the absence of labelling the protons in arterial blood. It is assumed that the inverted magnetization of the blood is the only difference between the two image types. Therefore, to calculate perfusion, a subtraction of the label from the control image is needed [22]. Multiple mpMRI sequences are required after which an average is calculated. This has been done by in-house developed STROKETOOL (Version 2.0, H.-J. Wittsack, DSI, Frechen, Germany) (Figure 12). Since acquisitions require labeled and unlabeled measurements and their subtraction, motion correction was performed by advanced normalization tools (ANTs) prior to ASL calculation [16].

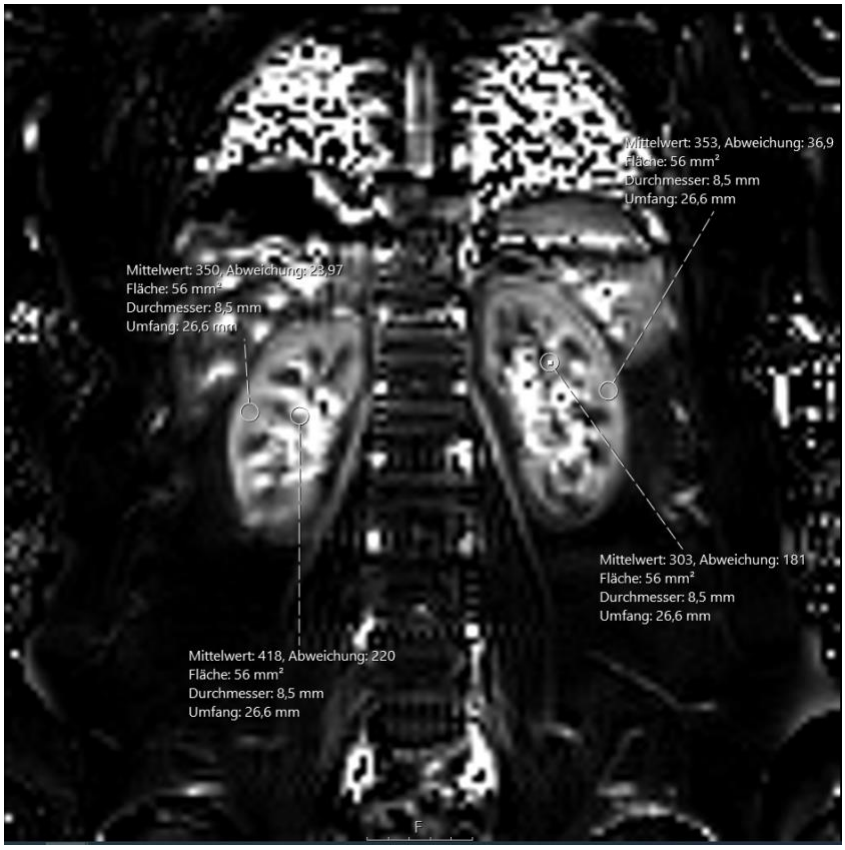

Figure 12: An example of ASL measurement, acquired in PACS after processing in STROKETOOL. ROI drawings in cortex and medulla of both kidneys, with automated calculation of mean values.

3.4.4 T_2-Star (T_2*/BOLD)

BOLD-MRI assesses renal tissue oxygenation by registering tissue deoxyhemoglobin levels voxel-wise. It is expressed as the apparent relaxation rate R_2*, which is the same as decay rate $1/T_2$* (R_2* = $1/T_2$*). R_2* increases in tissues with low oxygenation due to increased levels of deoxyhemoglobin. Thus, decreases in R_2* indicate lower deoxyhemoglobin and therefore higher oxygenation [67].

T_2* relaxation is the decay of transverse magnetization, as a result of a combination of spin-spin relaxation (T_2) and magnetic field inhomogeneity (T_2') [68]. T_2* relaxation is one of the main factors that determine image contrast with gradient-echo (GRE) sequences. It is fundamental for many MR applications, e.g. susceptibility-weighed (SW) imaging, perfusion MRI and mpMRI [69]. As already explained in 3.3.1, transverse magnetization is formed by a RF pulse, and it has a maximum magnitude instantly after its formation. Immediately after the RF pulse

is gone, it starts rapidly decreasing in magnitude while the protons return to their steady state. This process of reduction of transverse magnetization is called transverse relaxation. T_2 relaxation time is hence the time representing the reduction of the signal to 37% of its maximum value. Irreversible dephasing of the transverse magnetization is caused by transverse relaxation. As previously mentioned, there is also a local field inhomogeneity which causes a reversible dephasing effect and its time is called T_2* relaxation [69]. With T_2 relaxation, after the RF is turned off, there is a 180° refocusing pulse used for elimination of the magnetic field inhomogeneity. That is why the T_2 relaxation only shows the decay of transverse magnetization of the certain tissue. On the other hand, the T_2* relaxation does not include the 180° pulse to correct dephasing, and it therefore also takes the inhomogeneity of the main magnetic field into account. Different than T_2 relaxation, which obtains a spin echo signal, T_2* relaxation acquires a GRE signal, which is one of the most common techniques used for BOLD-MRI, along with single shot echo planar imaging (EPI). GRE T_2* sequence can detect even the smallest changes in the magnetic field and thus detect small tissue lesions early on, which makes an early diagnosis possible [67, 68, 70]. T_2* is shorter than T_2, as shown in Figure 13, and their relation can be portrayed by the following equation [69]:

$$\frac{\mathbf{1}}{\boldsymbol{T2^*}} = \frac{\mathbf{1}}{\boldsymbol{T2}} + \boldsymbol{\gamma} \times \Delta \boldsymbol{B_{inhom.}}$$

γ: gyromagnetic ratio

$\Delta B_{inhom.}$: magnetic field inhomogeneity

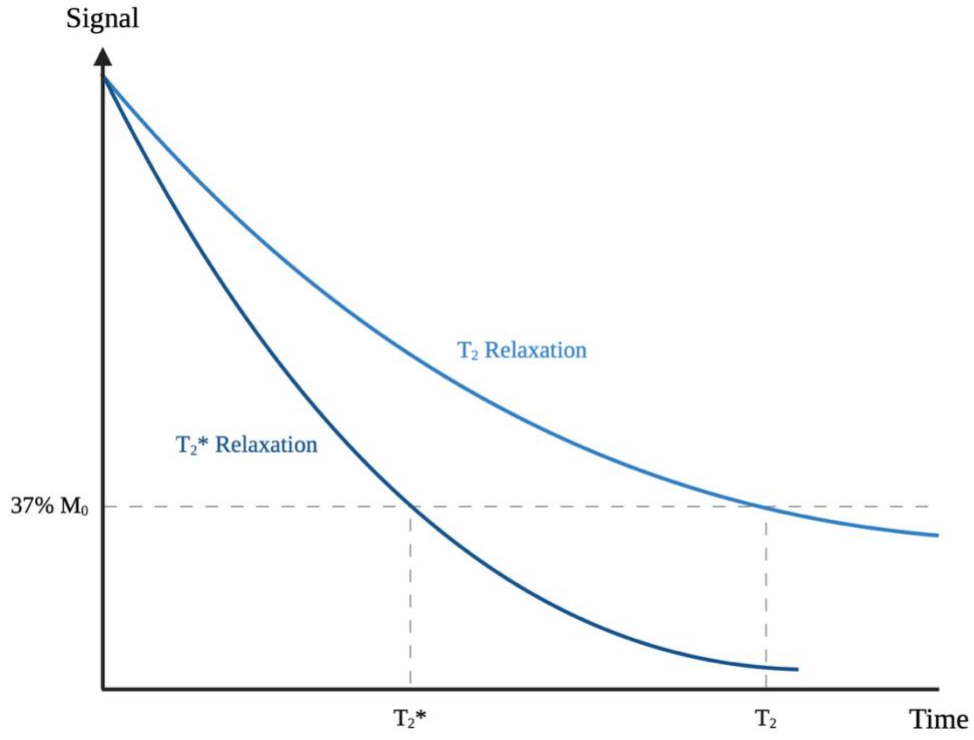

Figure 13: T_2 and T_2* relaxation [71]. The relaxation curves for T_2 and T_2* are shown, with T_2* being shorter than T_2. Created with BioRender.com and modified after *Chavhan et al.*, 2009 [69].

Figure 20 shows T_2* values of each pixel calculated with the help of ROIs.

3.4.5 T_1- and T_2-Map

Another functional MR method is magnetic resonance relaxometry (MRR), which is the measurement of independent quantitative MR relaxation times T_1 and T_2. MRR has been frequently used in other organs, such as cardiac MRI, for detecting changes like oedema, fibrosis, and amyloid deposition. Even so, the use of renal MRR is still low. Renal MRR nevertheless has potential for non-invasive quantification of renal function, tissue inflammation, and changes such as oedema and fibrosis of the kidney [72].

As explained in 3.3.1, after a RF pulse is applied, the protons return to the steady-state equilibrium parallel to B_0, which means that the longitudinal magnetization increases while the transverse magnetization decreases. Those are two independent processes that can be measured,

first by the spin-lattice (T_1) and second by the spin-spin (T_2) relaxation time. They vary in different tissues and are the reason for tissue contrast in morphological MRI [72]. The longitudinal (T_1) and transverse (T_2) relaxation can be mapped voxel-wise by using the non-invasive mpMRI tissue characterization method, called native T_1 and T_2 mapping, since no contrasting media is being used [73]. T_1 and T_2 mapping is defined as a quantification of T_1 and T_2 relaxation times.

T_1 mapping can be carried out with several different techniques: look-locker technique, modified look-locker pulse sequence (MOLLI), shortened modified look-locker technique (shMOLLI), saturation recovery single-shot acquisition (SASHA) [43], etc. After T_1 time of a tissue has been calculated, it can be depicted voxel-wise on a parametric T_1 map. T_1 map can be calculated from spoiled gradient echo images at several varying flip angles in separate acquisitions [73]. The flip angles used for the calculation of T_1 map for the patient cohort in this study are as follows:

#1 flip angle: 4°

#2 flip angle: 20° and

repetition time (TR) (ms): 5

This has been accomplished using in-house developed STROKETOOL (Version 2.0, H.-J. Wittsack, Digital Image Solutions [DSI], Frechen, Germany) (Figure 14).

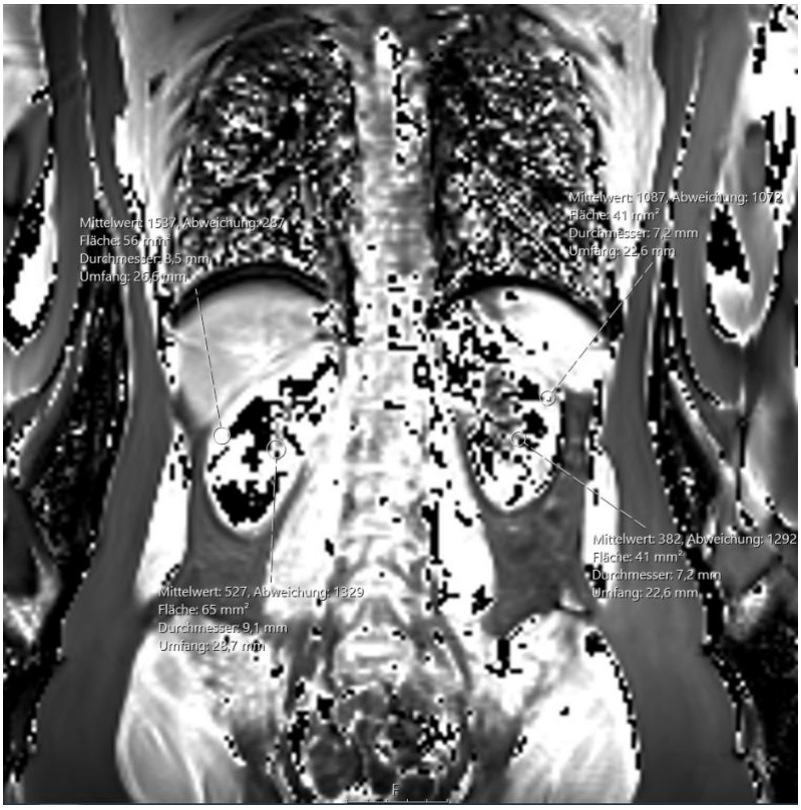

Figure 14: An example of T_1 Map measurement, acquired in PACS after processing in STROKETOOL. ROI drawings in cortex and medulla of both kidneys, with automated calculation of mean values.

T_2 mapping is an MRI technique used for constructing a parametric map, whose value shows the calculated T_2 relaxation time at each voxel. T_2 map can be analyzed quantitatively by drawing ROIs that are relevant for the tissue of interest and the pathology of interest. To construct a T_2 map, a minimum of three single-shot images is obtained at increasing T_2 preparation times. Those separate echo times (TE) are used to quantify the relaxation time decay [68]. The calculation of T_2 map has also been done by in-house developed STROKETOOL (Version 2.0, H.-J. Wittsack, DSI, Frechen, Germany), where the three TEs (12, 46, 81) have been run (Figure 15).

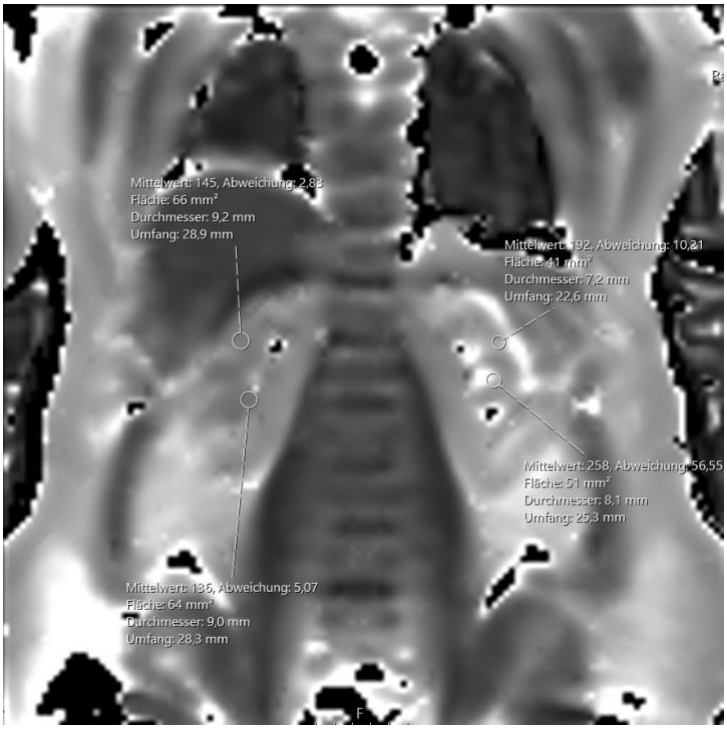

Figure 15: An example of T_2 Map measurement, acquired in PACS after processing in STROKETOOL. ROI drawings in cortex and medulla of both kidneys, with automated calculation of mean values.

3.5 MRI-Scanner

All MRI measurements were performed on a clinical 3T MR scanner (Magnetom Prisma, Siemens Healthineers AG, Erlangen, Germany).

The healthy subjects as well as the patients were all examined in a supine position. All examinations were performed with an eighteen-channel body coil. A 24-channel spine coil was used for the lumbar spine acquisition.

3.6 MRI-Sequences

The following section gives an overview of MRI-sequences used in this study. They were all performed without the use of a contrasting agent.

1) First, a T_2-weighted HASTE (Half-Fourier Acquisition Single-Shot Turbo Spin-Echo) sequence (t2_haste_tra) (t2_haste_cor) (t2_haste_sag_2loc) (t2_haste_cor_ang) was used. This is a single-section T_2-weighted sequence that uses a single excitation pulse together with half-

Fourier acquisition without respiratory triggering [74]. Coronal, axial, and sagittal images were acquired. This way, the complete anatomy of both the kidneys and the abdomen was acquired. For the HASTE image acquisition (Figure 16), the following sequence parameters were used:

Axial – 40 slices with slice thickness = 4 mm, field of view (FOV) = 296 x 380 mm, TR/TE (Time to Echo) = 1400/96 msec

Coronal – 40 slices with slice thickness = 5 mm, FOV = 380 x 380 mm, TR/TE = 1200/99 msec

Sagittal – 10 slices with slice thickness = 4 mm, FOV = 296 x 380 mm, TR/TE = 1400/96 msec

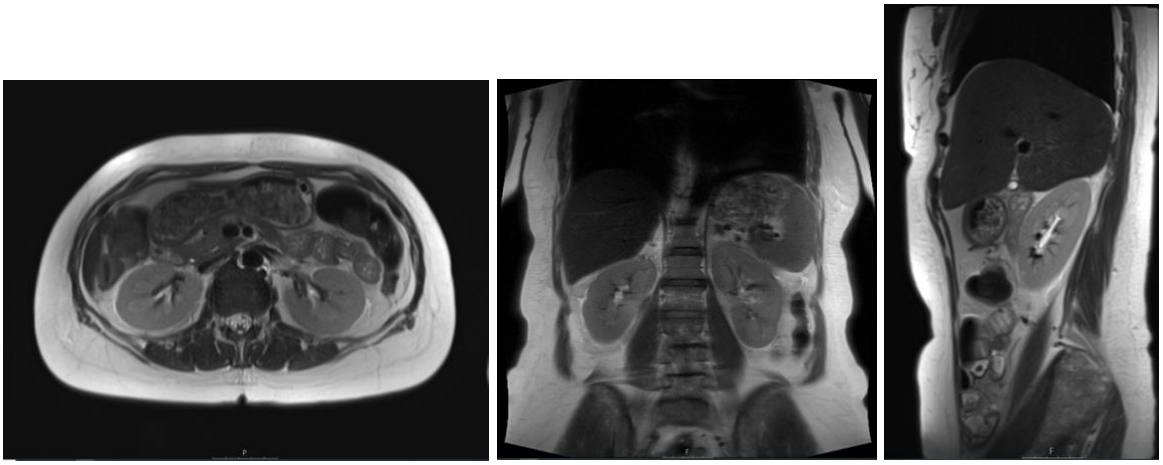

Figure 16: axial HASTE sequence on the left, coronal HASTE sequence in the middle, sagittal HASTE sequence on the right. Images acquired in PACS.

2) The next sequence performed was the coronal EPI (echo-planar imaging) sequence for DWI and DTI acquisition. EPI utilizes only one nuclear spin excitation per image and is able to obtain images very fast, in a fraction of a second [75]. The paracoronal EPI sequence along the kidney axis was acquired using the following parameters: 15 slices with slice thickness = 5 mm, FOV = 399 x 399 mm, TR/TE = 3000/78 msec, with b-value of 800 s/mm^2. An ADC and a FA map was obtained at each slice position (Figure 17).

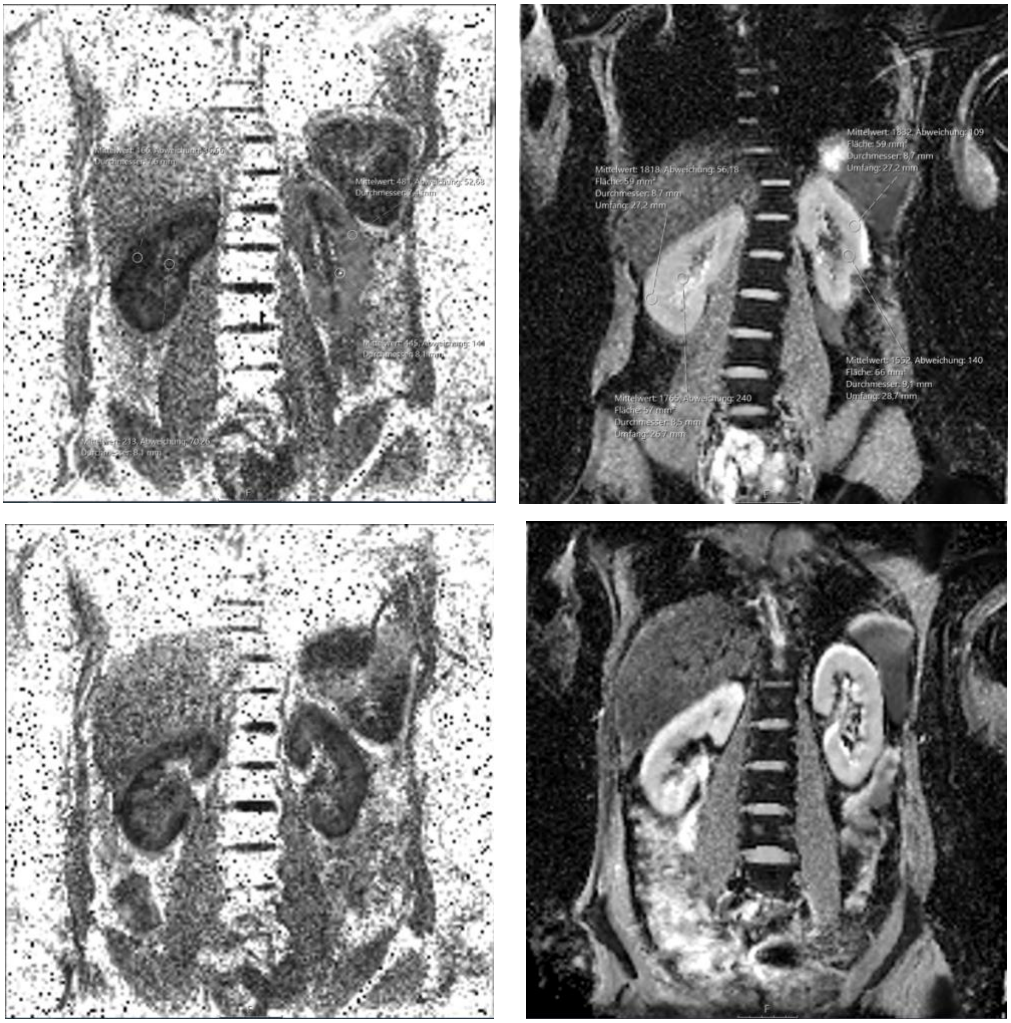

Figure 17: DTI FA sequence on the upper and lower left, DTI ADC sequence on the upper and lower right. ROI examples in upper left and right images. Images acquired in PACS.

3) A paracoronal FAIR True-FISP sequence was acquired next [76]. The following parameters were used for the acquisition: 60 slices with slice thickness = 8 mm, FOV = 400 x 400 mm, TR/TE = 5/2.5 msec.

In addition, a paracoronal M_0-True-FISP shot was made, before the FAIR True-FISP image was acquired and aligned to M_0-True-FISP (Figure 18). This is needed for the estimation of the tissue equilibrium magnetization (M_0). The estimated value of M_0 can then be used for the estimation of the perfusion rate (f) in the following equation [76]:

$$f = \frac{\lambda}{2TI} \frac{\Delta M(TI)}{M_0} \exp\left(\frac{TI}{T_1}\right)$$

f: perfusion rate (ml/100g/min)

λ: blood tissue water partition coefficient (constant value of 80ml/100g [77])

ΔM: difference in longitudinal magnetization between FAIR experiments with global and slice selective inversion

TI: inversion time (1 – 1.2 sec)

M_0: tissue equilibrium magnetization

T_1: longitudinal relaxation time of tissue

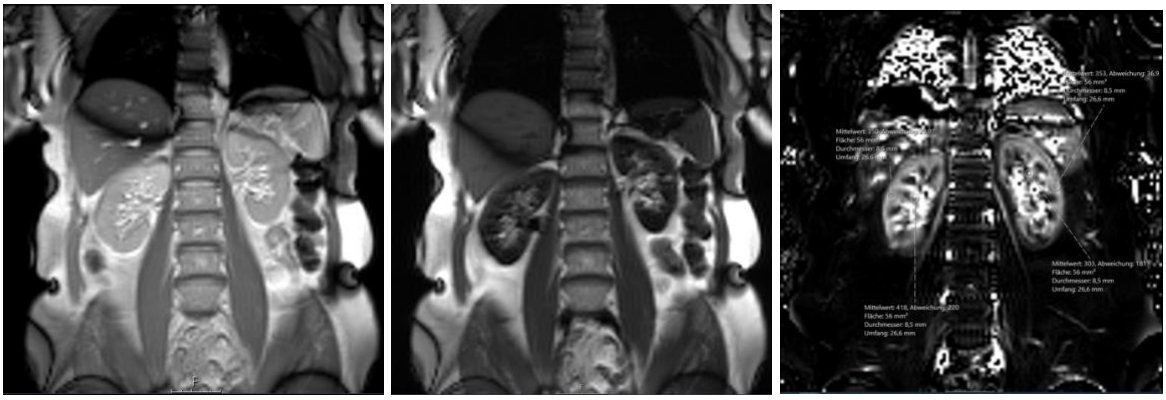

Figure 18: M_0-True-FISP sequence on the left, FAIR True-FISP sequence in the middle, ASL on the right with a ROI example. Images acquired in PACS.

4) The next sequence acquired was a paracoronal VIBE sequence for T_1 Mapping [78] (Figure 19). The parameters used for this sequence were: 12 slices with slice thickness = 5 mm, FOV = 399 x 399 mm, TR/TE = 5.06/1.69 msec.

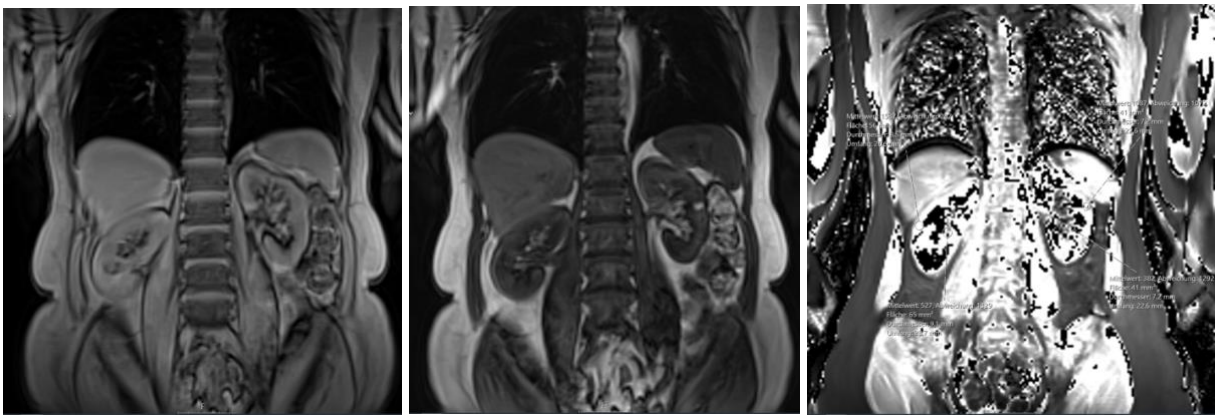

Figure 19: FLIP1 on the left, FLIP2 in the middle, T_1 Map on the right with a ROI example. Images acquired in PACS.

5) Subsequently, a coronal FLASH-2D-sequence (two-dimensional fast low angle shot) was performed [79]. The parameters used for the acquisition of this sequence were: 6 slices with slice thickness = 5 mm, FOV = 396 x 399 mm, TR/TE = 100/2.46 msec. This sequence was used to obtain a T_2*-Image and a T_2* Map (Figure 20).

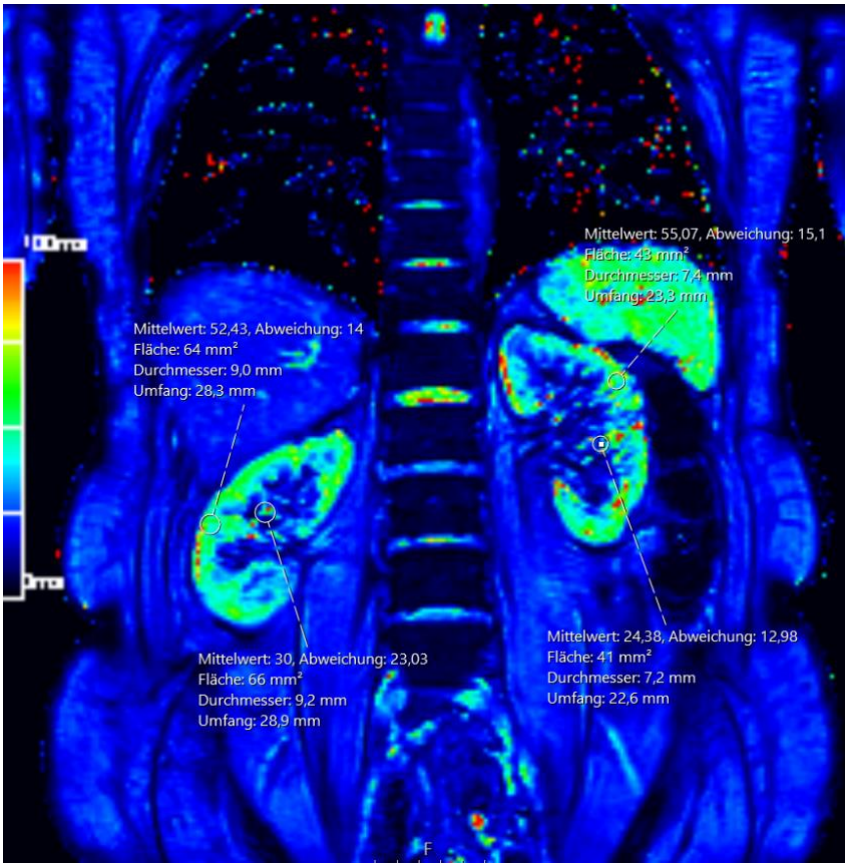

Figure 20: An example of T_2* measurement, acquired in PACS. ROI drawings in cortex and medulla of both kidneys, with automated calculation of mean values.

6) Coronal FSE (fast spin echo) or TSE (turbo spin echo) sequence was used for the creation of T_2 Map (Figure 21), acquired after processing, as described in 3.4.4 and 3.7 [80, 81]. The following parameters were used for the acquisition of this sequence: 3 slices with slice thickness = 5 mm, FOV = 400 x 400 mm, TR/TE = 2000/46 msec.

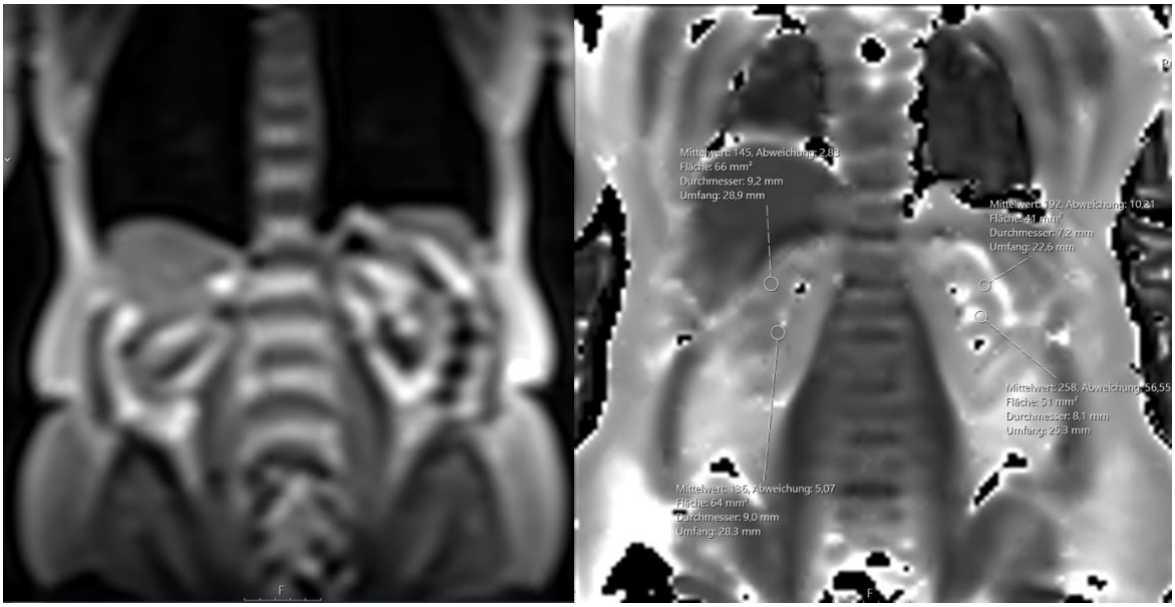

Figure 21: T2Map_cor_TE_12_46_81 on the left, processed T_2 Map on the right with an example of ROI drawings in cortex and medulla of both kidneys, with automated calculation mean values. Image acquired in PACS.

3.7 Image Analysis

The image quality was analyzed by evaluating resolution, clarity, sharpness, and lack of breathing-related motion artifacts. Sequences were repeated if motion artifacts were detected.

The system used for image analysis and ROI measurements was the clinic-owned system PACS (Picture Archiving and Communication System). ROI-based image analysis was performed separately for the left and right kidney, and a mean value for both kidneys was automatically calculated. For the analysis, one continuous ROI with a surface area of the circle ranging between 40 and 70 mm^2 was placed in the renal cortex and 3-5 ROIs in renal medulla, respectively (e.g., Figure 21).

The following previously mentioned parameters were measured using only the image analysis tools in PACS: ADC, FA and T_2*. For ASL, T_1 Map, and T_2 Map, additional image processing by in-house developed STROKETOOL (Version 2.0, H.-J. Wittsack, DSI, Frechen, Germany) was needed. In a second step, the images processed in STROKETOOL were exported back to PACS for ROI selection and mean value measurement.

3.8 Statistical Analysis

The acquired data was transferred to Microsoft Office Excel [82] for the first part of the statistical analysis. This included all the median and average values as well as the standard deviation, such as for the age statistics, accompanied by the t-tests for comparison between the groups. t-tests with two-tailed distribution and two-sample equal variance (homoscedastic) were used, with $p < 0.05$. The detailed analysis is shown in the appendix.

The subjects were divided into three groups based on the disease stadium, and one healthy group, as explained in 3.1 and 4.

Data analysis was performed by using the SPSS software (SPSS Statistics 29.0.2.0). To choose a suitable test for group comparisons, firstly a test of normality after Kolmogorov-Smirnov (KS) was conducted (Table V and VI, subchapter 4.2) to survey the data for normal distribution (homogeneity of variance). Depending on the homogeneity and heterogeneity of variance, two types of comparison tests were chosen for significance estimation, a parametric (ANOVA) and a nonparametric test (Kruskal-Wallis) respectively, each followed by adequate post-hoc tests, as explained in the following paragraphs (see 4.2). For this, the p-value of the t-tests was defined as $p < 0.05$.

As a final step, we performed a correlation analysis between the age of the subjects and each of the 6 parameters that were assessed in this study. For parametric data, the Pearson correlation analysis was performed. For the remaining non-parametric data, we performed the Spearman correlation analysis. For detailed correlation analysis, see 4.4 and appendix.

4. Results

4.1 Groups

There are four groups of participants in this study: acute, chronic, control, and healthy.

As mentioned in 3.1, all 36 patients were divided into three categories: subjects with acute kidney injury due to LN ("acute"), subjects with chronic kidney involvement ("chronic"), and SLE patients with no kidney involvement ("control") serving as a control group. The fourth group ("healthy") consisted of 10 healthy subjects. For each patient within each group, the six parameters previously mentioned in 3.4.1-3.4.5 were measured and the average values can be seen in the following Table IV.

Table IV: Comparison of the four groups of participants. Average values of age and six MRI parameters are shown, without differentiating between the right and the left kidney and cortex and medulla.

	acute	**chronic**	**control**	**healthy**
Number (N=46)	N=13	N=7	N=16	N=10
Number of women (N=31)	N=8	N=5	N=12	N=6
Number of men (N=15)	N=5	N=2	N=4	N=4
Age (in years)	43.38 ± 13.1	41.57 ± 10.8	53.06 ± 12.9	63.20 ± 6.9
ADC	1824.04 ± 275.76	1804 ± 227	1805 ± 225.68	1982 ± 98.69
FA	265.88 ± 105.83	259 ± 94	267 ± 106.22	211 ± 37.45
T_1 Map	725.69 ± 389.91	860 ± 346	700 ± 326.62	1156 ± 145.39
ASL	387.29 ± 192.29	323 ± 90	364 ± 110.04	296 ± 70.61

T_2*	50.26 ± 14.75	44 ± 14	47 ± 12.03	144 ± 23.75
T_2 Map	181.35 ± 56.58	160 ± 26	165 ± 33.84	167 ± 25.65

The following Figure 22 shows the graphical representation of the distribution of the groups, in accordance with the Table IV.

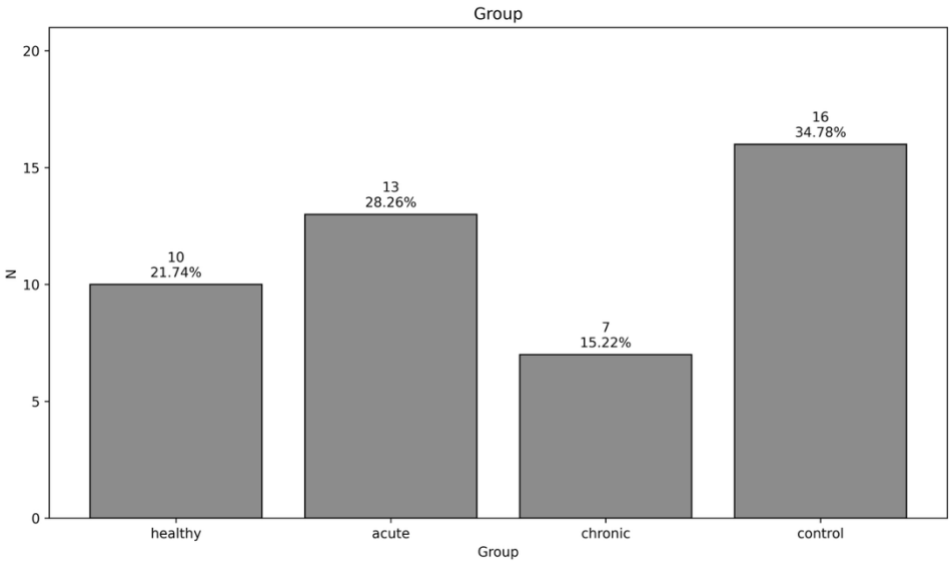

Figure 22: Distribution of all individuals throughout four groups.

4.2 SPSS Analysis

The results of the statistical analyses conducted with SPSS are presented in the following section. Tables V and VI portray a KS test of normality, as previously mentioned in 3.8.

Table V: Kolmogorov-Smirnov test of normality for ADC, FA, T_1 Map, ASL and T_2*. The parameters were sorted by the left and the right kidney and by cortex and medulla, with right and left kidney cortex marked respectively as RNC and LNC, right and left kidney medulla as RNM and LNM. The normally distributed data is marked by the asterisk (*) in the second column (Sig.) and is expressed as $p > 0.05$ (homogeneity of variance). Data where the level of significance was $p < 0.05$ is not normally distributed (heterogeneity of variance).

Tests of Normality	
Kolmogorov-Smirnov**	Sig.
Years	.200*
ADC_RNC	.200*

ADC_RNM	.043
ADC_LNC	.200*
ADC_LNM	.200*
FA_RNC	.200*
FA_RNM	.048
FA_LNC	.020
FA_LNM	.009
T1_Map_RNC	.003
T1_Map_RNM	.005
T1_Map_LNC	.027
T1_Map_LNM	.200*
ASL_RNC	.200*
ASL_RNM	.200*
ASL_LNC	.200*
ASL_LNM	.029
T2_RNC	<.001
T2_RNM	<.001
T2_LNC	<.001
T2_LNM	<.001

*. This is a lower bound of the true significance.
**. Lilliefors Significance Correction

Table VI: Kolmogorov-Smirnov test of normality for T_2 Map. The parameter T_2 Map was sorted by the left and the right kidney and by cortex and medulla, with right and left kidney cortex marked respectively as RNC and LNC, right and left kidney medulla as RNM and LNM. The normally distributed data is marked by the asterisk (*) in the second column (Sig.) and is expressed as $p > 0.05$ (homogeneity of variance). Data where the level of significance was $p < 0.05$ is not normally distributed (heterogeneity of variance).

Tests of Normality	
Kolmogorov-Smirnov**	
	Sig.
T2_Map_RNC	.036
T2_Map_RNM	.071
T2_Map_LNC	.132
T2_Map_LNM	.200*

*. This is a lower bound of the true significance.

**. Lilliefors Significance Correction

Depending on whether the data met the assumptions of normality and homogeneity of variance (3.8), appropriate statistical tests were selected: either parametric for normally distributed data or non-parametric alternatives for heterogeneity of variance (see below).

As noted above, if there was homogeneity of variance, pairwise comparisons were performed using a parametric, one-way analysis of variance (ANOVA). When it led to a significant result, it was followed up with post-hoc tests to see which particular groups showed significant differences. The post-hoc tests chosen were Tukey HSD (honestly significant difference) and Sidak. The next paragraph shows an example for this analysis, focused on parameter ADC.

As shown in Table V, the normality test after KS indicated that following parameters are normally distributed and thus homogenous: ADC RNC, LNC and LNM. Therefore, multiple groups were pairwise compared by conducting one-way ANOVA (e.g., ADC RNC, Table VII), with significant results being analyzed by post-hoc tests Sidak and Tukey HSD (e.g. Table VIII).

Table VII: ANOVA example, performed for ADC RNC. This shows the assessment of ADC in the right renal cortex. A significant result of $p < 0.01$ can be seen in the last column (Sig.) of the table.

ANOVA					
ADC_RNC					
	Sum of Squares	**df**	**Mean Square**	**F**	**Sig.**
Between Groups	383188.814	3	127729.605	5.820	.002
Within Groups	921741.295	42	21946.221		
Total	1304930.109	45			

Table VIII: Post hoc tests for significant ADC RNC ANOVA, Tukey HSD and Sidak. Two post hoc tests were performed, since ANOVA detected a significant difference for this example's measured parameter ADC RNC. The column marked by "Sig." shows a significant difference for the comparison between healthy subjects and acute group, as well as between acute group and control group, with *p*-values respectively $p < 0.01$ and $p < 0.05$. Detailed data can be seen in appendix.

Multiple Comparisons				
Dependent Variable: ADC_RNC				
	(I) Group	(J) Group	Mean Difference (I-J)	Sig.
Tukey HSD	healthy	acute	247.500*	.002
		chronic	125.643	.326
		control	77.938	.565
	acute	healthy	-247.500*	.002

		chronic	-121.857	.309
		control	-169.563*	.019
	chronic	healthy	-125.643	.326
		acute	121.857	.309
		control	-47.705	.892
	control	healthy	-77.938	.565
		acute	169.563*	.019
		chronic	47.705	.892
Sidak	healthy	acute	247.500*	.002
		chronic	125.643	.442
		control	77.938	.736
	acute	healthy	-247.500*	.002
		chronic	-121.857	.419
		control	-169.563*	.023
	chronic	healthy	-125.643	.442
		acute	121.857	.419
		control	-47.705	.981
	control	healthy	-77.938	.736
		acute	169.563*	.023
		chronic	47.705	.981

*. The mean difference is significant at the 0.05 level.

However, if there was heterogeneity of variance in the data assessed by the normality test, a non-parametric (NPar) test was conducted, in particular the Kruskal-Wallis test (e.g. Table IX). Since a significant Kruskal-Wallis test does not identify where exactly the significance occurs, Mann-Whitney was chosen as a post-hoc NPar test to specify the significant results (e.g. Table X). Detailed data can be found in appendix.

Table IX: Kruskal-Wallis Test, performed for FA LNM. An example of a significant result acquired by performing a non-parametric Kruskal-Wallis Test for FA LNM is shown. The Kruskal-Wallis test found a significant difference of $p < 0.01$, as shown on the right.

Kruskal-Wallis Test Ranks			
Group		**N**	**Mean Rank**
FA_LNM	Healthy subjects	10	10.00
	Acute	13	23.73
	Chronic	7	26.93
	Control	16	30.25
	Total	46	

Test Statistics [a,b]	
	FA_LNM
Kruskal-Wallis H	14.627
df	3
Asymp. Sig.	.002

a. Kruskal Wallis Test
b. Grouping Variable: Group

Table X: Post hoc test, Mann-Whitney. This test was performed for further specifying which groups were exactly significantly different, by applying it pairwise for each group, so that they were all compared to each other. This table shows a comparison between healthy subjects and patients with chronic changes of the kidney. The parameter measured was FA of the left kidney's medulla (FA LNM). The post hoc Mann-Whitney test showed a significant difference with $p < 0.01$, expressed as the exact significance in the last column of the table.

	Group	**N**	**Exact Sig.**
FA_LNM	healthy	10	< .001
	chronic	7	
	total	17	

4.3 Assessment of Individual Parameters

For each parameter, all four groups—healthy, acute, chronic, and control (Table IV) were pairwise compared to each other statistically (as explained in 4.2), while separating between the position of the kidney (left or right) and the region in the kidney (cortex and medulla) (e.g. right renal cortex of one group vs. right renal cortex of the other group etc.). The results were portrayed in graphs created in Microsoft Office Excel (Figure 23-28). Detailed data analysis was conducted in the SPSS 29.0.2.0, as explained in subchapter 3.8 and 4.2. The concrete results of this analysis can be seen in each parameter's subchapter, from 4.3.1-4.3.6.

4.3.1 ADC

Figure 23 shows a graph representing the significance level for every single measurement related to this section's relevant parameter ADC, both for the right and left kidney's cortex and medulla, for every single comparison between the four groups of subjects.

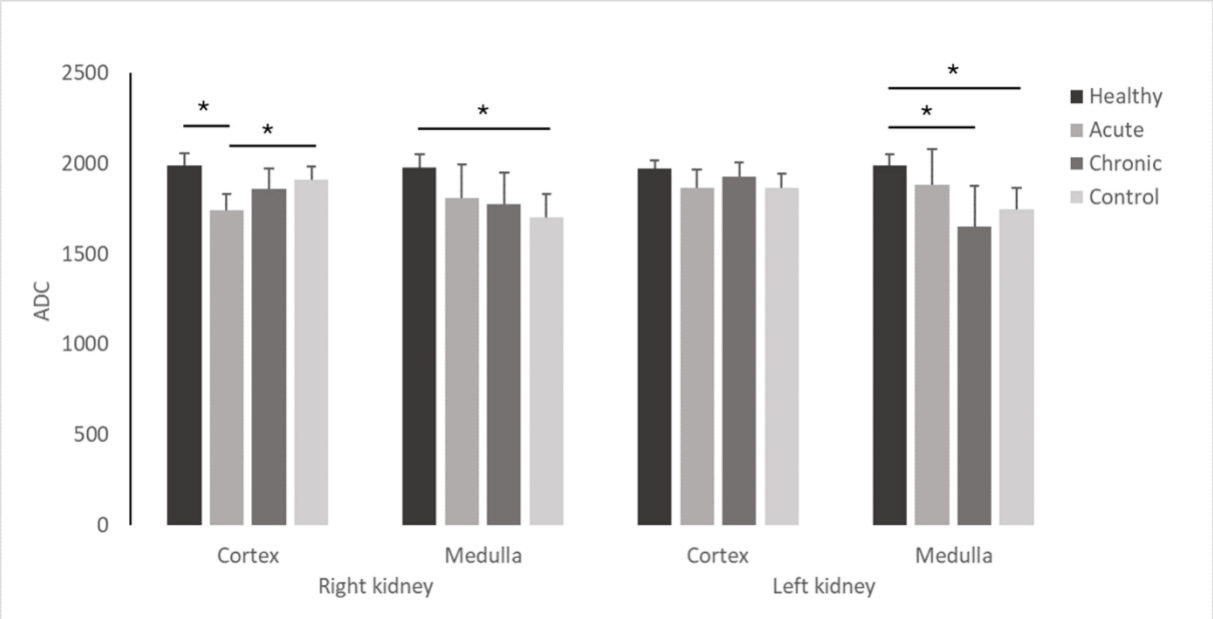

Figure 23: Comparison of apparent diffusion coefficient (ADC) values in renal cortex and medulla across all four study groups.

The x-axis is subdivided into right and left kidney, allowing for side-specific comparison, while the y-axis displays the mean ADC values. Statistically significant differences are indicated by connecting bars and asterisks (*; $p < 0.05$, 95% CI). Significant reductions in ADC were detected in both cortex and medulla when comparing healthy groups with patients suffering from lupus nephritis, independent of the extent of renal involvement.

The mean values along with the standard deviation (SD) can be found in Table XI.

The graph shows that ADC values differ significantly between the 4 compared groups. In at least one measured kidney area, the healthy group displayed significantly higher values compared to the control group ($p < 0.01$), acute group ($p < 0.01$), and the chronic group ($p < 0.05$). This highlights that disease status is associated with a reduction in ADC values, with a moderate effect size. All significant group differences are indicated by the asterisk (*). Table XI shows mean ADC values across all four groups.

Table XI: Group-wise mean (± SD) ADC values for the right and left kidneys, stratified by region (cortex, medulla).

Group	N	ADC_RNC Mean	ADC_RNM Mean	ADC_LNC Mean	ADC_LNM Mean
Healthy subjects	10	1987.50 ± 110.508	1975.30 ± 124.848	1974.30 ± 68.033	1989.03 ± 97.882
Acute	13	1740.00 ± 166.938	1808.77 ± 338.050	1863.54 ± 189.067	1883.85 ± 363.066
Chronic	7	1861.86 ± 150.143	1773.86 ± 235.115	1928.57 ± 100.854	1650.43 ± 306.029
Control	16	1909.56 ± 151.031	1700.38 ± 271.195	1865.00 ± 164.696	1745.00 ± 243.770
Total	46	1871.33 ± 170.289	1801.96 ± 275.609	1898.02 ± 151.741	1822.90 ± 288.710

4.3.2 FA

Figure 24 shows a graph representing the parameter FA, both for the right and left kidney's cortex and medulla, for all four groups.

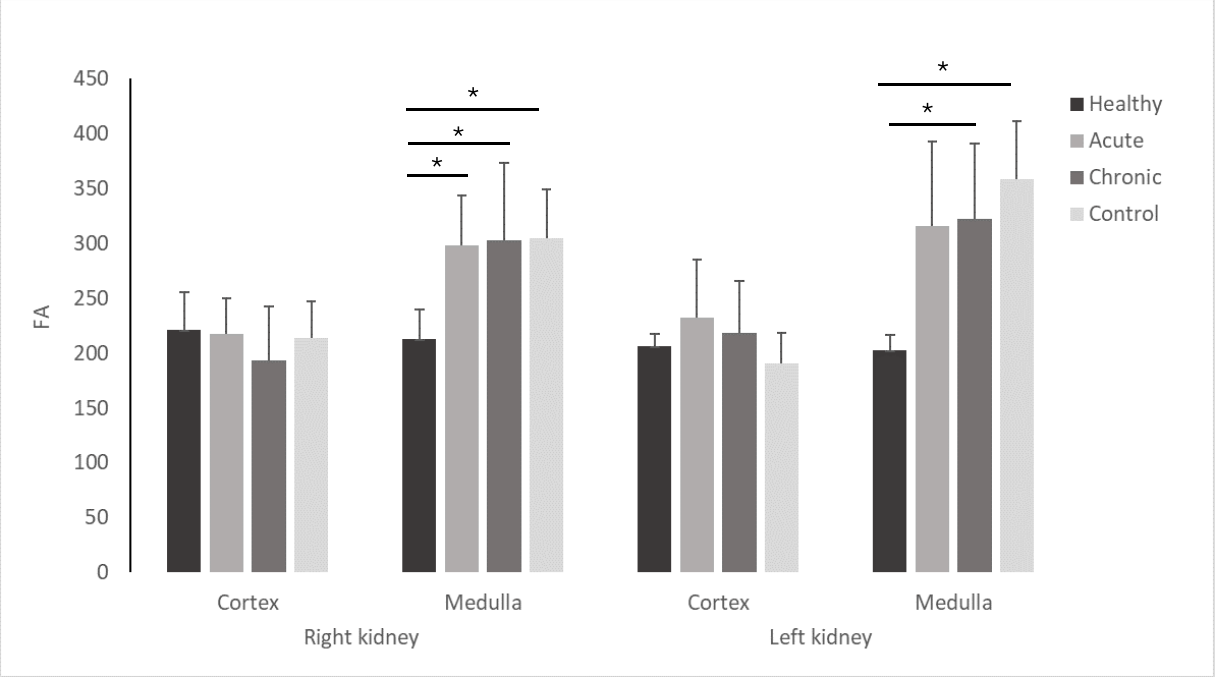

Figure 24: Comparison of fractional anisotropy (FA) values in renal cortex and medulla across all four study groups.

The x-axis is subdivided into right and left kidney, allowing for side-specific comparison, while the y-axis displays the mean FA values. Statistically significant differences are indicated by connecting bars and asterisks (*; $p < 0.05$, 95% CI). Significant increases in FA were detected in medulla when comparing healthy groups with patients suffering from lupus nephritis, independent of the extent of renal involvement.

The mean values along with the standard deviation (SD) can be found in Table XII.

The graph shows significant differences of FA values between the 4 compared groups. In at least one measured kidney area, the diseased groups (acute, chronic, control) often displayed significantly higher values compared to the healthy group ($p < 0.01$ for healthy vs. acute and healthy vs. control, and $p < 0.05$ for healthy vs. chronic). This suggests that disease status is associated with an increase in FA values, with a large effect size. All significant group differences are indicated by (*). Table XII shows mean FA values across all four groups.

Table XII: Group-wise mean (± SD) FA values for the right and left kidneys, stratified by region (cortex, medulla).

Group	N	FA_RNC Mean	FA_RNM Mean	FA_LNC Mean	FA_LNM Mean
Healthy subjects	10	221.00 ± 56.455	212.97 ± 42.686	206.20 ± 17.993	202.37 ± 22.881
Acute	13	217.69 ± 59.298	297.92 ± 84.502	232.15 ± 97.338	315.77 ± 141.099
Chronic	7	193.45 ± 65.919	303.00 ± 94.824	218.71 ± 63.710	322.00 ± 93.477
Control	16	213.38 ± 68.475	304.75 ± 90.214	190.56 ± 57.543	358.81 ± 106.955
Total	46	213.22 ± 61.623	282.60 ± 86.976	210.00 ± 67.286	307.04 ± 117.629

4.3.3 T_1 Map

Figure 25 shows a graph representing the parameter T_1 Map, both for the right and left kidney's cortex and medulla, for all four groups.

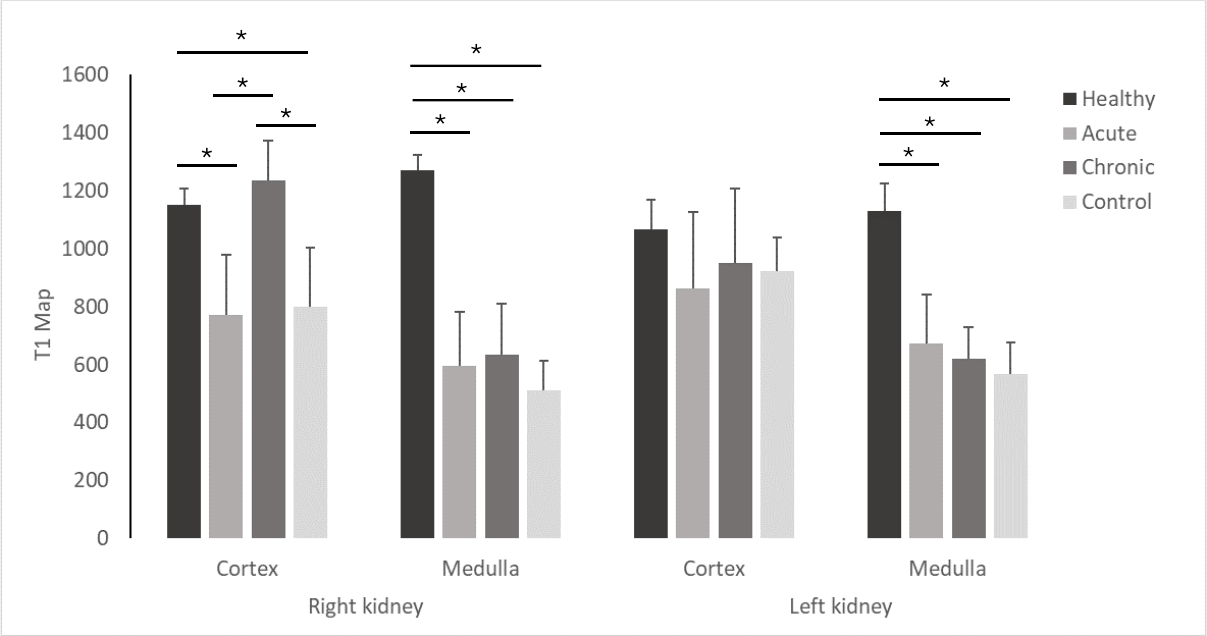

Figure 25: Comparison of T_1 Map values in renal cortex and medulla across all four study groups.

The x-axis is subdivided into right and left kidney, allowing for side-specific comparison, while the y-axis displays the mean T_1 Map values. Statistically significant differences are indicated by connecting bars and asterisks (*; $p < 0.05$, 95% CI). Significant reductions in T_1 Map were detected in both cortex and medulla when comparing healthy groups with patients suffering from lupus nephritis, independent of the extent of renal involvement.

The mean values along with the standard deviation (SD) can be found in Table XIII.

The graph illustrates significant differences in T_1 Map values among the four groups. Overall, in most measured kidney areas, the healthy group exhibited higher T_1 Map values compared to the acute, chronic, and control groups ($p < 0.05$). These findings indicate that the presence of disease is associated with reduced T_1 Map values, with large effect sizes. Additional significant group differences are marked with (*). Table XIII shows mean T_1 Map values across all four groups.

Table XIII: Group-wise mean (± SD) T_1 Map values for the right and left kidneys, stratified by region (cortex, medulla).

Group	N	T_1 Map_RNC Mean	T_1 Map_RNM Mean	T_1 Map_LNC Mean	T_1 Map_LNM Mean
Healthy subjects	10	1152.30 ± 90.652	1271.27 ± 87.023	1066.90 ± 166.553	1131.60 ± 154.328
Acute	13	770.77 ± 387.191	596.38 ± 340.948	861.38 ± 490.703	674.23 ± 309.888
Chronic	7	1236.14 ± 183.589	634.00 ± 240.662	949.71 ± 351.901	621.71 ± 146.913
Control	16	801.19 ± 417.783	510.19 ± 209.580	922.56 ± 240.273	566.19 ± 224.902
Total	46	935.11 ± 378.226	718.84 ± 378.979	940.78 ± 333.166	728.09 ± 313.385

4.3.4 ASL

Figure 26 shows a graph representing the parameter ASL, both for the right and left kidney's cortex and medulla, for all four groups.

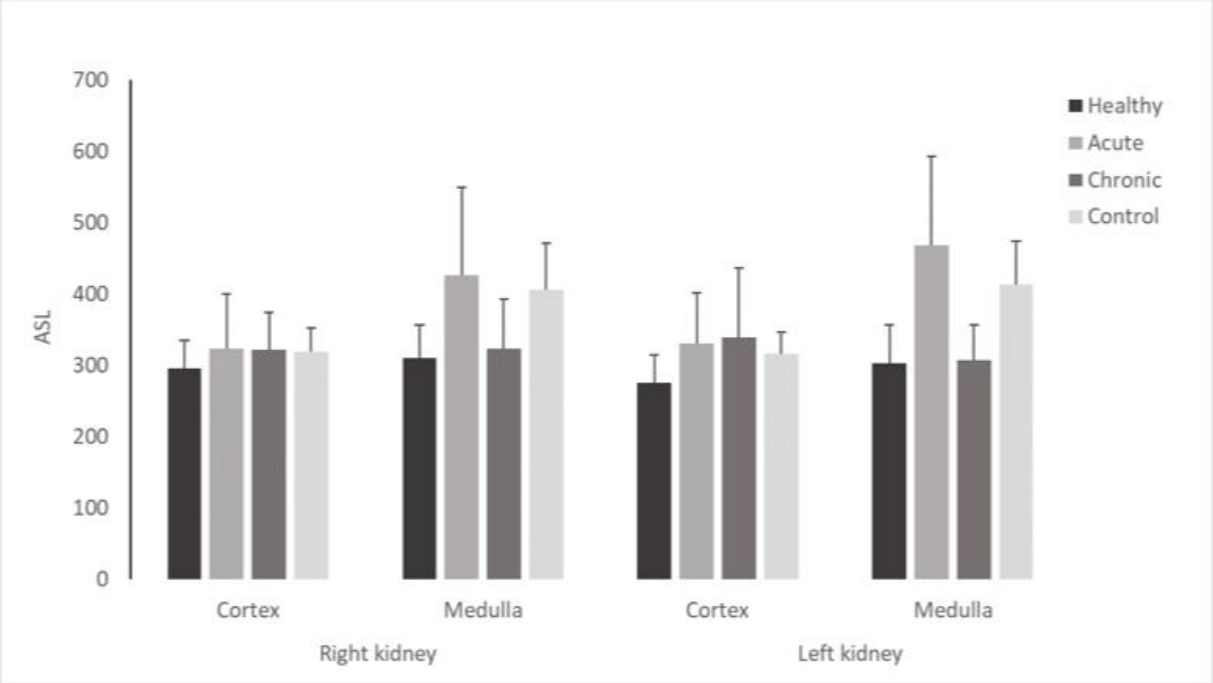

Figure 26: Comparison of arterial spin labeling (ASL) values in renal cortex and medulla across all four study groups.

The x-axis is subdivided into right and left kidney, allowing for side-specific comparison, while the y-axis displays the mean ASL values. Statistically significant differences are indicated by connecting bars and asterisks (*; $p < 0.05$, 95% CI). No significant differences were detected in ASL when comparing healthy groups with patients suffering from lupus nephritis, independent of the extent of renal involvement.

The mean values along with the standard deviation (SD) can be found in Table XIV.

The graph shows the ASL values in the kidney for the four groups. No significant differences were observed between groups, as indicated by the absence of asterisks (*). This suggests that disease status did not markedly affect ASL values. Table XIV shows mean ASL values across all four groups.

Table XIV: Group-wise mean (± SD) ASL values for the right and left kidneys, stratified by region (cortex, medulla).

Group	N	ASL_RNC Mean	ASL_RNM Mean	ASL_LNC Mean	ASL_LNM Mean
Healthy subjects	10	295.60 ± 62.624	310.53 ± 73.467	275.40 ± 63.738	302.97 ± 86.377
Acute	13	323.92 ± 140.309	426.58 ± 227.038	331.00 ± 130.849	467.68 ± 228.795
Chronic	7	322.57 ± 70.007	323.86 ± 93.316	339.00 ± 131.834	307.43 ± 67.228
Control	16	319.06 ± 69.455	406.25 ± 132.797	316.31 ± 63.025	413.00 ± 124.035
Total	46	315.87 ± 91.740	378.65 ± 155.875	315.02 ± 97.633	388.47 ± 160.795

4.3.5 T_2*

Figure 27 shows a graph representing the parameter T_2*, both for the right and left kidney's cortex and medulla, for all four groups.

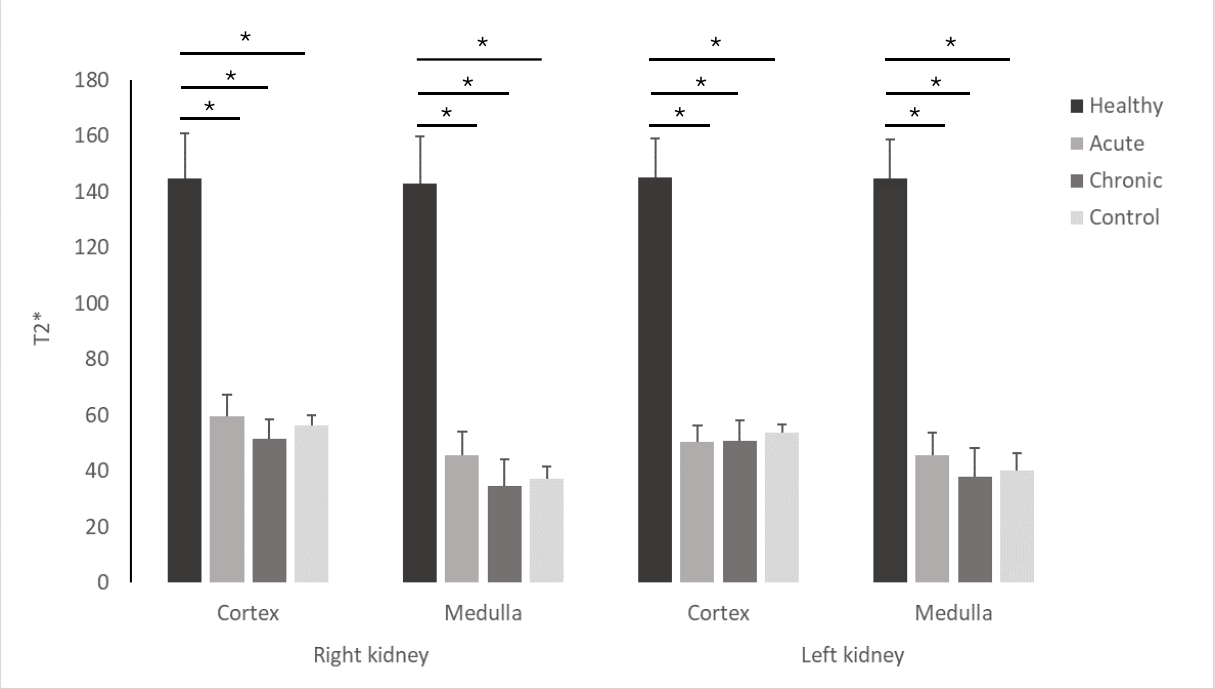

Figure 27: Comparison of T_2* values in renal cortex and medulla across all four study groups.

The x-axis is subdivided into right and left kidney, allowing for side-specific comparison, while the y-axis displays the mean T_2* values. Statistically significant differences are indicated by connecting bars and asterisks (*; $p < 0.05$, 95% CI). Significant reductions in T_2* were detected in both cortex and medulla when comparing healthy groups with patients suffering from lupus nephritis, independent of the extent of renal involvement.

The mean values along with the standard deviation (SD) can be found in Table XV.

The graph demonstrates significant group differences in T_2* values. Across all comparisons, the healthy group showed consistently higher values than the acute, chronic, and control groups ($p < 0.01$). These results emphasize that disease status is uniformly associated with a marked reduction in T_2* values, with very large effect sizes. Additional significant group differences are marked with (*). Table XV shows mean T_2* values across all four groups.

Table XV: Group-wise mean (± SD) T_2* values for the right and left kidneys, stratified by region (cortex, medulla).

Group	N	T_2*_RNC Mean	T_2*_RNM Mean	T_2*_LNC Mean	T_2*_LNM Mean
Healthy subjects	10	144.80 ± 25.905	143.03 ± 27.231	145.00 ± 22.499	144.60 ± 22.849
Acute	13	59.42 ± 14.243	45.58 ± 15.749	50.41 ± 11.111	45.63 ± 14.583
Chronic	7	51.59 ± 9.455	34.49 ± 13.065	50.95 ± 9.825	37.90 ± 14.031
Control	16	56.16 ± 7.475	37.20 ± 8.633	53.53 ± 6.267	40.25 ± 12.347
Total	46	75.66 ± 39.782	62.16 ± 46.212	72.14 ± 40.857	64.10 ± 45.671

4.3.6 T_2 Map

Figure 28 shows a graph representing the parameter T_2 Map, both for the right and left kidney's cortex and medulla, for all four groups.

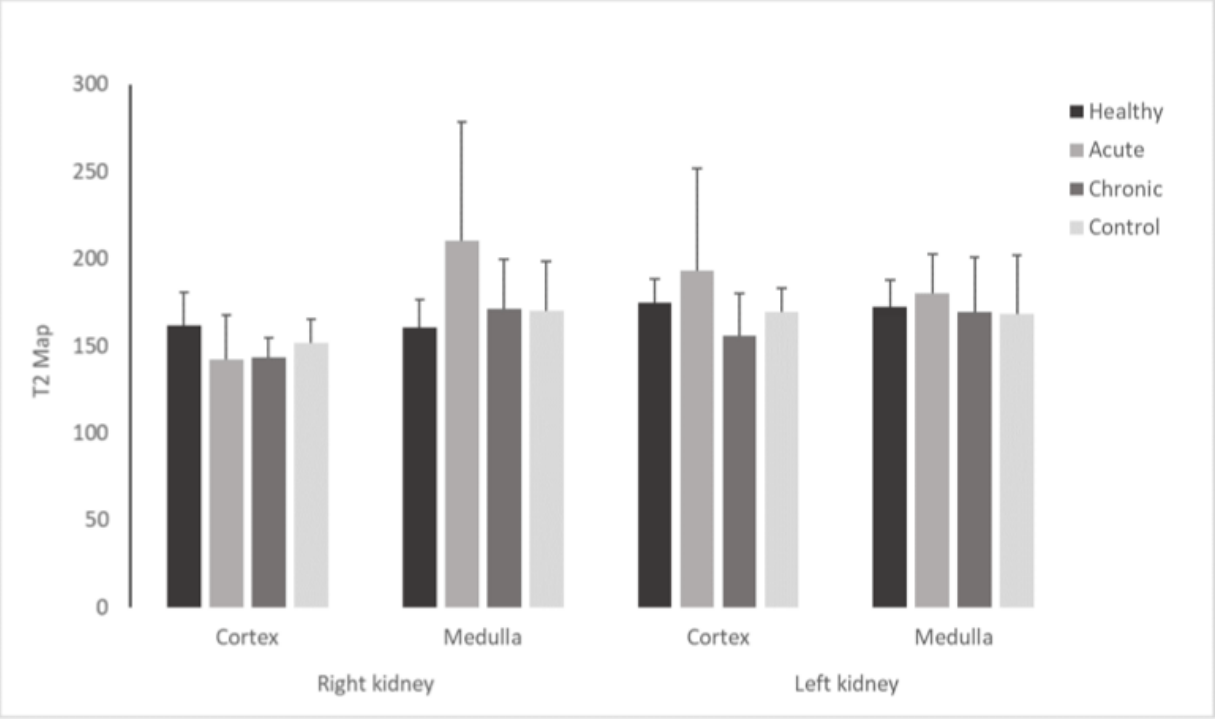

Figure 28: Comparison of T_2 Map values in renal cortex and medulla across all four study groups.

The x-axis is subdivided into right and left kidney, allowing for side-specific comparison, while the y-axis displays the mean T_2 Map values. Statistically significant differences are indicated by connecting bars and asterisks (*; $p < 0.05$, 95% CI). No significant differences were detected in T_2 Map when comparing healthy groups with patients suffering from lupus nephritis, independent of the extent of renal involvement.

The mean values along with the standard deviation (SD) can be found in Table XVI.

The graph shows the T_2 Map values across the four groups. No statistically significant differences were observed between the groups. For this parameter, not all 46 participants of the study were included in the statistical assessment, as measurements could not be obtained in some MRIs. Therefore, a total of 27 subjects were analyzed for T2 Map, as also detailed in Table XVI.

Table XVI: Group-wise mean (± SD) T_2 Map values for the right and left kidneys, stratified by region (cortex, medulla).

Group	N	T_2 Map_RNC Mean	T_2 Map_RNM Mean	T_2 Map_LNC Mean	T_2 Map_LNM Mean
Healthy subjects	10	161.80 ± 30.360	160.70 ± 25.913	174.80 ± 22.125	172.43 ± 24.384
Acute	5	142.40 ± 28.815	210.20 ± 78.187	193.00 ± 66.798	179.80 ± 26.338
Chronic	4	143.25 ± 11.383	171.25 ± 29.022	156.00 ± 24.617	169.25 ± 32.387
Control	8	151.88 ± 19.431	169.75 ± 41.202	169.38 ± 20.135	168.38 ± 48.308
Total	27	152.52 ± 25.091	174.11 ± 45.320	173.78 ± 34.074	172.12 ± 32.846

4.4 Correlation Analysis with Age Consideration

As a final step of data analysis, a correlation analysis was performed (as previously mentioned in 3.8) between the age of the subjects and each of the 6 parameters that were assessed in this study. For parametric data, such as ADC (RNC, RNM, LNC, LNM), FA (RNC, RNM, LNC), T_1 Map (LNM), ASL (RNC, RNM, LNC), and T_2 Map (RNC, RNM, LNC, LNM), the Pearson correlation analysis was performed. For the remaining non-parametric data, which included parameters FA (LNM), T_1 Map (RNC, RNM, LNC), ASL (LNM), and T_2* (RNC, RNM, LNC, LNM), the Spearman correlation analysis was conducted. Detailed correlation analysis data can be found in appendix (Table XXIV-XXXVII). The following sections show examples of the correlation results.

4.4.1 Pearson Correlation Analysis

Table XVII: Pearson correlation analysis, a linear correlation between two variables – years vs. ADC – in right and left renal cortex and medulla. Significant values are marked by the asterisk (*) and the *p*-values are listed in the "Sig." - row.

		ADC_RNC	ADC_RNM	ADC_LNC	ADC_LNM
Years	Pearson Correlation	.307*	-.154	.172	-.002
	Sig. (2-tailed)	.038	.306	.254	.987

*. Correlation is significant at the 0.05 level (2-tailed)

**. Correlation is significant at the 0.01 level (2-tailed)

Moderate evidence for positive correlation between the subject's age and ADC of right renal cortex (0.307*) is indicated by $p < 0.05$. This suggests that older patients may have higher ADC RNC values. There were no significant correlations for the medulla.

Table XVIII: Pearson correlation analysis, a linear correlation between two variables – years vs. ASL – in right and left renal cortex and right renal medulla. Significant values are marked by the asterisk (*)(**) and the *p*-values are listed in the "Sig." - row.

		ASL_RNC	ASL_RNM	ASL_LNC
Years	Pearson Correlation	-.382**	-.367*	-.465**
	Sig. (2-tailed)	.009	.012	.001

*. Correlation is significant at the 0.05 level (2-tailed)

**. Correlation is significant at the 0.01 level (2-tailed)

Table XVIII shows strong evidence for negative correlation (-.382**, e.g. ASL_RNC) between the subject's age and the parameter ASL, as indicated by $p < 0.01$ and $p < 0.05$. This confirms that older subjects tend to have lower ASL values.

4.4.2 Spearman Correlation Analysis

Table XIX: Spearman correlation analysis, a correlation between two ranked variables – years vs. T_1 Map – in right and left renal cortex and right renal medulla. Significant values are marked by the asterisk (**) and the *p*-values are listed in the "Sig." - row.

		T_1 Map_RNC	T_1 Map _RNM	T_1 Map _LNC
Years	Spearman's rho Correlation Coefficient	-.054	.378**	-.066
	Sig. (2-tailed)	.721	.010	.661

*. Correlation is significant at the 0.05 level (2-tailed)

**. Correlation is significant at the 0.01 level (2-tailed)

There was strong evidence for positive correlation (.378**) between the subject's age and T_1 Map of right renal medulla, indicated by $p = 0.01$. This indicates that older patients may have higher T_1 Map RNM values. There were no significant correlations for the cortex.

Table XX: Spearman correlation analysis, a correlation between two ranked variables – years vs. T_2* – in right and left renal cortex and medulla. Significant values are marked by the asterisk (*) and the *p*-values are listed in the "Sig." - row.

		T_2*_RNC	T_2*_RNM	T_2*_LNC	T_2*_LNM
Years	Spearman's rho Correlation Coefficient	.217	.064	.344*	.154
	Sig. (2-tailed)	.148	.674	.019	.308

*. Correlation is significant at the 0.05 level (2-tailed)

**. Correlation is significant at the 0.01 level (2-tailed)

There was moderate evidence for positive correlation (.344*) between the subject's age and T_2* of left renal cortex, indicated by $p < 0.05$. This suggests that older patients may have higher T_2* LNC values. There were no significant correlations for the medulla.

No significant correlations with age were observed for the other measured parameters, suggesting that these metrics are not age dependent.

5. Discussion

Non-invasive, contrast-free functional mpMRI has gained increasing attention as a promising approach for the evaluation of renal disease as a potential alternative to renal biopsy and its many limitations and repercussions. Imaging is no longer limited to the anatomical visualization of the kidney, but now enables the quantification of physiological and functional parameters, thereby offering indirect insight into renal microstructure [10, 83-86]. Renal mpMRI parameters applied in this study (see 3.4) enable quantification of key physiological functions of the kidney, including diffusion, anisotropy, and perfusion. These functions are known to be altered or impaired in the presence of renal disease. In this work, these parameters were investigated with the aim of developing renal imaging biomarkers that could complement, or guide, renal biopsy in the evaluation of rheumatic diseases, in particular lupus nephritis. Findings of this study demonstrated multiple significant differences between healthy and diseased renal function, although not all parameters reached statistical significance. The following subchapters (5.1-5.6) provide a more detailed discussion of each parameter. Additionally, the results of age correlation analysis are discussed, answering the question whether age is a relevant confounder. Subchapter 5.8 addresses the limitations inherent to the methods of measurement for these parameters.

5.1 ADC

Renal DWI MRI provides non-invasive insights into kidney function as well as the extent of tissue fibrosis or inflammatory processes [1].

Our measurements showed that ADC values were frequently significantly reduced in SLE patients with acute and chronic kidney impairment, as well as in the control group without LN, when compared to healthy participants (Figure 23). This observation supports the notion that disease status is associated with impaired renal microstructure, which is reflected by lower diffusion capacity. These results are in line with previous reports [1, 87-91] demonstrating decreased ADC values in diseased renal tissue, thereby reinforcing the potential of diffusion-weighted MRI as a non-invasive marker of renal pathology [1].

Multiple studies [90, 91] have proven correlation between decreased ADC and renal disease. There are multiple processes of water transport in normal renal function. Decaying renal

function, seen in GFR reduction, leads to a decreased rate of water reabsorption and its transfer across renal tubular system and therefore to a reduction of diffusion. Chronic renal dysfunction eventually leads to fibrosis which further restricts water diffusion [16]. There are several studies that show positive correlation between ADC and GFR [87, 88]. Another example was provided by *Fukuda et al.* [89], showing that patients with elevated serum creatinine levels exhibited lower renal ADC values compared to those with normal serum creatinine. However, it is difficult to choose a clear cut-off point for ADC values with the aim of clearly differentiating CKD vs. healthy kidney. By evaluating multiple studies, a systematic review by *Caroli et al.* [55] showed that this is due to high inter-individual variability as well as image resolution and protocol variability.

5.2 FA

Within this study, medullary FA values were usually significantly elevated in SLE patients compared to healthy participants, while cortical FA showed no significant differences in our study (Figure 24). *Caroli et al.* [55] assessed multiple studies reporting anisotropy values and came to the conclusion that there is generally a higher degree of anisotropy within the medulla in comparison to the cortex. This observation was explained by a presumption that there is a predominant water motion alongside tubular and vascular bundles of pyramids [55]. Furthermore, *Lanzman et al.* [92] also showed that medullary FA was significantly higher than cortical FA in both native and transplanted kidneys.

Consistent with our observation of higher anisotropy in diseased kidneys, some previous studies have also demonstrated elevated FA in pathological kidneys [93-95]. *Razek et al.* [93] showed that cortical FA was significantly higher in patients with LN than in healthy controls, with the assumption that severe inflammatory changes in the glomeruli caused this. Studies of early diabetic nephropathy, like *Saini et al.* [94] and *Chen et al.* [95], reported an initial and not always statistically significant medullary FA increase in early diabetic nephropathy and in normo-albuminuric diabetics compared with controls, interpreted as possible hyperfiltration-related early microstructural change. While the precise mechanisms remain uncertain, the increase in FA possibly reflects early microstructural alterations in renal tissue associated with kidney injury.

Further, the broader literature is heterogeneous, with multiple studies showing reduced renal FA in established disease instead, such as in CKD, diabetic kidney disease (DKD), and autosomal recessive polycystic kidney disease (ARPKD) [30, 64, 96-98]. For example, *Wang et al.* [96] reported that both cortical and medullary FA were significantly lower in CKD patients than in healthy volunteers. This is explained by the fact that anisotropy reflects the preferred diffusion direction. Therefore, in well-organized tissues like renal tubules, FA is high; when tissue becomes disorganized by a chronically progressing disease or inflammation, FA declines [99].

In summary, FA appears to diverge across renal diseases: it tends to decrease in conditions marked by progressive disruption of renal microarchitecture (e.g. CKD, DKD, ARPKD), whereas in LN, particularly in earlier or more active inflammatory stages, FA may appear elevated relative to healthy controls. This pattern in LN may reflect reduced isotropic motion (e.g., due to inflammatory cellularity/edema) with preserved radial tubular organization, whereas advancing fibrosis/chronicity and tubular atrophy eventually drive FA downward, thus aligning LN with to CKD-like patterns [93, 97-100].

Apparent inconsistencies across studies likely stem from differences in disease stage/class and treatment, as well as methodological factors such as ROI definition (cortex vs. medulla), partial-volume effects, and acquisition/processing parameters. This heterogeneity therefore underscores that FA is sensitive to stage-specific and compartment-specific pathology, highlighting the need for standardized protocols and stage-specific analyses.

5.3 T_1 Map

Across most sampled renal regions in this study, patients with LN (acute, chronic, control) had lower T_1 Map values than healthy participants, with multiple comparisons being statistically significant ($p < 0.05$). This pattern suggests an association between disease status and reduced T_1 Map, suggesting that T_1 mapping is sensitive to disease-related alterations in renal tissue. An exception to these results was reported in the cortical T_1 Map of the right kidney, with increased T_1 Map values in SLE patients with chronic changes of the kidney when compared to healthy participants (Figure 25). The observed left–right asymmetry could stem from methodological factors (e.g. positioning, coil sensitivity, ROI placement) and should be interpreted with caution.

Evidence for lower renal T_1 Map in LN vs. healthy is rare, as most studies report increased T_1 Map with active/former LN and with CKD/fibrosis [64, 101-104]. A human study that does show reduced T_1 Map in specific disease settings is *Aslam et al.* [105], which researched renal allograft rejection subtype and reported lower T_1 Map values (particularly in the medulla) in transplant recipients with cellular rejection compared to non-rejecting grafts and humoral rejection. Although not compared to healthy subjects, it demonstrates a disease-associated T_1 Map reduction. This study discusses T_1 sensitivity to cellular density [106] as a possible explanation for this effect [105].

5.4 ASL

Healthy participants exhibited numerically lower ASL values than the diseased groups (acute, chronic, control), but these differences were not statistically significant (Figure 26). Accordingly, these findings suggest that disease status did not measurably affect ASL in this study's cohort.

The absence of significant differences in ASL measurements may in part be explained by measurement errors. In particular, results can be distorted whenever a vessel is inadvertently included in the ROI, a circumstance that can easily occur and represents one of the well-recognized limitations of ASL measurements. Renal cortex perfusion is generally considered the most reliable, as cortical blood flow is high and the cortex is anatomically more distant from the collecting system and larger vessels that may cause artifacts. To minimize bias, ROIs should be manually defined on an anatomical reference image and carefully adjusted to exclude hyperintense signals on the perfusion maps, which are most likely to represent vascular structures (as described by *Nery et al.* [60]). Additionally, an automatic ROI placement with an increased number of ROIs may be needed to show significant differences more precisely.

Other studies mostly report lower cortical perfusion in renal disease—mainly CKD—than in healthy subjects [61, 107-110]. For example, *Heusch et al.* [61] showed significantly higher ASL perfusion in patients with eGFR > 30 mL/min/1.73 m than in patients with eGFR ≤ 30 mL/min/1.73 m. The PARENCHIMA [111] statement (reviewing 50+ studies) concludes that renal cortical perfusion is generally reduced in CKD compared with healthy volunteers; ASL perfusion correlates to eGFR and also declines with age and excretory function [22].

While the prevailing literature indicates reduced ASL values in kidney disease relative to healthy controls, these results are not universal. Notably, *Rapacchi et al.* [112] showed increased ASL values in patients with LN, stating that the mechanism behind this observation remains unclear and may be attributable to inflammatory activity.

5.5 T_2*

In the present study, T_2* values were noticeably and consistently significantly higher in healthy participants than in the acute, chronic, and control groups (Figure 27). This data indicates that renal disease is frequently associated with reduced T_2* (= higher R_2*, as mentioned in subchapter 3.4.3) relative to healthy controls.

These results are consistent with prior BOLD-MRI work [30, 113-115] reported in CKD, diabetic kidney disease, and lupus nephritis, supporting the view that disease-related hypoxia contributes to altered renal tissue oxygenation. Using an improved BOLD analysis, *Milani et al.* [113] showed that compared to controls, CKD was associated with significantly higher mean R_2* in the outer cortical layers, suggesting impaired cortical oxygenation. In a prospective cohort, *Pruijm et al.* [114] showed that lower cortical oxygenation predicted faster renal function decline (eGFR). *Chen et al.* [30] observed that patients with LN exhibited increased R_2* relative to controls. Notably, *Simon-Zoula et al.* [116] determined that R_2* is generally higher in medulla than in cortex, and that age was associated with higher R_2* in cortical and medullary regions, which is consistent with increased medullary hypoxia in older adults. This needs to be taken into consideration as a possible confounder.

5.6 T_2 Map

T_2-mapping did not reveal statistically significant intergroup differences in this study. However, only 27 of the 46 participants contributed analyzable T_2 maps because measurements could not be obtained in several MRI examinations (see Table XVI, as well as Table XLV in appendix). The resulting reduction in sample size and corresponding loss of statistical power, together with the known variability of renal T_2 mapping (PARENCHIMA consensus, [73]), may have obscured true group effects. Methodological refinement is therefore warranted, including optimized acquisition and processing (e.g., standardized protocols, robust motion control, and

validated commercial mapping software such as MyoMaps [117]) to improve data completeness and measurement reliability.

As previously mentioned, there are multiple studies showing that renal T_2-mapping is variable and needs further standardization [72, 73, 118]. For example, *Wolf et al.* [72] showed that T_1/T_2 measurements vary widely, reflecting both methodological differences of MRR and physiological or pathological influences, such as fluid balance and renal fibrosis. The COST Action PARENCHIMA is currently working on the increase of specificity of renal MRR.

Although renal T_2-mapping shows great variability, there are studies showing increased renal T_2 Map values in patients with renal disease when compared to healthy groups [119, 120], although those are not directly related to LN. In conclusion, evidence for native renal T_2-mapping in rheumatic diseases remains limited, highlighting the need for further standardization and validation of renal T_2-mapping techniques before broader clinical application.

5.7 Age Correlation

This study demonstrated strong evidence of a negative correlation between ASL values and age, underscoring the physiological phenomenon of age-related decline in renal perfusion. This was confirmed by the PARENCHIMA systematic review by *Odudu et al.* [22], which summarized 50+ renal ASL studies and concluded that ASL-measured renal perfusion decreases with age.

Our analysis of the other parameters in SLE revealed either no correlation with age or only isolated significant findings, suggesting that age is unlikely to represent a relevant confounder. Other studies suggest some age correlation in healthy volunteers, in particular, *Li et al.* [121] showed that mpMRI renal parameters correlate with age and sex of healthy subjects. However, evidence of age dependence was often limited across studies [122-124].

5.8 Limitations

While this study offers meaningful insights, we acknowledge below the key limitations that specify the boundaries of applicability of these findings and highlight priorities for future work.

First, the cohort size was limited. Although the number of patients studied was small, this is an inherent challenge in studying such a rare disease, and the data collected still provide clinically

meaningful insights. Nonetheless, larger cohorts could strengthen future research applying functional MR imaging to evaluate renal manifestations in SLE.

Furthermore, clearer group allocations might be useful, for example by considering lupus stages (Table I) in greater detail and placing stronger emphasis on histological findings. This approach would ensure a more accurate determination of disease status and stage and allow for improved correlation with imaging results. Surprisingly, significant differences were frequently observed between the healthy group and the control group consisting of SLE patients without LN, that is, those without known kidney impairment, which may indicate that SLE induces renal alterations at an early stage, even before they become clinically apparent as lupus nephritis.

Lastly, individual parameter analyses revealed frequent differences between the left and right kidneys as well as between cortex and medulla, as can be seen in Figure 23-28. Several factors may account for these discrepancies, all of which are in direct relation to ROI placements: artificial side differences, difficulties in the presence of disease-related changes where reliably distinguishing cortex from medulla is often more challenging. This limitation could potentially be addressed by automatic ROI placement. Furthermore, the relatively low number of ROIs may have increased the likelihood of error. In the future, more automated approaches for defining and placing ROIs, such as the twelve-layer concentric objects (TLCO) method developed by *Milani et al.* [113] which divides the renal parenchyma into 12 layers of equal thickness, might help improve reproducibility. Nonetheless, our manual assessment remains the most frequently applied approach at present.

In conclusion, further methodological optimization is essential to strengthen the reproducibility and increase the clinical significance of renal mpMRI in the assessment of rheumatic diseases, in particular lupus, thereby enabling more robust and reliable applications in both research and patient care.

6. Conclusion

This dissertation contributes to further development and application of contrast-free functional multiparametric MRI of the human kidney by evaluating its utility for classifying renal involvement in rheumatic diseases. Renal involvement is a serious, and not uncommon, complication that can lead to loss of organ function and therefore requires rapid diagnosis and treatment. At present, diagnostic confirmation largely relies on invasive renal biopsy. Therefore, we systematically assessed multiple mpMRI parameters to explore their potential as early biomarkers and non-invasive surrogates for biopsy.

Taken together, our results provide substantive evidence that renal mpMRI captures disease-related alterations in lupus, with several parameters showing significant group differences and therefore yielding valuable insights. At the same time, the magnitude of discrimination, or more precisely the parameters' sensitivity to disease, varied across metrics. While significant differences between healthy and diseased kidneys were modest for some metrics (e.g., ADC), others demonstrated larger effect sizes (e.g., T_2*), and not all parameters reached statistical significance (e.g., T_2 Map).

Where effects were absent or attenuated, or where methodological constraints may have played a role, two non-exclusive interpretations must be considered: (I) current mpMRI implementations may not yet serve as an adequate substitute for renal biopsy in lupus, and (II) cohort stratification was limited in the current study (e.g., limited consideration of lupus nephritis class/stage, disease activity vs. chronicity, or treatment status), such that residual heterogeneity possibly diluted true effects. This heterogeneity also argues against reliance on a single biomarker and favors a weighted, multiparametric approach that leverages complementary information. These considerations, alongside the study's methodological limitations, frame priorities for future work, including stage-aware group definitions, incorporation of additional covariates, and further optimization and standardization of acquisition and analysis pipelines.

7. References

1. Karadeli, E., et al., *Diffusion-weighted MR imaging of kidneys in patients with systemic lupus erythematosus: initial experience.* Rheumatol Int, 2010. **30**(9): p. 1177-81.
2. Rovin, B.H., et al., *KDIGO 2024 Clinical Practice Guideline for the management of LUPUS NEPHRITIS.* Kidney International, 2024. **105**(1): p. S1-S69.
3. Rodriguez-Ramirez, S., N. Wiegley, and J.M. Mejia-Vilet, *Kidney Biopsy in Management of Lupus Nephritis: A Case-Based Narrative Review.* Kidney Med, 2024. **6**(2): p. 100772.
4. Bakdash, K., et al., *Complications of Percutaneous Renal Biopsy.* Semin Intervent Radiol, 2019. **36**(2): p. 97-103.
5. Luciano, R.L. and G.W. Moeckel, *Update on the Native Kidney Biopsy: Core Curriculum 2019.* American Journal of Kidney Diseases, 2019. **73**(3): p. 404-415.
6. Corapi, K.M., et al., *Bleeding complications of native kidney biopsy: a systematic review and meta-analysis.* Am J Kidney Dis, 2012. **60**(1): p. 62-73.
7. Nguyen, L., et al., *Kidney biopsy; challenges with peri-procedural management.* J Nephropathol, 2025. **14**(4): p. e17222-e17222.
8. Mendichovszky, I., et al., *Technical recommendations for clinical translation of renal MRI: a consensus project of the Cooperation in Science and Technology Action PARENCHIMA.* Magma, 2020. **33**(1): p. 131-140.
9. Caroli, A., et al., *Functional magnetic resonance imaging of the kidneys: where do we stand? The perspective of the European COST Action PARENCHIMA.* Nephrol Dial Transplant, 2018. **33**(suppl_2): p. ii1-ii3.
10. Roditi, G., et al., *Renovascular imaging in the NSF Era.* Journal of Magnetic Resonance Imaging, 2009. **30**(6): p. 1323-1334.
11. Olchowy, C., et al., *The presence of the gadolinium-based contrast agent depositions in the brain and symptoms of gadolinium neurotoxicity - A systematic review.* PLOS ONE, 2017. **12**(2): p. e0171704.
12. Bane, O., et al., *Renal MRI: From Nephron to NMR Signal.* J Magn Reson Imaging, 2023. **58**(6): p. 1660-1679.
13. Francis, A., et al., *Chronic kidney disease and the global public health agenda: an international consensus.* Nature Reviews Nephrology, 2024. **20**(7): p. 473-485.
14. Jager, K.J., et al., *A single number for advocacy and communication—worldwide more than 850 million individuals have kidney diseases.* Kidney International, 2019. **96**(5): p. 1048-1050.
15. Selby, N.M., et al., *Magnetic resonance imaging biomarkers for chronic kidney disease: a position paper from the European Cooperation in Science and Technology Action PARENCHIMA.* Nephrol Dial Transplant, 2018. **33**(suppl_2): p. ii4-ii14.

16. Zhang, J.L., et al., *Functional MRI of the kidneys.* J Magn Reson Imaging, 2013. **37**(2): p. 282-93.

17. Francis, S.T., N.M. Selby, and M.W. Taal, *Magnetic Resonance Imaging to Evaluate Kidney Structure, Function, and Pathology: Moving Toward Clinical Application.* American Journal of Kidney Diseases, 2023. **82**(4): p. 491-504.

18. Waschke, J., T.M. Böckers, and F. Paulsen, *Sobotta Lehrbuch Anatomie*. 2 ed. 2019: Elsevier Health Sciences, Elsevier GmbH Deutschland.

19. Benninghoff, A. and D. Drenckhahn, *Taschenbuch Anatomie*. 2008: Elsevier München, Urban&Fischer Verlag. 624.

20. Bokonjic, S., *Figure 1: Kidney anatomy. Created in BioRender.* https://BioRender.com/9g0h5vr. 2025.

21. Bokonjic, S., *Figure 2: Renal circulation.. Created in BioRender.* https://BioRender.com/2mn6hxn. 2025.

22. Odudu, A., et al., *Arterial spin labelling MRI to measure renal perfusion: a systematic review and statement paper.* Nephrology Dialysis Transplantation, 2018. **33**(suppl_2): p. ii15-ii21.

23. Nikolic I., T.V., Lackovic V. et al., *Histologija i osnovna embriologija (Histology and basic embriology)*. 2023: Data Status, Beograd, 2023.

24. Gallardo, P.A. and C.P. Vio, *Functional Anatomy of the Kidney*. 2022, Springer International Publishing. p. 7-28.

25. CERVERA, R., et al., *Systemic Lupus Erythematosus: Clinical and Immunologic Patterns of Disease Expression in a Cohort of 1,000 Patients.* Medicine, 1993. **72**(2): p. 113-124.

26. Lam, G.K. and M. Petri, *Assessment of systemic lupus erythematosus.* Clinical and experimental rheumatology, 2005. **23**(5): p. S120.

27. Li, X., et al., *Diffusion weighted imaging and blood oxygen level-dependent MR imaging of kidneys in patients with lupus nephritis.* Journal of translational medicine, 2014. **12**: p. 295.

28. Lech, M. and H.J. Anders, *The pathogenesis of lupus nephritis.* J Am Soc Nephrol, 2013. **24**(9): p. 1357-66.

29. Karadeli, E., et al., *Diffusion-weighted MR imaging of kidneys in patients with systemic lupus erythematosus: initial experience.* Rheumatology International, 2010. **30**(9): p. 1177-1181.

30. Chen, Y.-X., et al., *Clinical study on the use of advanced magnetic resonance imaging in lupus nephritis.* BMC Medical Imaging, 2022. **22**(1): p. 210.

31. Mok, C.C., *Understanding lupus nephritis: diagnosis, management, and treatment options.* Int J Womens Health, 2012. **4**: p. 213-22.

32. Christopher-Stine, L., et al., *Renal biopsy in lupus patients with low levels of proteinuria.* J Rheumatol, 2007. **34**(2): p. 332-5.

33. Golbus, J. and W.J. McCune, *LUPUS NEPHRITIS: Classification, Prognosis, Immunopathogenesis, and Treatment.* Rheumatic Disease Clinics of North America, 1994. **20**(1): p. 213-242.

34. Jennette, J.C., et al., *2012 Revised International Chapel Hill Consensus Conference Nomenclature of Vasculitides.* Arthritis & Rheumatism, 2013. **65**(1): p. 1-11.

35. Hoffmann, K., M. Hertl, and C. Sitaru, *Molekulare Diagnostik der Kollagenosen und Vaskulitiden.* Der Hautarzt, 2016. **67**(1): p. 40-52.

36. Holl-Ulrich, K., *Vaskulitis.* Der Pathologe, 2013. **34**(6): p. 569-581.

37. Bokonjic, S., *Figure 5: Classification of vasculitides by vessel size.. Created in BioRender.* https://BioRender.com/d6pgdej. 2025.

38. Kaviani, R., et al., *Single organ hepatic artery vasculitis as an unusual cause of epigastric pain: A case report.* World J Clin Cases, 2022. **10**(26): p. 9384-9389.

39. Charles Jennette, J. and R. J. Falk, *The Pathology of Vasculitis Involving the Kidney.* American Journal of Kidney Diseases, 1994. **24**(1): p. 130-141.

40. Amoli, M.M., et al., *Interleukin 8 gene polymorphism is associated with increased risk of nephritis in cutaneous vasculitis.* The Journal of rheumatology, 2002. **29**(11): p. 2367-2370.

41. Jayne, D., *Vasculitis—when can biopsy be avoided?* Nephrology Dialysis Transplantation, 2017. **32**(9): p. 1454-1456.

42. Thurman, J.M. and N.J. Serkova, *Non-invasive imaging to monitor lupus nephritis and neuropsychiatric systemic lupus erythematosus.* F1000Res, 2015. **4**: p. 153.

43. Taylor, A.J., et al., *T1 Mapping.* JACC: Cardiovascular Imaging, 2016. **9**(1): p. 67-81.

44. Chernoff, D. and P. Stark, *Principles of magnetic resonance imaging.* UpToDate. Waltham MA: UpToDate. Retrieved February, 2010.

45. Dale, B.M., M.A. Brown, and R.C. Semelka, *MRI: Basic Principles and Applications*. 5 ed. 2015: John Wiley & Sons, 2015. 248.

46. Dössel, O., *Bildgebende Verfahren in der Medizin: von der Technik zur medizinischen Anwendung*. 2016: Berlin, Heidelberg Springer Berlin Heidelberg Imprint: Springer Vieweg 2016. 513.

47. Grover, V.P., et al., *Magnetic Resonance Imaging: Principles and Techniques: Lessons for Clinicians.* J Clin Exp Hepatol, 2015. **5**(3): p. 246-55.

48. Weishaupt, D., V.D. Köchli, and B. Marincek, *Wie funktioniert MRI?: eine Einführung in Physik und Funktionsweise der Magnetresonanzbildgebung*. 2009: Springer.

49. Bokonjic, S., *Figure 6: The Larmor equation.. Created in BioRender.* https://BioRender.com/lxkco0p. 2025.

50. Bokonjic, S., *Figure 7: Nuclear spin.. Created in BioRender.* https://BioRender.com/os5lr7x. 2025.

51. Bokonjic, S., *Figure 8: Coordinate system.. Created in BioRender.* https://BioRender.com/j5g37hf. 2025.

52. Krautstrunk, J., *Figure 9: T1 and T2 relaxation.. Created in BioRender. https://BioRender.com/yyaimno*. 2025.

53. McRobbie, D., et al., *Getting in tune: resonance and relaxation.* MRI from Picture to Proton, 2017: p. 124-143.

54. Glover, G.H., *Overview of functional magnetic resonance imaging.* Neurosurg Clin N Am, 2011. **22**(2): p. 133-9, vii.

55. Caroli, A., et al., *Diffusion-weighted magnetic resonance imaging to assess diffuse renal pathology: a systematic review and statement paper.* Nephrology Dialysis Transplantation, 2018. **33**(suppl_2): p. ii29-ii40.

56. Kooreman, E.S., et al., *ADC measurements on the Unity MR-linac - A recommendation on behalf of the Elekta Unity MR-linac consortium.* Radiother Oncol, 2020. **153**: p. 106-113.

57. al., C.R.F.e., et al., *Potential Pitfalls of Using Fractional Anisotropy, Axial Diffusivity, and Radial Diffusivity as Biomarkers of Cerebral White Matter Microstructure.* Frontiers in Neuroscience (ISSN 1662-453X), 2022. **Vol. 15 (2021)**.

58. Detre, J.A., et al., *Tissue specific perfusion imaging using arterial spin labeling.* NMR Biomed, 1994. **7**(1-2): p. 75-82.

59. Buxton, R.B., et al., *A general kinetic model for quantitative perfusion imaging with arterial spin labeling.* Magn Reson Med, 1998. **40**(3): p. 383-96.

60. Nery, F., et al., *Consensus-based technical recommendations for clinical translation of renal ASL MRI.* Magnetic Resonance Materials in Physics, Biology and Medicine, 2019. **33**: p. 1-21.

61. Heusch, P., et al., *Functional evaluation of transplanted kidneys using arterial spin labeling MRI.* Journal of Magnetic Resonance Imaging, 2014. **40**(1): p. 84-89.

62. Lanzman, R.S., et al., *Arterial Spin Labeling (ASL) Perfusionsbildgebung von Transplantatnieren bei 3T.* Rofo, 2012. **184**(S 01): p. VO403_3.

63. Nery, F., et al., *Consensus-based technical recommendations for clinical translation of renal MRI*. 2020.

64. Haase, I., et al., *PO.5.118 Functional multiparametric mri to assess renal involvement in SLE*. Vol. 9. 2022. A90.3-A91.

65. Song, R., R.B. Loeffler, and C.M. Hillenbrand, *Improved renal perfusion measurement with a dual navigator-gated Q2TIPS fair technique.* Magn Reson Med, 2010. **64**(5): p. 1352-9.

66. Kiefer, C., et al., *A feasibility study on model-based evaluation of kidney perfusion measured by means of FAIR prepared true-FISP arterial spin labeling (ASL) on a 3-T MR scanner.* Acad Radiol, 2009. **16**(1): p. 79-87.

67. Pruijm, M., et al., *Renal blood oxygenation level-dependent magnetic resonance imaging to measure renal tissue oxygenation: a statement paper and systematic review.* Nephrology Dialysis Transplantation, 2018. **33**(suppl_2): p. ii22-ii28.

68. Lota, A.S., P.D. Gatehouse, and R.H. Mohiaddin, *T2 mapping and T2* imaging in heart failure.* Heart Failure Reviews, 2017. **22**(4): p. 431-440.

69. Chavhan, G.B., et al., *Principles, techniques, and applications of T2*-based MR imaging and its special applications.* Radiographics, 2009. **29**(5): p. 1433-49.

70. Tang, M.Y., et al., *GRE T2∗-weighted MRI: principles and clinical applications.* Biomed Res Int, 2014. **2014**: p. 312142.

71. Krautstrunk, J., *Figure 12: T2 and T2* relaxation.. Created in BioRender. https://BioRender.com/8c98ivk.* 2025.

72. Wolf, M., et al., *Magnetic resonance imaging T1- and T2-mapping to assess renal structure and function: a systematic review and statement paper.* Nephrology Dialysis Transplantation, 2018. **33**(suppl_2): p. ii41-ii50.

73. Dekkers, I.A., et al., *Consensus-based technical recommendations for clinical translation of renal T1 and T2 mapping MRI.* Magnetic Resonance Materials in Physics, Biology and Medicine, 2020. **33**(1): p. 163-176.

74. Semelka, R.C., et al., *HASTE MR imaging: description of technique and preliminary results in the abdomen.* J Magn Reson Imaging, 1996. **6**(4): p. 698-9.

75. Stehling, M.K., R. Turner, and P. Mansfield, *Echo-Planar Imaging: Magnetic Resonance Imaging in a Fraction of a Second.* Science, 1991. **254**(5028): p. 43-50.

76. Martirosian, P., et al., *FAIR true-FISP perfusion imaging of the kidneys.* Magnetic Resonance in Medicine, 2004. **51**(2): p. 353-361.

77. Karger, N., et al., *Quantitation of renal perfusion using arterial spin labeling with FAIR-UFLARE.* Magnetic Resonance Imaging, 2000. **18**(6): p. 641-647.

78. Tan, Q., et al., *Deep learning enabled near-isotropic CAIPIRINHA VIBE in the nephrogenic phase improves image quality and renal lesion conspicuity.* Eur J Radiol Open, 2025. **14**: p. 100622.

79. Frahm, J., A. Haase, and D. Matthaei, *Rapid NMR imaging of dynamic processes using the FLASII technique.* Magnetic Resonance in Medicine, 1986. **3**(2): p. 321-327.

80. RT, Y.H., et al., *HITACHI'S FAST SPIN ECHO TECHNOLOGY.* 2008.

81. Pai, A., et al., *Magnetic Resonance Imaging Physics*, in *StatPearls*. 2025, StatPearls Publishing; Copyright © 2025, StatPearls Publishing LLC.: Treasure Island (FL).

82. Corporation, M., *Microsoft Excel. Retrieved from https://office.microsoft.com/excel*. 2018.

83. Stabinska, J., et al., *Probing Renal Microstructure and Function with Advanced Diffusion MRI: Concepts, Applications, Challenges, and Future Directions.* Journal of Magnetic Resonance Imaging, 2023. **60**: p. 1259-1277.

84. Jerome, N., A. Caroli, and A. Ljimani, *Renal Diffusion-Weighted Imaging (DWI) for Apparent Diffusion Coefficient (ADC), Intravoxel Incoherent Motion (IVIM), and Diffusion Tensor Imaging (DTI): Basic Concepts*. 2021. p. 187-204.

85. Notohamiprodjo, M., M.F. Reiser, and S.P. Sourbron, *Diffusion and perfusion of the kidney.* European Journal of Radiology, 2010. **76**(3): p. 337-347.

86. Li, X., et al., *Diffusion weighted imaging and blood oxygen level-dependent MR imaging of kidneys in patients with lupus nephritis.* J Transl Med, 2014. **12**: p. 295.

87. Toya, R., et al., *Correlation between estimated glomerular filtration rate (eGFR) and apparent diffusion coefficient (ADC) values of the kidneys.* Magn Reson Med Sci, 2010. **9**(2): p. 59-64.

88. Xu, Y., X. Wang, and X. Jiang, *Relationship between the renal apparent diffusion coefficient and glomerular filtration rate: preliminary experience.* J Magn Reson Imaging, 2007. **26**(3): p. 678-81.

89. Fukuda, Y., et al., *Anisotropic diffusion in kidney: Apparent diffusion coefficient measurements for clinical use.* Journal of Magnetic Resonance Imaging, 2000. **11**(2): p. 156-160.

90. Thoeny, H.C., et al., *Diffusion-weighted MR imaging of kidneys in healthy volunteers and patients with parenchymal diseases: initial experience.* Radiology, 2005. **235**(3): p. 911-7.

91. Namimoto, T., et al., *Measurement of the apparent diffusion coefficient in diffuse renal disease by diffusion-weighted echo-planar MR imaging.* J Magn Reson Imaging, 1999. **9**(6): p. 832-7.

92. Lanzman, R.S., et al., *Diffusionstensor Bildgebung (DTI) von Transplantatnieren bei 3T: erste Ergebnisse.* RöFo - Fortschritte auf dem Gebiet der Röntgenstrahlen und der bildgebenden Verfahren, 2011. **183**.

93. Razek, A.A.K.A., et al., *Diffusion tensor imaging of renal cortex in lupus nephritis.* Japanese Journal of Radiology, 2021. **39**(11): p. 1069-1076.

94. Saini, S., V. Kumar, and P. Koteshwara, *Role of Diffusion Tensor Imaging in renal parenchymal changes.* Indian J Radiol Imaging, 2018. **28**(2): p. 175-181.

95. Chen, X., et al., *In vivo evaluation of renal function using diffusion weighted imaging and diffusion tensor imaging in type 2 diabetics with normoalbuminuria versus microalbuminuria.* Front Med, 2014. **8**(4): p. 471-6.

96. Wang, W.J., et al., *3T magnetic resonance diffusion tensor imaging in chronic kidney disease.* Abdom Imaging, 2014. **39**(4): p. 770-5.

97. Ye, X.J., et al., *Using magnetic resonance diffusion tensor imaging to evaluate renal function changes in diabetic patients with early-stage chronic kidney disease.* Clinical Radiology, 2019. **74**(2): p. 116-122.

98. Serai, S.D., et al., *Diffusion tensor imaging of the kidney in healthy controls and in children and young adults with autosomal recessive polycystic kidney disease.* Abdom Radiol (NY), 2019. **44**(5): p. 1867-1872.

99. Skeoch, S., et al., *Evaluation of non-contrast MRI biomarkers in lupus nephritis.* Clin Exp Rheumatol, 2017. **35**(6): p. 954-958.

100. Seah, J.-m., et al., *Functional MRI in assessment of diabetic kidney disease in people with type 1 diabetes.* Journal of Diabetes and its Complications, 2022. **36**(1): p. 108076.

101. Shi, Z., et al., *Native T1-mapping as a predictor of progressive renal function decline in chronic kidney disease patients.* BMC Nephrol, 2024. **25**(1): p. 121.

102. Graham-Brown, M.P., et al., *Association between native T1 mapping of the kidney and renal fibrosis in patients with IgA nephropathy.* BMC Nephrol, 2019. **20**(1): p. 256.

103. Wu, J., et al., *Native T1 Mapping in Assessing Kidney Fibrosis for Patients With Chronic Glomerulonephritis.* Front Med (Lausanne), 2021. **8**: p. 772326.

104. Cox, E.F., et al., *Multiparametric Renal Magnetic Resonance Imaging: Validation, Interventions, and Alterations in Chronic Kidney Disease.* Frontiers in Physiology, 2017. **Volume 8 - 2017**.

105. Aslam, I., et al., *Validation of automatically measured T1 map cortico-medullary difference (ΔT1) for eGFR and fibrosis assessment in allograft kidneys.* PLoS One, 2023. **18**(2): p. e0277277.

106. Zormpas-Petridis, K., et al., *Noninvasive MRI Native T1 Mapping Detects Response to MYCN-targeted Therapies in the Th-MYCN Model of Neuroblastoma.* Cancer Research, 2020. **80**(16): p. 3424-3435.

107. Cai, Y.-z., et al., *Diagnostic value of renal perfusion in patients with chronic kidney disease using 3D arterial spin labeling.* Journal of Magnetic Resonance Imaging, 2017. **46**(2): p. 589-594.

108. Rossi, C., et al., *Histogram analysis of renal arterial spin labeling perfusion data reveals differences between volunteers and patients with mild chronic kidney disease.* Invest Radiol, 2012. **47**(8): p. 490-6.

109. Tan, H., I. Koktzoglou, and P.V. Prasad, *Renal perfusion imaging with two-dimensional navigator gated arterial spin labeling.* Magn Reson Med, 2014. **71**(2): p. 570-9.

110. Li, L.P., et al., *Evaluation of Renal Blood Flow in Chronic Kidney Disease Using Arterial Spin Labeling Perfusion Magnetic Resonance Imaging.* Kidney Int Rep, 2017. **2**(1): p. 36-43.

111. PARENCHIMA. *COST Action CA16103: Magnetic Resonance Imaging Biomarkers for Chronic Kidney Disease*. PARENCHIMA consensus papers (ASL, DWI, T1/T2 mapping, BOLD) to justify methods/parameters: Nery et al. 2020 (ASL), Dekkers et al. 2020 (T1/T2), Ljimani et al. 2020 (DWI), Bane et al. 2020 (BOLD).]. Available from: www.renalmri.org.

112. Rapacchi, S., et al., *Towards the identification of multi-parametric quantitative MRI biomarkers in lupus nephritis.* Magnetic Resonance Imaging, 2015. **33**(9): p. 1066-1074.

113. Milani, B., et al., *Reduction of cortical oxygenation in chronic kidney disease: evidence obtained with a new analysis method of blood oxygenation level-dependent magnetic resonance imaging.* Nephrology Dialysis Transplantation, 2016. **32**(12): p. 2097-2105.

114. Pruijm, M., et al., *Reduced cortical oxygenation predicts a progressive decline of renal function in patients with chronic kidney disease.* Kidney International, 2018. **93**(4): p. 932-940.

115. Yin, W.-J., et al., *Noninvasive evaluation of renal oxygenation in diabetic nephropathy by BOLD-MRI.* European Journal of Radiology, 2012. **81**(7): p. 1426-1431.

116. Simon-Zoula, S.C., et al., *Non-invasive monitoring of renal oxygenation using BOLD-MRI: a reproducibility study.* NMR in Biomedicine, 2006. **19**(1): p. 84-89.

117. Siemens-Healthcare-GmbH, *MyoMaps Software. Siemens Healthineers.* https://www.siemens-healthineers.com/magnetic-resonance-imaging/options-and-upgrades/clinical-applications/myomaps. 2020.

118. Li, H., et al., *Improvements in Between-Vendor MRI Harmonization of Renal T(2) Mapping using Stimulated Echo Compensation.* J Magn Reson Imaging, 2024. **60**(5): p. 2144-2155.

119. Siedek, F., et al., *Magnetic Resonance Kidney Parenchyma-T2 as a Novel Imaging Biomarker for Autosomal Dominant Polycystic Kidney Disease.* Investigative Radiology, 2020. **55**(4): p. 217-225.

120. Adams, L.C., et al., *Multiparametric Assessment of Changes in Renal Tissue after Kidney Transplantation with Quantitative MR Relaxometry and Diffusion-Tensor Imaging at 3 T.* J Clin Med, 2020. **9**(5).

121. Li, X.-M., et al., *Non-invasive evaluation of renal structure and function of healthy individuals with multiparametric MRI: Effects of sex and age.* Scientific Reports, 2019. **9**(1): p. 10661.

122. Suo, S.T., et al., *Apparent diffusion coefficient measurements of bilateral kidneys at 3 T MRI: effects of age, gender, and laterality in healthy adults.* Clin Radiol, 2014. **69**(12): p. e491-6.

123. Rabadi, T., et al., *Influence of age on parameters of multiparametric functional renal MRI: A prospective exploratory study.* Eur J Radiol, 2025. **192**: p. 112366.

124. Henry, R., et al., *MRI quantitative T1 and T2 mapping of the renal cortex: Assessment of normal values and potential usefulness for renal masses at 3 T.* European Journal of Radiology, 2024. **181**: p. 111741.

8. Table of Figures

9. Table of Tables

10. Appendix

10.1 Comparison Tests: Results

Table XXI: Post hoc tests for significant ADC RNC ANOVA, Tukey HSD and Sidak, conducted by using the SPSS software 29.0.2.0. Two post hoc tests were performed, since ANOVA detected a significant difference for this example's measured parameter ADC RNC. The column marked by "Sig." shows a significant difference for the comparison between healthy subjects and acute group, as well as between acute group and control group, with *p*-values respectively < 0.01 and < 0.05.

Multiple Comparisons							
Dependent Variable: ADC_RNC							
						95% Confidence Interval	
	(I) Group	(J) Group	Mean Difference (I-J)	Std. Error	Sig.	Lower Bound	Upper Bound
Tukey HSD	Healthy	Acute	247.500*	62.312	.002	80.82	414.18
		Chronic	125.643	73.005	.326	-69.64	320.93
		Control	77.938	59.718	.565	-81.81	237.68
	Acute	Healthy	-247.500*	62.312	.002	-414.18	-80.82
		Chronic	-121.857	69.450	.309	-307.63	63.92
		Control	-169.563*	55.316	.019	-317.53	-21.60
	Chronic	Healthy	-125.643	73.005	.326	-320.93	69.64
		Acute	121.857	69.450	.309	-63.92	307.63
		Control	-47.705	67.133	.892	-227.28	131.87
	Control	Healthy	-77.938	59.718	.565	-237.68	81.81
		Acute	169.563*	55.316	.019	21.60	317.53
		Chronic	47.705	67.133	.892	-131.87	227.28
Sidak	Healthy	Acute	247.500*	62.312	.002	75.47	419.53
		Chronic	125.643	73.005	.442	-75.91	327.20
		Control	77.938	59.718	.736	-86.93	242.81
	Acute	Healthy	-247.500*	62.312	.002	-419.53	-75.47
		Chronic	-121.857	69.450	.419	-313.59	69.88
		Control	-169.563*	55.316	.023	-322.28	-16.85
	Chronic	Healthy	-125.643	73.005	.442	-327.20	75.91
		Acute	121.857	69.450	.419	-69.88	313.59
		Control	-47.705	67.133	.981	-233.04	137.63
	Control	Healthy	-77.938	59.718	.736	-242.81	86.93
		Acute	169.563*	55.316	.023	16.85	322.28
		Chronic	47.705	67.133	.981	-137.63	233.04

*. The mean difference is significant at the 0.05 level.

Table XXII: Post hoc test, Mann-Whitney, conducted by using the SPSS software 29.0.2.0. This test was performed for further specifying which groups were exactly significantly different, by applying it pairwise for each group, so that they were all compared to each other. This table shows a comparison between healthy subjects and patients with acute changes of the kidney. The parameter measured was FA of the left kidney's medulla (FA LNM). The post hoc Mann-Whitney test showed no significant difference with $p = 0.067$, as can be seen as the exact significance in the last row of the right table.

Ranks				
	Group	N	Mean Rank	Sum of Ranks
FA_LNM	Healthy subjects	10	9.00	90.00
	Acute	13	14.31	186.00
	Total	23		

Test Statistics[a]	
	FA_LNM
Mann-Whitney U	35.000
Wilcoxon W	90.000
Z	-1.861
Asymp. Sig. (2-tailed)	.063
Exact Sig. (2*(1-tailed Sig.))	.067[b]

a. Grouping Variable: Group
b. Not corrected for ties.

Table XXIII: Post hoc test, Mann-Whitney, conducted by using the SPSS software 29.0.2.0. This test was performed for further specifying which groups were exactly significantly different, by applying it pairwise for each group, so that they were all compared to each other. This table shows a comparison between healthy subjects and patients with chronic changes of the kidney. The parameter measured was FA of the left kidney's medulla (FA LNM). The post hoc Mann-Whitney test showed a significant difference with $p < 0.01$, expressed as the exact significance in the last row of the right table.

Ranks				
	Group	N	Mean Rank	Sum of Ranks
FA_LNM	Healthy subjects	10	5.60	56.00
	Chronic	7	13.86	97.00
	Total	17		

Test Statistics[a]	
	FA_LNM
Mann-Whitney U	1.000
Wilcoxon W	56.000
Z	-3.318
Asymp. Sig. (2-tailed)	<.001
Exact Sig. (2*(1-tailed Sig.))	<.001[b]

a. Grouping Variable: Group
b. Not corrected for ties.

10.2 Results Tables from the Pearson and Spearman Correlation

Table XXIV: Pearson correlation analysis for parameter ADC in the right and left renal cortex and medulla, conducted by using the SPSS software 29.0.2.0. Both the positively and negatively correlating values are marked with * - and ** - symbol. This analysis shows only positively correlating values.

Parametric Correlations						
		Years	ADC_RNC	ADC_RNM	ADC_LNC	ADC_LNM
Years	Pearson Correlation	1	.307*	-.154	.172	-.002
	Sig. (2-tailed)		.038	.306	.254	.987
	N	46	46	46	46	46
ADC_RNC	Pearson Correlation	.307*	1	.424**	.622**	.307*
	Sig. (2-tailed)	.038		.003	<.001	.038
	N	46	46	46	46	46

ADC_RNM	Pearson Correlation	-.154	.424**	1	.351*	.574**
	Sig. (2-tailed)	.306	.003		.017	<.001
	N	46	46	46	46	46
ADC_LNC	Pearson Correlation	.172	.622**	.351*	1	.546**
	Sig. (2-tailed)	.254	<.001	.017		<.001
	N	46	46	46	46	46
ADC_LNM	Pearson Correlation	-.002	.307*	.574**	.546**	1
	Sig. (2-tailed)	.987	.038	<.001	<.001	
	N	46	46	46	46	46

*. Correlation is significant at the 0.05 level (2-tailed).

**. Correlation is significant at the 0.01 level (2-tailed).

Table XXV: Pearson correlation analysis for parameter FA in the right and left renal cortex and right renal medulla, conducted by using the SPSS software 29.0.2.0. Both the positively and negatively correlating values are marked with * - and ** - symbol. This analysis shows one positively correlating value (parameter FA RNM in comparison to FA RNC).

Parametric Correlations					
		Years	FA_RNC	FA_RNM	FA_LNC
Years	Pearson Correlation	1	.130	-.124	.124
	Sig. (2-tailed)		.391	.413	.411
	N	46	46	46	46
FA_RNC	Pearson Correlation	.130	1	.307*	.210
	Sig. (2-tailed)	.391		.038	.161
	N	46	46	46	46
FA_RNM	Pearson Correlation	-.124	.307*	1	.088
	Sig. (2-tailed)	.413	.038		.561
	N	46	46	46	46
FA_LNC	Pearson Correlation	.124	.210	.088	1
	Sig. (2-tailed)	.411	.161	.561	
	N	46	46	46	46

*. Correlation is significant at the 0.05 level (2-tailed).

Table XXVI: Pearson correlation analysis for parameter T_1 Map in left renal medulla, conducted by using the SPSS software 29.0.2.0. Both the positively and negatively correlating values are marked with * - and ** - symbol. This analysis shows no correlating values.

Parametric Correlations			
		Years	T_1_Map_LNM
Years	Pearson Correlation	1	.275
	Sig. (2-tailed)		.065
	N	46	46
T_1_Map_LNM	Pearson Correlation	.275	1
	Sig. (2-tailed)	.065	
	N	46	46

Table XXVII: Pearson correlation analysis for parameter ASL in the right and left renal cortex and right renal medulla, conducted by using the SPSS software 29.0.2.0. Both the positively and negatively correlating values are marked with * - and ** - symbol.

Parametric Correlations					
		Years	ASL_RNC	ASL_RNM	ASL_LNC
Years	Pearson Correlation	1	-.382**	-.367*	-.465**
	Sig. (2-tailed)		.009	.012	.001
	N	46	46	46	46
ASL_RNC	Pearson Correlation	-.382**	1	.618**	.725**
	Sig. (2-tailed)	.009		<.001	<.001
	N	46	46	46	46
ASL_RNM	Pearson Correlation	-.367*	.618**	1	.573**
	Sig. (2-tailed)	.012	<.001		<.001
	N	46	46	46	46
ASL_LNC	Pearson Correlation	-.465**	.725**	.573**	1
	Sig. (2-tailed)	.001	<.001	<.001	
	N	46	46	46	46

**. Correlation is significant at the 0.01 level (2-tailed).

*. Correlation is significant at the 0.05 level (2-tailed).

Table XXVIII: Pearson correlation analysis for parameter T_2 Map in the right and left renal cortex and medulla, conducted by using the SPSS software 29.0.2.0. Both the positively and negatively correlating values are marked with * - and ** - symbol. This analysis shows only positively correlating values.

Parametric Correlations						
		Years	T_2_Map_RNC	T_2_Map_RNM	T_2_Map_LNC	T_2_Map_LNM
Years	Pearson Correlation	1	.250	.230	-.102	.156
	Sig. (2-tailed)		.209	.248	.613	.438
	N	46	27	27	27	27
T_2_Map _RNC	Pearson Correlation	.250	1	.176	.387*	.261
	Sig. (2-tailed)	.209		.381	.046	.189
	N	27	27	27	27	27
T_2_Map _RNM	Pearson Correlation	.230	.176	1	-.233	.160
	Sig. (2-tailed)	.248	.381		.243	.426
	N	27	27	27	27	27
T_2_Map _LNC	Pearson Correlation	-.102	.387*	-.233	1	.461*
	Sig. (2-tailed)	.613	.046	.243		.015
	N	27	27	27	27	27
T_2_Map _LNM	Pearson Correlation	.156	.261	.160	.461*	1
	Sig. (2-tailed)	.438	.189	.426	.015	
	N	27	27	27	27	27

*. Correlation is significant at the 0.05 level (2-tailed).

Table XXIX: Spearman correlation analysis for parameter FA in the left renal medulla, conducted by using the SPSS software 29.0.2.0. The correlating values are marked with * - and **- symbol. This analysis shows no correlating values.

Nonparametric Correlations				
			Years	FA_LNM
Spearman´s rho	Years	Correlation Coefficient	1.000	-.039
		Sig. (2-tailed)	.	.796
		N	46	46
	FA_LNM	Correlation Coefficient	-.039	1.000
		Sig. (2-tailed)	.796	.
		N	46	46

Table XXX: Spearman correlation analysis for parameter T_1 Map in the right and left renal cortex and right renal medulla, conducted by using the SPSS software 29.0.2.0. The correlating values are marked with * - and **- symbol. This analysis shows only positively correlating values.

Nonparametric Correlations						
			Years	T_1_Map_RNC	T_1_Map_RNM	T_1_Map_LNC
Spearman´s rho	Years	Correlation Coefficient	1.000	-.054	.378**	-.066
		Sig. (2-tailed)	.	.721	.010	.661
		N	46	46	46	46
	T_1_Map_RNC	Correlation Coefficient	-.054	1.000	.263	.332*
		Sig. (2-tailed)	.721	.	.077	.024
		N	46	46	46	46
	T_1_Map_RNM	Correlation Coefficient	.378**	.263	1.000	.301*
		Sig. (2-tailed)	.010	.077	.	.042
		N	46	46	46	46
	T_1_Map_LNC	Correlation Coefficient	-.066	.332*	.301*	1.000
		Sig. (2-tailed)	.661	.024	.042	.
		N	46	46	46	46

**. Correlation is significant at the 0.01 level (2-tailed).

*. Correlation is significant at the 0.05 level (2-tailed).

Table XXXI: Spearman correlation analysis for parameter ASL in left renal medulla, conducted by using the SPSS software 29.0.2.0. The correlating values are marked with * - and **- symbol. This analysis shows no correlating values.

Nonparametric Correlations				
			Years	ASL_LNM
Spearman´s rho	Years	Correlation Coefficient	1.000	-.224
		Sig. (2-tailed)	.	.134
		N	46	46
	ASL_LNM	Correlation Coefficient	-.224	1.000
		Sig. (2-tailed)	.134	.
		N	46	46

Table XXXII: Spearman correlation analysis for parameter T_2* in the right and left renal cortex and medulla, conducted by using the SPSS software 29.0.2.0. The correlating values are marked with * - and **- symbol. This analysis shows only positively correlating values.

Nonparametric Correlations							
			Years	T_2_RNC	T_2_RNM	T_2_LNC	T_2_LNM
Spearman´s rho	Years	Correlation Coefficient	1.000	.217	.064	.344*	.154
		Sig. (2-tailed)	.	.148	.674	.019	.308
		N	46	46	46	46	46
	T_2_RNC	Correlation Coefficient	.217	1.000	.741**	.709**	.693**
		Sig. (2-tailed)	.148	.	<.001	<.001	<.001
		N	46	46	46	46	46
	T_2_RNN	Correlation Coefficient	.064	.741**	1.000	.587**	.760**
		Sig. (2-tailed)	.674	<.001	.	<.001	<.001
		N	46	46	46	46	46
	T_2_LNC	Correlation Coefficient	.344*	.709**	.587**	1.000	.727**
		Sig. (2-tailed)	.019	<.001	<.001	.	<.001
		N	46	46	46	46	46
	T_2_LNM	Correlation Coefficient	.154	.693**	.760**	.727**	1.000
		Sig. (2-tailed)	.308	<.001	<.001	<.001	.
		N	46	46	46	46	46

*. Correlation is significant at the 0.05 level (2-tailed).

**. Correlation is significant at the 0.01 level (2-tailed).

Table XXXIII: Pearson correlation analysis, linear correlation between two variables – years (participant´s age) vs. FA in right and left renal cortex and right renal medulla. Significant values are marked by the asterisk (*) and the *p*-values are listed in the “Sig.” - column. There were no significant correlations for the measured parameters. Analysis conducted by using the SPSS software 29.0.2.0

		FA_RNC	FA_RNM	FA_LNC
Years	Pearson Correlation	.130	-.124	.124
	Sig. (2-tailed)	.391	.413	.411

*. Correlation is significant at the 0.05 level (2-tailed)

**. Correlation is significant at the 0.01 level (2-tailed)

Table XXXIV: Pearson correlation analysis, linear correlation between two variables – years (participant´s age) vs. T_1 Map in the left renal medulla. Significant values are marked by the asterisk (*) and the *p*-values are listed in the "Sig." - column. There were no significant correlations for the measured parameter. Analysis conducted by using the SPSS software 29.0.2.0

		T_1 Map_LNM
Years	Pearson Correlation	-.275
	Sig. (2-tailed)	.065

*. Correlation is significant at the 0.05 level (2-tailed)

**. Correlation is significant at the 0.01 level (2-tailed)

Table XXXV: Pearson correlation analysis, linear correlation between two variables – years (participant´s age) vs. T_2 Map in right and left renal cortex and medulla. There were no significant correlations for the measured parameters. Analysis conducted by using the SPSS software 29.0.2.0

		T_2 Map_RNC	T_2 Map _RNM	T_2 Map _LNC	T_2 Map _LNM
Years	Pearson Correlation	.250	.230	-.102	.156
	Sig. (2-tailed)	.209	.248	.613	.438

*. Correlation is significant at the 0.05 level (2-tailed)

**. Correlation is significant at the 0.01 level (2-tailed)

Table XXXVI: Spearman correlation analysis, correlation between two ranked variables – years (participant´s age) vs. FA in left renal medulla. There were no significant correlations for the measured parameters. Analysis conducted by using the SPSS software 29.0.2.0

		FA_LNM
Years	Spearman's rho Correlation Coefficient	-.039
	Sig. (2-tailed)	.796

*. Correlation is significant at the 0.05 level (2-tailed)

**. Correlation is significant at the 0.01 level (2-tailed)

Table XXXVII: Spearman correlation analysis, correlation between two ranked variables – years (participant´s age) vs. ASL in left renal medulla. There were no significant correlations for the measured parameters. Analysis conducted by using the SPSS software 29.0.2.0

		ASL_LNM
Years	Spearman's rho Correlation Coefficient	-.224
	Sig. (2-tailed)	.134

*. Correlation is significant at the 0.05 level (2-tailed)

**. Correlation is significant at the 0.01 level (2-tailed)

10.3 Tables with Participants Data

Table XXXVIII: Data of 36 patients included in this study, with their respectable codes, age, sex, date of MRI acquisition and groups.

	Code	Age in years	Sex	MRI date	Group
1	LN01a	24	F	20.05.2020	acute
2	LN02	70	M	29.07.2020	acute
3	LN03	45	M	20.08.2020	acute
4	LN04	42	F	27.08.2020	acute
5	LN05	56	F	05.09.2020	acute
6	LN08	71	M	09.12.2020	control
7	LN09	41	F	18.12.2020	control
8	LN11	56	F	04.01.2021	control
9	LN12	42	F	12.01.2021	chronic
10	LN14	57	M	20.01.2021	chronic
11	LN17	34	M	10.02.2021	control
12	LN18	57	M	10.02.2021	control
13	LN20	24	F	15.02.2021	chronic
14	LN21	35	F	17.02.2021	chronic
15	LN22	57	F	24.02.2021	control
16	LN24	61	F	03.03.2021	control
17	LN25	47	M	03.03.2021	control
18	LN26	68	F	12.05.2021	control
19	LN27a	36	M	12.05.2021	acute
20	LN28	44	F	19.05.2021	chronic
21	LN29	51	F	19.05.2021	chronic
22	LN30	71	F	26.05.2021	control
23	LN31	48	F	23.06.2021	control
24	LN32	42	F	21.07.2021	control

25	LN34	60	F	27.07.2021	control
26	LN35	66	F	29.07.2021	control
27	LN37	36	F	15.09.2021	control
28	LN40	42	F	08.12.2021	acute
29	LN42	38	M	06.02.2022	chronic
30	LN43	42	M	16.03.2022	acute
31	LN44	35	F	05.04.2022	acute
32	LN45	34	F	31.05.2022	control
33	LN46	45	M	02.06.2022	acute
34	LN47	23	F	20.07.2022	acute
35	LN50	60	F	08.12.2022	acute
36	LN51	44	F	05.04.2023	acute

Table XXXIX: Data of 10 healthy participants included in this study, with their respectable codes, age, sex and groups.

	Code	Age in years	Sex	Group
1	Proband01	63	M	healthy
2	Proband02	65	F	healthy
3	Proband03	67	M	healthy
4	Proband04	54	M	healthy
5	Proband05	58	F	healthy
6	Proband06	76	M	healthy
7	Proband07	67	F	healthy
8	Proband08	62	F	healthy
9	Proband09	67	F	healthy
10	Proband10	53	F	healthy

Table XL: ADC data for each participant included in this study, with their respectable codes and groups.

	Code	ADC RNC	ADC RNM	ADC LNC	ADC LNM	Group
1	LN01a	1986	2174	2131	2550	acute
2	LN02	1752	1493	1725	1434	acute
3	LN03	1347	846	1553	1092	acute
4	LN04	1579	1943	1802	1796	acute
5	LN05	1965	1931	2192	2144	acute
6	LN08	1844	1355	2019	2008	control
7	LN09	2184	2019	2176	2158	control
8	LN11	1743	1916	1864	1868	control
9	LN12	1983	1988	1953	1521	chronic
10	LN14	1996	1352	1952	1315	chronic
11	LN17	1863	1731	1912	1407	control
12	LN18	1867	1447	2010	2026	control
13	LN20	1818	1765	1832	1552	chronic
14	LN21	1763	1608	1766	1581	chronic
15	LN22	1954	1978	1603	1613	control
16	LN24	1927	1856	1913	2041	control
17	LN25	1766	1539	1824	1523	control

18	LN26	2069	1412	1982	1980	control
19	LN27a	1688	1830	1958	2078	acute
20	LN28	1891	2033	2067	1499	chronic
21	LN29	1991	1783	1999	1833	chronic
22	LN30	2076	1916	1790	1698	control
23	LN31	2000	1442	1922	1786	control
24	LN32	1761	1645	1774	1610	control
25	LN34	1902	1301	1840	1389	control
26	LN35	1746	1636	1772	1474	control
27	LN37	2146	2222	1952	1674	control
28	LN40	1827	1794	2003	1888	acute
29	LN42	1591	1888	1931	2252	chronic
30	LN43	1709	1727	1798	1545	acute
31	LN44	1863	1814	1875	1964	acute
32	LN45	1705	1791	1487	1665	control
33	LN46	1659	1995	1747	2070	acute
34	LN47	1716	2037	1668	2072	acute
35	LN50	1828	2098	2036	1917	acute
36	LN51	1701	1832	1738	1940	acute
37	Proband01	2049	2031	1888	1918	healthy
38	Proband02	1874	1818	1906	1881	healthy
39	Proband03	2041	2032	2002	2003	healthy
40	Proband04	1927	1955	2026	2040	healthy
41	Proband05	1966	1996	1966	1987	healthy
42	Proband06	1796	1748	1862	1796	healthy
43	Proband07	2008	1932	2034	2032	healthy
44	Proband08	2204	2149	2068	2122	healthy
45	Proband09	1976	1960	2005	2030	healthy
46	Proband10	2034	2132	1986	2081	healthy

Table XLI: FA data for each participant included in this study, with their respectable codes and groups.

	Code	FA RNC	FA RNM	FA LNC	FA LNM	Group
1	LN01a	193	255	212	199	acute
2	LN02	187	324	285	463	acute
3	LN03	352	448	324	599	acute
4	LN04	283	314	184	307	acute
5	LN05	166	213	481	445	acute
6	LN08	372	400	183	287	control
7	LN09	112	302	122	289	control
8	LN11	229	211	308	297	control
9	LN12	231	197	118	261	chronic
10	LN14	186	477	245	431	chronic
11	LN17	214	258	159	318	control
12	LN18	193	236	134	304	control
13	LN20	234	337	272	474	chronic
14	LN21	125	286	164	302	chronic
15	LN22	249	211	210	514	control
16	LN24	123	262	236	540	control
17	LN25	273	352	288	424	control
18	LN26	193	284	143	239	control
19	LN27a	239	351	267	225	acute
20	LN28	94	350	214	263	chronic

21	LN29	285	243	306	226	chronic
22	LN30	217	244	205	410	control
23	LN31	175	471	146	407	control
24	LN32	159	177	184	284	control
25	LN34	166	340	214	353	control
26	LN35	311	390	152	541	control
27	LN37	166	270	118	359	control
28	LN40	231	282	273	297	acute
29	LN42	199	231	212	297	chronic
30	LN43	242	459	155	474	acute
31	LN44	175	235	149	267	acute
32	LN45	262	468	247	175	control
33	LN46	114	254	129	159	acute
34	LN47	217	166	128	178	acute
35	LN50	185	269	212	153	acute
36	LN51	246	303	219	339	acute
37	Proband01	208	193	217	234	healthy
38	Proband02	200	215	189	159	healthy
39	Proband03	219	237	226	210	healthy
40	Proband04	248	232	198	218	healthy
41	Proband05	148	153	203	189	healthy
42	Proband06	172	165	187	176	healthy
43	Proband07	236	216	212	212	healthy
44	Proband08	352	287	217	211	healthy
45	Proband09	246	258	234	223	healthy
46	Proband10	181	174	179	192	healthy

Table XLII: T_1 Map data for each participant included in this study, with their respectable codes and groups.

	Code	T_1 Map RNC	T_1 Map RNM	T_1 Map LNC	T_1 Map LNM	Group
1	LN01a	309	100	456	315	acute
2	LN02	337	657	525	628	acute
3	LN03	466	333	363	343	acute
4	LN04	364	498	667	794	acute
5	LN05	509	848	1521	442	acute
6	LN08	645	577	574	646	control
7	LN09	1244	400	1116	384	control
8	LN11	1458	540	1143	999	control
9	LN12	1304	483	1135	761	chronic
10	LN14	1159	360	1136	586	chronic
11	LN17	547	1000	1152	842	control
12	LN18	436	380	516	653	control
13	LN20	1537	527	1087	382	chronic
14	LN21	1160	932	1259	763	chronic
15	LN22	1439	500	813	395	control
16	LN24	983	423	1199	519	control
17	LN25	805	161	763	365	control
18	LN26	717	740	1178	859	control
19	LN27a	1178	293	488	402	acute
20	LN28	1393	965	1142	560	chronic
21	LN29	1077	453	367	536	chronic
22	LN30	532	727	823	229	control

23	LN31	146	428	1242	606	control
24	LN32	1010	355	911	434	control
25	LN34	1398	751	954	590	control
26	LN35	427	328	876	666	control
27	LN37	274	329	542	198	control
28	LN40	1325	138	1513	1153	acute
29	LN42	1023	718	522	764	chronic
30	LN43	906	988	1208	477	acute
31	LN44	1138	376	1377	505	acute
32	LN45	758	524	959	674	control
33	LN46	1021	996	533	755	acute
34	LN47	1317	902	1530	1323	acute
35	LN50	634	536	247	760	acute
36	LN51	516	1088	770	868	acute
37	Proband01	1345	1289	713	965	healthy
38	Proband02	1162	1323	1185	1265	healthy
39	Proband03	1098	1204	1179	1291	healthy
40	Proband04	1057	1345	1059	1021	healthy
41	Proband05	1084	1116	1185	1318	healthy
42	Proband06	1087	1303	1078	1086	healthy
43	Proband07	1240	1176	911	933	healthy
44	Proband08	1214	1272	937	1090	healthy
45	Proband09	1087	1269	1234	1015	healthy
46	Proband10	1149	1416	1188	1330	healthy

Table XLIII: ASL data for each participant included in this study, with their respectable codes and groups.

	Code	ASL RNC	ASL RNM	ASL LNC	ASL LNM	Group
1	LN01a	508	673	433	621	acute
2	LN02	187	107	175	239	acute
3	LN03	82	58	113	80	acute
4	LN04	399	252	375	352	acute
5	LN05	280	409	344	367	acute
6	LN08	173	366	329	403	control
7	LN09	262	202	395	495	control
8	LN11	301	337	342	568	control
9	LN12	300	381	329	254	chronic
10	LN14	326	366	332	268	chronic
11	LN17	427	455	390	261	control
12	LN18	223	446	209	267	control
13	LN20	376	459	555	354	chronic
14	LN21	232	360	355	440	chronic
15	LN22	338	370	280	445	control
16	LN24	350	418	353	303	control
17	LN25	328	609	338	558	control
18	LN26	264	419	235	426	control
19	LN27a	405	529	368	456	acute
20	LN28	402	280	426	266	chronic
21	LN29	386	208	233	296	chronic
22	LN30	327	217	236	564	control
23	LN31	286	671	269	412	control
24	LN32	394	362	412	432	control
25	LN34	425	516	355	259	control

26	LN35	364	422	268	404	control
27	LN37	354	490	370	598	control
28	LN40	348	297	474	534	acute
29	LN42	236	213	143	274	chronic
30	LN43	339	661	468	914	acute
31	LN44	341	471	274	560	acute
32	LN45	289	200	280	213	control
33	LN46	258	393	222	446	acute
34	LN47	595	868	524	803	acute
35	LN50	324	478	366	471	acute
36	LN51	145	350	167	237	acute
37	Proband01	276	316	263	287	healthy
38	Proband02	279	297	294	339	healthy
39	Proband03	291	293	297	305	healthy
40	Proband04	269	278	254	261	healthy
41	Proband05	341	312	252	313	healthy
42	Proband06	205	223	186	189	healthy
43	Proband07	302	277	270	268	healthy
44	Proband08	314	328	290	279	healthy
45	Proband09	438	503	428	521	healthy
46	Proband10	241	277	220	268	healthy

Table XLIV: T_2* data for each participant included in this study, with their respectable codes and groups.

	Code	T_2* RNC	T_2* RNM	T_2* LNC	T_2* LNM	Group
1	LN01a	56	42	46	41	acute
2	LN02	53	39	50	37	acute
3	LN03	43	35	41	31	acute
4	LN04	63	53	60	48	acute
5	LN05	55	29	57	44	acute
6	LN08	52	24	46	38	control
7	LN09	54	43	63	48	control
8	LN11	44	47	58	62	control
9	LN12	55	58	51	61	chronic
10	LN14	46	22	49	22	chronic
11	LN17	53	42	57	38	control
12	LN18	66	32	61	48	control
13	LN20	51	37	50	43	chronic
14	LN21	55	41	57	36	chronic
15	LN22	52	30	55	24	control
16	LN24	72	36	54	40	control
17	LN25	55	46	51	39	control
18	LN26	57	34	55	48	control
19	LN27a	64	55	40	30	acute
20	LN28	66	37	53	29	chronic
21	LN29	51	23	65	50	chronic
22	LN30	49	36	60	30	control
23	LN31	64	28	51	42	control
24	LN32	63	40	53	58	control
25	LN34	49	39	37	20	control
26	LN35	53	26	56	18	control
27	LN37	63	58	50	45	control
28	LN40	71	45	50	48	acute

29	LN42	36	24	33	25	chronic
30	LN43	41	23	39	38	acute
31	LN44	65	53	67	58	acute
32	LN45	52	34	51	45	control
33	LN46	46	55	30	56	acute
34	LN47	67	85	58	83	acute
35	LN50	53	33	52	31	acute
36	LN51	95	47	67	48	acute
37	Proband01	131	129	130	130	healthy
38	Proband02	115	113	126	123	healthy
39	Proband03	164	170	176	168	healthy
40	Proband04	126	122	140	135	healthy
41	Proband05	178	174	134	146	healthy
42	Proband06	147	133	130	130	healthy
43	Proband07	176	178	158	155	healthy
44	Proband08	109	105	128	122	healthy
45	Proband09	171	169	191	195	healthy
46	Proband10	131	138	137	141	healthy

Table XLV: T_2 Map data for each participant included in this study, with their respectable codes and groups.

	Code	T_2 Map RNC	T_2 Map RNM	T_2 Map LNC	T_2 Map LNM	Group
1	LN01a	134	184	176	207	acute
2	LN02	119	344	94	148	acute
3	LN04	144	178	186	158	acute
4	LN05	191	204	263	203	acute
5	LN08	150	226	157	225	control
6	LN09	136	159	169	124	control
7	LN11	158	151	143	151	control
8	LN12	155	148	189	158	chronic
9	LN14	134	177	146	176	chronic
10	LN17	135	147	156	137	control
11	LN18	194	222	184	157	control
12	LN20	133	150	131	133	chronic
13	LN21	151	210	158	210	chronic
14	LN22	159	201	199	168	control
15	LN24	145	136	192	258	control
16	LN25	138	116	155	127	control
17	LN27a	124	141	246	183	acute
18	Proband01	126	127	173	163	healthy
19	Proband02	178	170	185	196	healthy
20	Proband03	129	133	146	137	healthy
21	Proband04	170	155	169	161	healthy
22	Proband05	143	142	156	147	healthy
23	Proband06	140	156	174	167	healthy
24	Proband07	204	171	173	169	healthy
25	Proband08	209	217	170	180	healthy
26	Proband09	140	156	172	182	healthy
27	Proband10	179	179	230	222	healthy

10.4 Tables with t-Tests

Table XLVI: t-tests for parameter ADC between the four groups: acute, chronic, healthy and control. *p*-values can be found in the third column. Significant results ($p < 0.05$) are highlighted in bold.

ADC	t-test acute vs chronic RNC	0.12498385
	t-test acute vs chronic RNM	0.79030437
	t-test acute vs chronic LNC	0.32909521
	t-test acute vs chronic LNM	0.14964756
	t-test acute vs control RNC	**0.00790698**
	t-test acute vs control RNM	0.3461172
	t-test acute vs control LNC	0.98241473
	t-test acute vs control LNM	0.22981074
	t-test chronic vs control RNC	0.49271673
	t-test chronic vs control RNM	0.54170859
	t-test chronic vs control LNC	0.35800108
	t-test chronic vs control LNM	0.43647214
	t-test acute vs healthy RNC	**0.000583188**
	t-test acute vs healthy RNM	0.154868513
	t-test acute vs healthy LNC	0.09313506
	t-test acute vs healthy LNM	0.384958528
	t-test chronic vs healthy RNC	0.064629839
	t-test chronic vs healthy RNM	**0.035913051**
	t-test chronic vs healthy LNC	0.279704957
	t-test chronic vs healthy LNM	**0.004805316**

*Significant results ($p < 0.05$) in bold

Table XLVII: t-tests for parameter FA between the four groups: acute, chronic, healthy and control. *p*-values can be found in the third column. Significant results ($p < 0.05$) are highlighted in bold.

FA	t-test acute vs chronic RNC	0.41205028
	t-test acute vs chronic RNM	0.90350603
	t-test acute vs chronic LNC	0.1347847
	t-test acute vs chronic LNM	0.90731296
	t-test acute vs control RNC	0.85919496
	t-test acute vs control RNM	0.83646052
	t-test acute vs control LNC	0.16362263
	t-test acute vs control LNM	0.35812683

	t-test chronic vs control RNC	0.52335072
	t-test chronic vs control RNM	0.96675414
	t-test chronic vs control LNC	0.30728881
	t-test chronic vs control LNM	0.44035055
	t-test acute vs healthy RNC	0.893617774
	t-test acute vs healthy RNM	**0.008625479**
	t-test acute vs healthy LNC	0.416958116
	t-test acute vs healthy LNM	**0.02063768**
	t-test chronic vs healthy RNC	0.369415945
	t-test chronic vs healthy RNM	**0.017557323**
	t-test chronic vs healthy LNC	0.560319996
	t-test chronic vs healthy LNM	**0.001328047**

*Significant results ($p < 0.05$) in bold

Table XLVIII: t-tests for parameter T_1 Map between the four groups: acute, chronic, healthy and control. *p*-values can be found in the third column. Significant results ($p < 0.05$) are highlighted in bold.

T_1 Map	t-test acute vs chronic RNC	0.00807738
	t-test acute vs chronic RNM	0.77794654
	t-test acute vs chronic LNC	0.64868924
	t-test acute vs chronic LNM	0.6796185
	t-test acute vs control RNC	0.84188882
	t-test acute vs control RNM	0.40993803
	t-test acute vs control LNC	0.66392787
	t-test acute vs control LNM	0.28638224
	t-test chronic vs control RNC	**0.01603167**
	t-test chronic vs control RNM	0.2257403
	t-test chronic vs control LNC	0.83071792
	t-test chronic vs control LNM	0.55767864
	t-test acute vs healthy RNC	**0.006264144**
	t-test acute vs healthy RNM	4.94805E-06
	t-test acute vs healthy LNC	0.220173689
	t-test acute vs healthy LNM	**0.000347012**
	t-test chronic vs healthy RNC	0.229099121
	t-test chronic vs healthy RNM	1.23451E-06
	t-test chronic vs healthy LNC	0.369928769
	t-test chronic vs healthy LNM	5.66039E-06

*Significant results ($p < 0.05$) in bold

Table XLIX: t-tests for parameter ASL between the four groups: acute, chronic, healthy and control. *p*-values can be found in the third column. Significant results ($p < 0.05$) are highlighted in bold.

ASL	t-test acute vs chronic RNC	0.97740214
	t-test acute vs chronic RNM	0.17245062
	t-test acute vs chronic LNC	0.89794015
	t-test acute vs chronic LNM	**0.03287785**
	t-test acute vs control RNC	0.90399083
	t-test acute vs control RNM	0.76571016
	t-test acute vs control LNC	0.69447609
	t-test acute vs control LNM	0.41884174
	t-test chronic vs control RNC	0.9124893
	t-test chronic vs control RNM	0.15362157
	t-test chronic vs control LNC	0.57688443
	t-test chronic vs control LNM	**0.0477711**
	t-test acute vs healthy RNC	0.560060735
	t-test acute vs healthy RNM	0.136594288
	t-test acute vs healthy LNC	0.231818277
	t-test acute vs healthy LNM	**0.043181381**
	t-test chronic vs healthy RNC	0.417733259
	t-test chronic vs healthy RNM	0.746130103
	t-test chronic vs healthy LNC	0.202791986
	t-test chronic vs healthy LNM	0.910584554

*Significant results ($p < 0.05$) in bold

Table L: t-tests for parameter T_2* between the four groups: acute, chronic, healthy and control. *p*-values can be found in the third column. Significant results ($p < 0.05$) are highlighted in bold.

T_2*	t-test acute vs chronic RNC	0.16023074
	t-test acute vs chronic RNM	0.12994041
	t-test acute vs chronic LNC	0.91589031
	t-test acute vs chronic LNM	0.26696199
	t-test acute vs control RNC	0.4356154
	t-test acute vs control RNM	**0.07961873**
	t-test acute vs control LNC	0.34891853
	t-test acute vs control LNM	0.29096364
	t-test chronic vs control RNC	0.22630449
	t-test chronic vs control RNM	0.55934004

	t-test chronic vs control LNC	0.45380286
	t-test chronic vs control LNM	0.69058653
	t-test acute vs healthy RNC	1.61287E-09
	t-test acute vs healthy RNM	4.8858E-10
	t-test acute vs healthy LNC	1.12598E-11
	t-test acute vs healthy LNM	2.68558E-11
	t-test chronic vs healthy RNC	1.87166E-07
	t-test chronic vs healthy RNM	7.22329E-08
	t-test chronic vs healthy LNC	1.12598E-11
	t-test chronic vs healthy LNM	1.52097E-08

*Significant results ($p < 0.05$) in bold

Table LI: t-tests for parameter T_2 Map between the four groups: acute, chronic, healthy and control. *p*-values can be found in the third column. Significant results ($p < 0.05$) are highlighted in bold.

T_2 Map	t-test acute vs chronic RNC	0.957644654
	t-test acute vs chronic RNM	0.380786849
	t-test acute vs chronic LNC	0.332659752
	t-test acute vs chronic LNM	0.605466716
	t-test acute vs control RNC	0.490233244
	t-test acute vs control RNM	0.242726796
	t-test acute vs control LNC	0.359789917
	t-test acute vs control LNM	0.64007278
	t-test chronic vs control RNC	0.437383485
	t-test chronic vs control RNM	0.949822493
	t-test chronic vs control LNC	0.335294715
	t-test chronic vs control LNM	0.974812455
	t-test acute vs healthy RNC	0.257279456
	t-test acute vs healthy RNM	0.084771757
	t-test acute vs healthy LNC	0.436341766
	t-test acute vs healthy LNM	0.599702552
	t-test chronic vs healthy RNC	0.266440551
	t-test chronic vs healthy RNM	0.517208971
	t-test chronic vs healthy LNC	0.188186436
	t-test chronic vs healthy LNM	0.84314897

*Significant results ($p < 0.05$) in bold

10.5 Patient Information and Consent

UKD Universitätsklinikum Düsseldorf

HEINRICH HEINE UNIVERSITÄT DÜSSELDORF

Institut für Diagnostische und Interventionelle Radiologie

Direktor
Univ.-Prof. Dr. G. Antoch

Sekretariat
Tel.: (0211) 81-17752
Fax: (0211) 81-16145
radiologie@med.uni-duesseldorf.de

Moorenstrasse 5
D-40225 Düsseldorf

Stellv. Direktor
Univ.-Prof. Dr. G. Fürst
Tel. (0211) 81-08555
Fax. (0211) 81-08558
fuerst@med.uni-duesseldorf.de

Leitender Oberarzt
Priv.-Doz. Dr. L. Schimmöller
Tel. (0211) 81-17295
Fax: (0211) 81-16145
Lars.Schimmoeller@med.uni-duesseldorf.de

Geschäftsführender Oberarzt
Dr. L. Sawicki
Tel. (0211) 81-18518
Fax: (0211) 81-16145
LinoMorris.Sawicki@med.uni-duesseldorf.de

Bereich Neuroradiologie
Prof. Dr. B. Turowski
Tel. (0211) 81-17968
Fax. (0211) 81-08876
bernd.turowski@med.uni-duesseldorf.de

Bereich Kinderradiologie
Dr. J. Schaper
Tel. (0211) 81-17665
Fax. (0211) 81-19293
schaper@med.uni-duesseldorf.de

Bereich Gynäkologische Radiologie
Dr. F. Dietzel
Tel. (0211) 81-17528
Fax. (0211) 81-17522
Frederic.Dietzel@med.uni-duesseldorf.de

Bereich Medizinische Physik
Prof. Dr. H.- J. Wittsack
Tel. (0211) 81-17356
Fax. (0211) 81-16299
hans-joerg.wittsack@med.uni-duesseldorf.de

Probanden-/Patienteninformation

Funktionelle, kontrastmittelfreie MRT-Untersuchungen

Sehr geehrte/r Studienteilnehmer/in,

Mit der Studie prüfen wir am Universitätsklinikum Düsseldorf die Möglichkeit der funktionellen, nicht-invasiven und kontrastmittelfreien MRT-Untersuchung.
Die geplante MRT-Untersuchung kann neben der Anatomie des untersuchten Organs auch Aussagen über die organspezifische Funktion und Feinstruktur des Organgewebes treffen. Auch die Möglichkeit der Unterscheidung vom gesundem und krankem Gewebe mittels der geplanten MRT-Untersuchung soll im Rahmen dieser Studie überprüft werden.

Das bei Ihnen geplante Untersuchungsprotokoll umfasst eine Übersichtsmessung zur anatomischen Darstellung und eine bis zwei funktionelle Messungen. Die Untersuchung findet in Rückenlage statt und die Untersuchungsdauer beträgt ca. 30 Minuten.

Zur Durchführung der MRT-Untersuchung ist kein Kontrastmittel und auch kein anderes Medikament erforderlich. Nach gegenwärtigem Kenntnisstand ist eine MRT-Untersuchung für den Menschen nicht schädlich.

Durch die Teilnahme an der Studie erwächst kein für Sie relevanter Nutzen. Auch haben die im Rahmen der geplanten Untersuchung erhobenen Daten keinen Einfluss auf die bei Ihnen womöglich geplante Therapie durch den behandelnden Arzt. Allerdings könnten die Ergebnisse möglicherweise in Zukunft einen medizinischen

Fortschritt darstellen.

Nicht teilnehmen können Probanden/Patienten mit

- Klaustrophobie
- Künstliche Herzklappe
- Herzschrittmacher
- Cochlea-Implantat
- Alle anderen metallischen Implantate (Feste Zahnspange, Retainer, Dauerakkupunkturnadel, abgebrochene Biopsienadel etc.)
- Metall im Körper (Granatsplitter etc.)
- Großflächige Tätowierungen, metallische Schminke
- Alter unter 18. Lebensjahr
- Implantierte Medikamentenpumpe
- Schwere Kreislauferkrankungen, Lungen- oder Herzerkrankungen, Diabetes
- Neurologische Erkrankungen, Epilepsie, Schlaganfall etc.
- Gehörerkrankungen, Tinnitus, erhöhte Empfindlichkeit gegenüber lauten Geräuschen
- Fehlendes schriftliches Einverständnis
- Schwangerschaft (Probandinnen, welche die Frage nach einer Schwangerschaft nicht eindeutig verneinen können, werden von der Studie ausgeschlossen)
- Weitere MRT-Ausschlusskriterien (werden vom Studienarzt geprüft)

Alle im Rahmen der Untersuchung erhobenen personenbezogenen Daten werden entsprechend der ärztlichen Schweigepflicht und den gesetzlichen Bestimmungen des Datenschutzes vertraulich behandelt und nicht an Dritte weitergegeben. Die Studienleitung wird alle angemessenen Schritte unternehmen, um den Schutz Ihrer Daten gemäß den Datenschutzstandards der Europäischen Union zu gewährleisten. Die Daten sind gegen unbefugten Zugriff gesichert.

Die erhobenen Bilddaten werden zunächst vom Studienarzt auf mögliche, noch unbekannte Pathologien überprüft (der Verlauf der bereits bekannten

Pathologien wird hierbei nicht beurteilt). Sollte hierbei ein pathologischer, noch nicht bekannter Zufallsbefund festgestellt werden, werden Sie umgehend vom Studienarzt kontaktiert und über diesen aufgeklärt.

Bei der wissenschaftlichen Auswertung wird ihr Name durch eine fortlaufende Nummer ausgetauscht. Diese Pseudonymisierung erfolgt dabei bereits zum Zeitpunkt der Speicherung von Bilddaten einer Untersuchung im elektronischen Bildarchiv des Instituts (= Datenbank 2). Eine Refernzliste mit personenbezogenen Daten der Probanden/Patienten wird auf einem separaten Rechner, der die Bestimmungen des Datenschutzgesetzes erfüllt, aufbewahrt (= Datenbank 1). Eine Zuordnung der personenbezogenen Daten zu den Studiendaten dürfen nur die Prüfärzte vornehmen. Nach Abschluss oder Abbruch der Studie werden die Prüfungsunterlagen gemäß den Bestimmungen des Datenschutzes verwaltet und für mindestens weitere zehn Jahre im Institut aufbewahrt. Anschließend erfolgt eine unwiederrufliche Löschung der Referenzliste durch den Studienarzt. Ab diesem Zeitpunkt liegen sämtliche Studiendaten in anonymisierter Form vor.

Sie können die Untersuchung jederzeit abbrechen. Ebenso können Sie die Einwilligung zur Teilnahme an der Studie jederzeit widerrufen. Beim Widerruf Ihrer Einwilligung werden alle personenbezogenen Daten unverzüglich gelöscht. Bitte beachten Sie, dass ab dem Zeitpunkt der vollständigen Anonymisierung der Studiendaten zwar der Widerruf der Einwilligung möglich ist, eine Löschung Ihrer anonymisierten Daten jedoch nicht mehr erfolgen kann, da nach erfolgter, vollständiger Anonymisierung der Studiendaten eine Zuordnung der Studiendaten zu den persönlichen Daten nicht mehr möglich ist.
Ein Widerruf ist in schriftlicher Form an die Studienleitung, Frau Dr. med. Alexandra Ljimani, Institut für Diagnostische und Interventionelle Radiologie UKD, Moorenstr. 5, 40225 Düsseldorf, Tel.: 0211-81-17752, zu richten.

Der Verantwortliche für die studienbedingte Erhebung personenbezogener Daten ist die Studienleiterin, Frau Dr. med. Alexandra Ljimani, Institut für Diagnostische und Interventionelle Radiologie UKD, Moorenstr. 5, 40225 Düsseldorf, Tel.: 0211-81-17752. Sie haben das Recht, vom Verantwortlichen Auskunft über die von Ihnen gespeicherten personenbezogenen Daten zu

verlangen. Ebenfalls können Sie die Berichtigung unzutreffender Daten sowie die Löschung der Daten oder Einschränkung deren Verarbeitung verlangen.

Bei Anliegen, Fragen oder Beschwerden zur Datenverarbeitung und zur Einhaltung der datenschutzrechtlichen Anforderungen wenden Sie sich bitte zunächst an die Studienleitung (Kontaktdaten siehe oben).

Für weiterführende Fragen oder bei Problemen bzgl. des Datenschutzes können Sie sich an folgende Stellen wenden:

Datenschutzbeauftragte/r des Universitätsklinikums Düsseldorf *(zuständig für Patienten und Mitarbeiter als Studienteilnehmer für Studien am UKD)*
Moorenstr. 5, 40225 Düsseldorf
datenschutz@med.uni-duesseldorf.de

Datenschutzbeauftragte/r der Heinrich-Heine-Universität Düsseldorf *(zuständig für gesunde Probanden und Studierende als Studienteilnehmer für Studien am UKD)*
Universitätsstr. 1, 40225 Düsseldorf
datenschutzbeauftragter@hhu.de

Im Falle einer rechtswidrigen Datenverarbeitung haben Sie das Recht, sich bei folgender Aufsichtsbehörde zu beschweren:

Landesbeauftragte für Datenschutz und Informationsfreiheit Nordrhein-Westfalen
Postfach 20 04 44, 40102 Düsseldorf
E-Mail: poststelle@ldi.nrw.de

Der direkte Weg zum und vom Studienort sowie der Aufenthalt am Studienort sind durch eine Wegeunfallversicherung versichert. Die Schadensanzeige ist in schriftlicher Form an die Studienleiterin, Frau Dr. med. Alexandra Ljimani, Institut für Diagnostische und Interventionelle Radiologie UKD, zu richten.
Für unverschuldete Gesundheitsschäden, die während der Studie entstehen, wird keine Haftung übernommen.

Universitätsklinikum Düsseldorf

HEINRICH HEINE
UNIVERSITÄT DÜSSELDORF

Institut für Diagnostische und Interventionelle Radiologie

Direktor
Univ.-Prof. Dr. G. Antoch

Sekretariat
Tel.: (0211) 81-17752
Fax: (0211) 81-16145
radiologie@med.uni-duesseldorf.de

Moorenstrasse 5
D-40225 Düsseldorf

Stellv. Direktor
Univ.-Prof. Dr. G. Fürst
Tel. (0211) 81-08555
Fax. (0211) 81-08558
fuerst@med.uni-duesseldorf.de

Leitender Oberarzt
Priv.-Doz. Dr. L. Schimmöller
Tel. (0211) 81-17295
Fax: (0211) 81-16145
Lars.Schimmoeller@med.uni-duesseldorf.de

Geschäftsführender Oberarzt
Dr. L. Sawicki
Tel. (0211) 81-18518
Fax: (0211) 81-16145
LinoMorris.Sawicki@med.uni-duesseldorf.de

Bereich Neuroradiologie
Prof. Dr. B. Turowski
Tel. (0211) 81-17968
Fax. (0211) 81-08876
bernd.turowski@med.uni-duesseldorf.de

Bereich Kinderradiologie
Dr. J. Schaper
Tel. (0211) 81-17665
Fax. (0211) 81-19293
schaper@med.uni-duesseldorf.de

Bereich Gynäkologische Radiologie
Dr. F. Dietzel
Tel. (0211) 81-17528
Fax. (0211) 81-17522
Frederic.Dietzel@med.uni-duesseldorf.de

Bereich Medizinische Physik
Prof. Dr. H.- J. Wittsack
Tel. (0211) 81-17356
Fax. (0211) 81-16299
hans-joerg.wittsack@med.uni-duesseldorf.de

Probanden-/Patienteneinwilligungserklärung zur Teilnahme an der Studie:

Funktionelle, kontrastmittelfreie MRT-Untersuchungen

Hiermit bestätige ich, dass ich die Probanden-/Patienteninformation gelesen und in einer Aufklärung durch einen Arzt ausführlich und verständlich über die Bedeutung, Risiken und Tragweite der Untersuchung aufgeklärt worden bin. Ich habe darüber hinaus den Text der Probanden-/Patienteninformation sowie die hier nachfolgend abgedruckten Erklärungen gelesen und verstanden. Ich hatte die Gelegenheit, mit dem Prüfarzt über die Durchführung der Untersuchung zu sprechen. Alle meine Fragen wurden zufriedenstellend beantwortet.

Mir ist bekannt, dass bei dieser Studie personenbezogene Daten, insbesondere medizinische Befunde über mich erhoben, gespeichert und ausgewertet werden sollen. Die Verwendung der Angaben über meine Gesundheit erfolgt nach gesetzlichen Bestimmungen und setzt vor der Teilnahme an der klinischen Untersuchung folgende freiwillig abgegebene Einwilligungserklärung voraus, das heißt ohne die nachfolgende Einwilligung kann ich nicht an der klinischen Untersuchung teilnehmen.

Mir ist bekannt, dass bei dieser Studie erhobenen Bilddaten vom Studienarzt unter medizinischen Gesichtspunkten ausgewertet werden. Beim Vorliegen eines möglichen, noch unbekannten, pathologischen Befundes bin ich damit einverstanden, dass der Studienarzt Kontakt mit mir aufnimmt und mir diesen Befund mitteilt. Mir ist bewusst, dass ein solcher Zufallsbefund eine lebensverändernde Diagnose nach sich ziehen kann.

Der direkte Weg zum und vom Studienort sowie der Aufenthalt am Studienort sind durch eine Wegeunfallversicherung versichert. Die Schadensanzeige ist in schriftlicher Form an die Studienleiterin, Frau Dr. med. Alexandra Ljimani, Institut für Diagnostische und Interventionelle Radiologie UKD, zu richten.
Mir ist bekannt, dass für unverschuldete Gesundheitsschäden, die während der Studie entstehen, keine Haftung übernommen wird.

Ich willige ein, dass im Rahmen dieser klinischen Untersuchung personenbezogene Daten, insbesondere Angaben über meine Gesundheit, über mich erhoben und in Papierform sowie auf elektronischen Datenträgern im Institut für Diagnostische und Interventionelle Radiologie aufgezeichnet werden.

Während der laufenden Studie erfolgt die Speicherung der Daten in pseudonymisierter Form, d.h. der Patientenname wird bereits zum Zeitpunkt der Speicherung der Bilddaten einer Untersuchung durch eine fortlaufende Nummer ausgetauscht. Eine Referenzliste mit personenbezogenen Daten aller Probanden/Patienten wird auf einem separaten Institutscomputer, der die Bestimmungen des Datenschutzgesetzes erfüllt, aufbewahrt.

Ich willige ein, dass meine Daten nach Beendigung oder Abbruch der Untersuchung mindestens zehn Jahre aufbewahrt werden. Danach werden meine personenbezogenen Daten gelöscht, soweit nicht gesetzliche, satzungsmäßige oder vertragliche Aufbewahrungsfristen entgegenstehen.
Ab diesem Zeitpunkt liegen sämtliche Studiendaten in anonymisierter Form vor. Eine Zuordnung zu den persönlichen Daten ist ab diesem Zeitpunkt nicht mehr möglich.

Ich bin darüber aufgeklärt worden, dass ich jederzeit die Teilnahme an der klinischen Untersuchung beenden kann. Beim Widerruf meiner Einwilligung an der Studie teilzunehmen werden alle personenbezogenen Daten unverzüglich gelöscht.
Des weiteren bin ich darüber aufgeklärt worden, dass ab dem Zeitpunkt der unwiderruflichen Anonymisierung der Studiendaten zwar ein Widerruf der Einwilligungserklärung möglich ist, die Löschung der anonymisierten Studiendaten jedoch aufgrund des fehlenden Personenbezuges nicht mehr erfolgen kann.
Ein Widerruf ist in schriftlicher Form an die Studienleitung, Frau Dr. med. Alexandra Ljimani, Institut für Diagnostische und Interventionelle Radiologie UKD, Moorenstr. 5, 40225 Düsseldorf, Tel.: 0211-81-17752, zu richten.

Ich willige ein, an der o.g. Studie als Proband/Patient freiwillig teilzunehmen und bin darüber informiert worden, dass meine Daten im Rahmen der Studie sowie in wissenschaftlichen Publikationen anonymisiert verwendet werden.

Name des Teilnehmers: _____, geb. _____

Teilnehmer-Nr.: _____

Düsseldorf, Unterschrift Proband/Patient Unterschrift Arzt

Acknowledgments

I would like to thank Dr. Dragan Spaic for invaluable support with the statistical analyses, and PD Dr. Alexandra Ljimani for guidance not only as my supervisor but also as a true mentor and life coach.

I also wish to thank my boyfriend, Johannes Krautstrunk, for his unconditional support, for proofreading my work, and for being both my biggest critic and my greatest supporter.

Another heartfelt thanks goes to my best friend, Anne Riter, for carefully editing the language and grammar of my thesis and for always supporting me, despite the ocean that separates us.